Dissertation zur Erlangung des Doktorgrades

der Fakultät für Chemie und Pharmazie

der Ludwig-Maximilians-Universität München

Tumor-targeted Delivery of Cas9 mRNA and sgRNA against KRAS-Mutated Lung Cancer

Siyu Chen

Aus

Siping, Jilin, China

2024

Erklärung

Diese Dissertation wurde im Sinne von § 7 der Promotionsordnung vom 28. November 2011 von Frau Prof. Dr. Olivia M. Merkel betreut.

Eidesstattliche Versicherung

Diese Dissertation wurde eigenständig und ohne unerlaubte Hilfe erarbeitet.

München, 15.10.2024

.....

Siyu Chen

Dissertation eingereicht am: 17.10.2024

1. Gutachterin: Prof. Dr. Olivia. M. Merkel
2. Gutachter: Prof. Dr. Wolfgang Frieß

Mündliche Prüfung am: 22.11.2024

To my family

“唯爱永存”

Table of Contents

1. Abstract

According to the Global Cancer Statistics 2022, lung cancer is the most commonly diagnosed cancer and the leading cause of cancer-related deaths worldwide.[1] Among various genetic mutations linked to lung cancer, KRAS mutations are observed in 25% of cases, making it the most frequently mutated gene.[2] Designing inhibitors for KRAS has been challenging due to its relatively smooth protein structure, which lacks obvious binding sites, stalling drug development for years. However, the advent of CRISPR-Cas9 has revolutionized gene therapy, offering a powerful and customizable tool for genome editing. CRISPR-Cas9, an adaptive immune system found in most bacteria and archaea, holds great promise for correcting pathogenic mutations, including KRAS mutations, due to its fast onset, transient expression, low off-target effects, and cost-effectiveness.[3]

CRISPR-Cas9 can be delivered through various methods, including plasmid DNA,[4] mRNA/sgRNA,[5] and protein/sgRNA ribonucleoprotein complexes (RNPs).[6] In recent years, mRNA delivery technology has advanced significantly, with the development of mRNA vaccines against COVID-19 being a landmark success. The nucleoside-modified mRNA-LNP vaccines from Moderna and Pfizer/BioNTech have established mRNA as a viable therapeutic platform. Beyond vaccines, mRNA-based CRISPR-Cas9 therapeutics offer several advantages,[7,8] including transient expression, which allows for controlled therapeutic effects, minimizing off-target risks and avoiding the possibility of genomic integration. This makes mRNA delivery systems safer and more precise compared to viral vectors, sparking growing interest in their use for gene editing.

Despite these benefits, efficient delivery of mRNA for CRISPR-Cas9 remains a significant challenge, especially for the co-delivery of Cas9 mRNA and sgRNA. In this study, we screened various polymers and developed a lipid-modified polymer, C14-PEI for co-delivery of Cas9 mRNA and sgRNA for *KRAS* mutant lung cancer therapy. After extensive characterization, a novel micelleplex with

C14-PEI was designed to target *KRAS* mutations in lung cancer. The C14-PEI nanoparticles demonstrated favorable properties, mediating high eGFP mRNA expression and effective *KRAS* mutation knockout. By incorporating PEG-PLE to shield the positive surface charges, we optimized the nanoparticle characteristics and significantly enhanced gene editing efficiency. Furthermore, we employed an engineered affibody targeting the Erbb3 receptor, which is overexpressed in *KRAS*-mutant lung cancer cells, to conjugate the polyplexes for specific targeting. This conjugation strategy allowed us to demonstrate that affibody-conjugated polyplexes can specifically target Erbb3 and enhance polyplex retention within cells. Adjusting the formulation and affibody density further modified the polyplex behavior, showing the potential of this approach for targeted mRNA delivery in gene therapy.

2. Introduction

2.1 CRISPR Gene Editing

Clustered Regularly Interspaced Short Palindromic Repeats (CRISPR) are sequences found in prokaryotic bacteria and archaea that play a role in their adaptive immune systems. First identified by Ishino et al. in 1987,[9] CRISPR was further defined by Mojica in 1993[10], but it remained relatively underexplored until 2012. That year, Jennifer A. Doudna and Emmanuelle Charpentier introduced a groundbreaking genome editing tool based on the CRISPR-Cas9 system, earning them the 2020 Nobel Prize in Chemistry.[11] The development of the CRISPR-Cas9 system in 2012 revolutionized molecular biology, ushering in an era of rapid advancements. In 2013, Feng Zhang and colleagues successfully applied CRISPR-Cas9 to edit mammalian genomes.[4] Soon after, researchers extended its application to genome editing in various organisms, including mice[12], drosophila[13], zebrafish[14], crop[15], and others[16,17]. This widespread success marked the beginning of CRISPR's transformative impact across multiple fields of biology.

2.1.1 Classification of CRISPR-Cas System

Makarov classified CRISPR-Cas systems into two classes, comprising six types and several subtypes,[18,19] based on the number and function of Cas genes (Figure 1). Class 1, which includes types I, III, and IV, requires multiple Cas proteins to form a complex that collaboratively interferes with target genes. In contrast, Class 2 systems, such as types II, V, and VI rely on a single Cas protein to carry out gene interference.[20] Class 2 CRISPR-Cas systems are particularly appealing for gene-editing applications due to their simpler structure and clearer mechanisms.[21] This class includes the well-known Cas9 from type II, as well as Cas12a (formerly Cpf1) and Cas12b (C2c1) from type V, and Cas13a (C2c2) and Cas13b (C2c3) from type VI.[22] Among these, the Cas9 protein has been the most extensively studied and applied. Cas9 is a 160 kilo

Dalton (kDa) endonuclease with a bi-lobed architecture, consisting of REC and NUC lobes, that forms a ribonucleoprotein complex by binding to CRISPR RNA (crRNA) and trans-activating crRNA (tracrRNA), which together recognize target double-stranded DNA (dsDNA). In practice, the crRNA-tracrRNA complex is often replaced by a single-guide RNA (sgRNA), which serves the same function.[3,14] The Cas9 protein contains three key domains within its NUC lobe: HNH, RuvC, and the PAM-interacting (PI) domain. The HNH and RuvC domains are responsible for cleaving the DNA strands, while the PI domain recognizes the protospacer adjacent motif (PAM), a required three-nucleotide sequence (-NGG-) on the target DNA.[11,23,24]

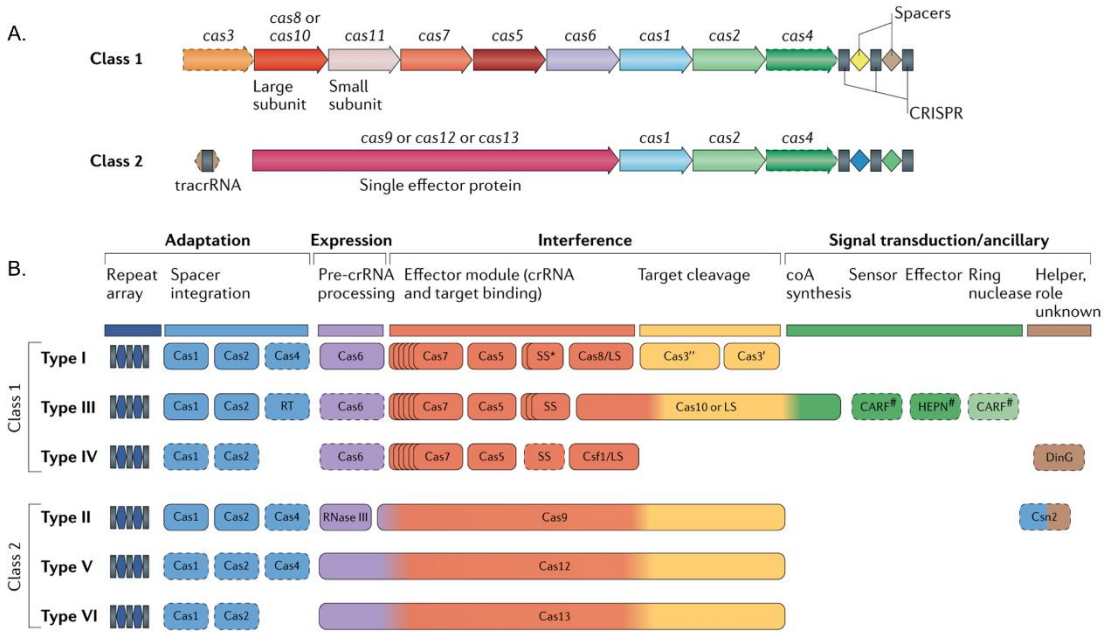

Figure 1. Classification of the CRISPR system. A. Structures of Class 1 and Class 2. **B.** Different types and their respective regions. Reproduced from Ref.19 Copyright ©2019, with permission from Springer Nature.

Cpf1, also known as Cas12a, is a single RNA-guided endonuclease found in various bacterial and archaeal genomes.[21] As part of the class 2, type V CRISPR system, Cpf1 is structurally distinct from Cas9. It contains two RuvC-like nuclease domains but lacks the HNH domain present in Cas9.[25] Unlike Cas9, Cpf1 does not require tracrRNA, and its essential crRNA is smaller. Another key difference is that Cpf1 recognizes a T-rich PAM sequence (-TTTN-), compared to Cas9's preference for a G-rich PAM. Cpf1 also creates sticky ends

during DNA cleavage, whereas Cas9 produces blunt ends. Sticky ends are generally more efficient for DNA repair processes like homologous recombination, which is critical for precise gene insertion or correction. In contrast, Cas9's blunt ends are less effective for such repair mechanisms, limiting its use in applications requiring precision. Additionally, Cas9's dependence on a G-rich PAM restricts its targetable genomic regions, posing a limitation in editing locations that lack a compatible PAM. Moreover, the need for both crRNA and tracrRNA in Cas9 complicates the delivery process, as these two components must either be co-delivered or processed from a sgRNA *in vivo*. These characteristics make Cpf1 a smaller, simpler endonuclease, addressing several limitations of the CRISPR-Cas9 system. As a result, Cpf1 offers a viable alternative for gene editing, especially in cases where Cas9's target range and repair efficiency are restrictive.

Beyond Cas9 and Cpf1, other unique effectors have been discovered in recent years. In 2015, Shmakov and colleagues identified three distinct class 2 CRISPR-Cas systems, Cas12b (C2c1), Cas13a (C2c2), and Cas13b (C2c3), using a computational pipeline designed to explore microbial genome sequence diversity.[20] Both Cas12b and Cas13b possess RuvC-like endonuclease domains, while Cas13a contains higher eukaryote and prokaryote nucleotide-binding (HEPN) RNase domains, which mediate RNA interference.[26] Additionally, several engineered Cas9 variants and homologs have been developed to overcome Cas9's limitations, particularly its strict requirement for an NGG PAM sequence, which restricts sgRNA design.[27,28] These advances are likely to open new possibilities for applying CRISPR systems in genome engineering technology (Table 1).

Table 1. Summary of Cas and other typical nuclease variants used in CRISPR experiments and their PAM sequences.

CRISPR Nucleases	Organism Isolated From	PAM Sequence (5' to 3')	Reference

SpCas9	*Streptococcus pyogenes*	NGG-	11
SaCas9	*Staphylococcus aureus*	NNGRRT-	29
NmeCas9	*Neisseria meningitidis*	NNNNGATT-	30
CjCas9	*Campylobacter jejuni*	NNNNRYAC or NNNNACAC	31
StCas9	*Streptococcus thermophilus*	NNAGAAW	32
LbCpf1	*Lachnospiraceae bacterium*	TTTN	33
AsCpf1	*Acidaminococcus sp.*	TTTN	33
FnCpf1	*Francisella novicida*	TTN	34

2.1.2 Mechanism of CRISPR-Cas System

In nature, CRISPR functions as an adaptive immune system in bacteria and archaea, defending against viral invasion. When a virus attacks, the surviving bacteria store fragments of the viral DNA in their genome between CRISPR sequence repeats. If the same virus invades again, the bacteria produce a complementary RNA sequence that recruits the Cas nuclease to cut the viral DNA, halting the infection.[35] The mechanism by which CRISPR targets and cleaves DNA can be explained through its structure. The CRISPR-Cas9 system, particularly the commonly used type II system, requires only a single DNA

endonuclease, Cas9.[24] Cas9 has two distinct nuclease domains, HNH and RuvC, which recognize and cleave dsDNA (Figure 2). The HNH domain cleaves the strand complementary to the crRNA, while the RuvC domain cleaves the opposite strand.[23] In type II systems, tracrRNA, located upstream of the CRISPR array, is essential for forming a dual-RNA hybrid structure with crRNA in the presence of RNase III, guiding Cas9 to cleave DNA at a complementary 20-nucleotide target sequence adjacent to a PAM.[36] Studies have shown that using a sgRNA instead of the crRNA-tracrRNA complex enhances the efficiency of DNA targeting.[37] In this system, the Cas9 protein and sgRNA form a ribonucleoprotein complex, facilitated by interactions between the sgRNA scaffold and positively charged grooves on the Cas9 surface. Upon binding to sgRNA, Cas9 undergoes a conformational change from an inactive state to an active, DNA-binding conformation. The sgRNA's spacer region remains free to interact with the target DNA, allowing the two-component CRISPR-Cas9 system to be programmed to target virtually any DNA sequence. Once Cas9 creates a site-specific blunt-ended double-strand break (DSB), the DSB can be repaired either through error-prone non-homologous end joining (NHEJ), which introduces small insertions or deletions (indels), or through homology-directed repair (HDR), enabling precise genome modification using a homologous repair template.[38]

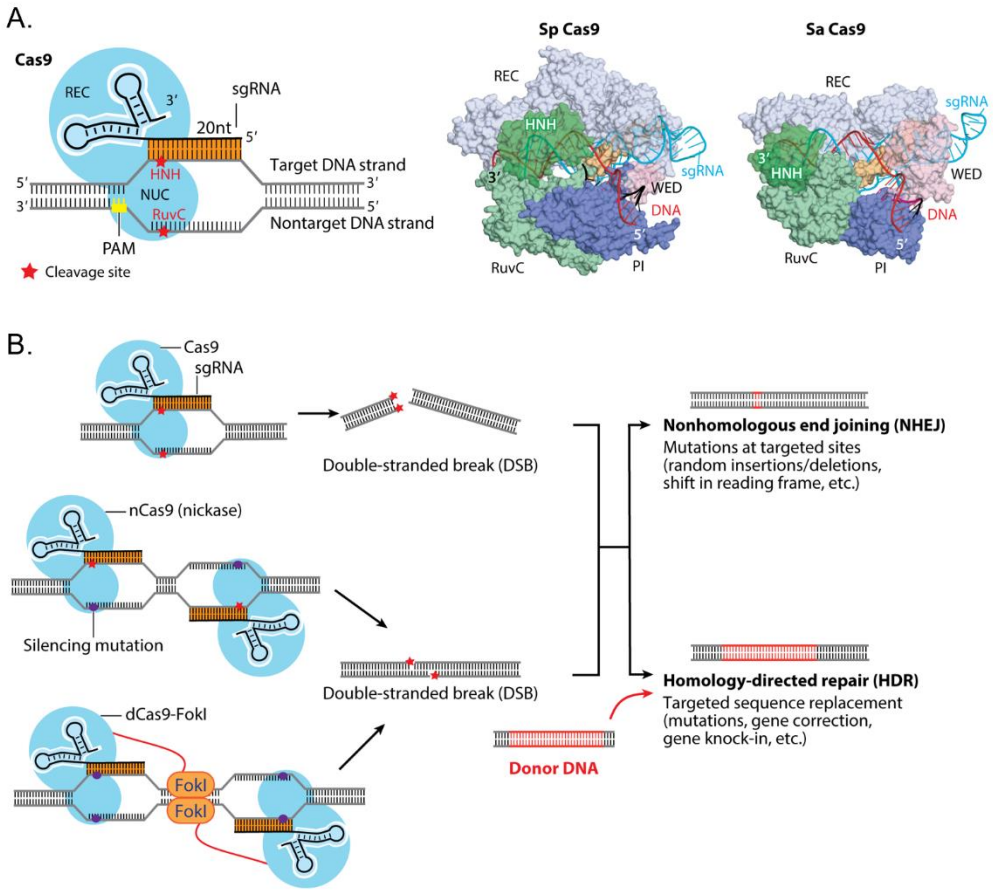

Figure 2. The structure (A.) and mechanism (B.) of CRISPR-Cas9. Reproduced from Ref.25 Copyright ©2016, with permission from Annual Reviews.

2.1.3 Forms of CRISPR Delivery

With the advancement of the CRISPR-Cas genome editing system, improving the efficiency and safety of both *in vivo* and *in vitro* delivery systems has become a critical challenge. Cas9 can be delivered in three primary forms: plasmid DNA[4], mRNA/sgRNA[5], and protein/sgRNA ribonucleoprotein complexes (RNPs).[6,7] Depending on the specific form of CRISPR-Cas, experimental models, and sample types, a range of delivery strategies can be employed. For animal models, Cas9 DNA or RNA, along with sgRNA or CRISPR RNPs, are typically introduced into zygotes through microinjection or electroporation to generate modified organisms in a single step.[39] In contrast, delivery to cells is more complex due to concerns about off-target effects (OTEs) and immunogenicity.

Plasmids

The plasmid-encoded Cas9 protein and sgRNA format is the most classical and widely used approach for CRISPR delivery. Its successful application across various organisms,[40] including mice,[41] humans,[4] and plants,[15] demonstrates that plasmid-based CRISPR-Cas9 is a straightforward and convenient strategy, as it circumvents the need to transfect multiple components into the same cells.[7] Since plasmid systems enable both transient and stable expression of Cas9 and sgRNA in mammalian cell lines with high efficiency, many have been designed to include necessary elements such as enhancers and reporters. For instance, the pX260 vector expresses Cas9 protein and sgRNA from the same plasmid, housing cassettes for crRNA, tracrRNA, and SpCas9 sequences.[7] The plasmid is digested with a restriction enzyme and ligated with an annealed oligonucleotide designed for a specific target site.

Despite its advantages, the plasmid-based CRISPR system presents several challenges. One issue is cytotoxicity—research has shown that transfecting certain cell lines with plasmids can lead to cell death.[42] More critically, plasmid-based systems require time for intracellular processing before genome editing can occur.[7] After transfection, the plasmid must be transported into the nucleus for the transcription of sgRNA and Cas9-encoding mRNA. The resulting mRNA must then exit the nucleus for Cas9 protein translation. Once produced, the Cas9 protein binds sgRNA, and this complex reenters the nucleus to locate and edit the target genome. Additionally, plasmid-based CRISPR-Cas9 systems tend to produce more OTEs. Since Cas9 and sgRNA remain active in the cell for extended periods, the risk of cutting non-targeted genomic sites increases.[43] Prolonged expression of the Cas9 enzyme and sgRNA from plasmids has been shown to elevate the likelihood of off-target insertions, further complicating precise gene editing.[44]

RNPs

Direct delivery of the Cas9 protein complexed with sgRNA has emerged as the most extensively studied strategy in recent years. The purified Cas9 protein,

being positively charged, efficiently forms RNPs.[45] This RNP approach offers several advantages for CRISPR experiments, including rapid action and high gene editing efficiency. RNPs can be effectively used in cells that are typically resistant to transfection, such as primary cells. Additionally, using RNPs mitigates challenges related to protein expression in cells where common eukaryotic promoters, like CMV or EF1A, found in many CRISPR plasmids, are not expressed. Furthermore, RNP delivery limits potential off-target effects, toxicity, and immune responses because it does not involve the introduction of foreign DNA, and the Cas9-gRNA complex is naturally degraded over time.[7] In 2014, Kim and colleagues demonstrated the advantages of delivering Cas9/sgRNA RNPs directly into cells via electroporation, bypassing the limitations of plasmid-based delivery.[46] Their findings showed that RNPs enable efficient genome editing in human primary and embryonic stem (ES) cells that are typically resistant to DNA transfection, while also reducing off-target effects and preventing unwanted plasmid DNA integration into the host genome. Similarly, Ramakrishna and colleagues illustrated that treatment with cell-penetrating peptide (CPP)-conjugated recombinant Cas9 protein, alongside CPP-complexed guide RNAs, resulted in endogenous gene disruptions in human cell lines, further confirming that RNP delivery can reduce OTEs compared to plasmid transfections.[47] Despite these advantages, the use of Cas9-RNPs does present challenges, including the manufacturing and preservation of Cas9 protein activity, as well as difficulties in *in vivo* protein delivery.[48] Endosomal entrapment poses a significant barrier, as therapeutic proteins must localize to the cytosol or, in the case of Cas9, the nucleus. Additionally, the expression of Cas9 protein can be laborious, and once isolated, its nuclease activity diminishes within days.[8,40] To enhance the efficiency of Cas9-RNP delivery, researchers have conducted extensive investigations. For example, Chen and colleagues developed CRISPR-EZ (CRISPR RNP Electroporation of Zygotes), an electroporation-based method that delivers Cas9/sgRNA RNPs into mouse zygotes. This innovative approach enables high-efficiency, high-throughput *in vivo* genome editing while ensuring high viability, significantly simplifying RNP delivery in mouse zygotes.[39]

mRNA and sgRNA

Delivery of a Cas9 mRNA formulation combined with sgRNA enables transient expression of the Cas9 protein, which limits the duration of gene editing and consequently reduces the risk of OTEs and side effects. Within target cells, Cas9 mRNA is translated into the Cas9 protein, which then forms a complex with sgRNA. This delivery strategy offers several notable advantages.[49] First, the combination of Cas9 mRNA and sgRNA demonstrates low cytotoxicity in both primary and immortalized cell lines. Second, compared to plasmid-based CRISPR-Cas systems, mRNA delivery typically results in fewer OTEs. Since mRNAs only need to enter the cytoplasm to exert their effects, this method can minimize off-target activity.[7] Furthermore, compared with more established mRNA-based approaches, systemic RNP delivery requires further evaluation and optimization to address challenges related to duration of action time and immune response.[8] On the one hand, mRNA can continuously translate into the encoded protein, facilitating longer-lasting expression compared to the transient delivery of Cas9 RNPs. On the other hand, RNPs consist of a protein component, like Cas9, that can potentially be immunogenic, and more research is needed to understand and mitigate these immune responses when delivered systemically. Whereas mRNA-based systems have been more extensively studied in immune response, with strategies developed to minimize innate immune activation, such as the use of chemically modified nucleotides in the mRNA. The ability to modify mRNA sequences to encode regulatory elements also allows for controlled expression of gene-editing tools in a cell-specific manner. In 2013, Shen and colleagues first demonstrated the use of the CRISPR-Cas system to cut DNA in zebrafish and mouse embryos using Cas9 mRNA and sgRNA, paving the way for generating gene-disrupted animals.[50] They later showed that employing Cas9 nickase and paired sgRNAs significantly increased the fidelity of the system for *in vivo* genome editing without compromising efficiency.[51] Similarly, Auer and colleagues successfully converted eGFP into Gal4 transgenic lines by co-injecting a donor plasmid with short sgRNA and Cas9 mRNA into zebrafish.[52]

However, the effectiveness of this gene-editing approach is limited by the

delivery of both components — mRNA and sgRNA.[40] Yin and colleagues highlighted the reliance on viral co-delivery to supplement mRNA delivery.[53] They utilized nanoparticle-mediated delivery of Cas9 mRNA alongside adeno-associated viruses (AAVs) encoding sgRNA and a repair template to achieve significant correction (over 6%) in the fumarylacetoacetate hydrolase *(Fah)* gene. While some studies have succeeded in co-delivery, mRNA-based approaches often face challenges due to the necessity of delivering multiple components. Thus far, mRNA-based gene editing has primarily been accomplished *in vivo* and *in vitro* through co-delivery with nanoparticle systems or in combination with viral delivery.[8] Additionally, single-stranded RNA is inherently more fragile than other types of nucleic acids, making it susceptible to premature degradation. To enhance efficiency by improving sgRNA stability, researchers have explored synthetic modifications, such as altering the RNA 2' hydroxyl group to 2' O-methyl (2'OMe) and 2' fluoro (2'F) modifications, and incorporating phosphorothioate bonds. For instance, Yin and colleagues reported that a single intravenous injection of modified sgRNA into mice induced over 80% editing of the *PCSK9* gene in the liver, reducing serum *PCSK9* levels to undetectable levels and significantly lowering cholesterol levels by approximately 35% to 40%.[54] In another study, Finn et al. encapsulated synthetically modified sgRNA with spCas9-encoded mRNA in a lipid nanoparticle (LNP) vehicle. They demonstrated that a single administration resulted in significant editing of the mouse transthyretin (Ttr) gene in the liver, achieving a reduction of more than 97% in serum protein levels that persisted for at least 12 months.[55] However, the inherent limitations of mRNA delivery remain a major obstacle to effective CRISPR gene editing,[56,57] which will be discussed in detail in the following section.

2.2 mRNA-Based Therapeutics

2.2.1 The Development of mRNA-Based Therapeutics

The structure and function of mRNA have been extensively studied since its initial identification in the 1960s (Figure 3).[58-61] Generally, mRNA is a single-

stranded RNA molecule that corresponds to the genetic sequence of a gene and serves as the template for protein translation by ribosomes.[62] While mRNA-based therapeutics have emerged as one of the most promising and commercially successful innovations in modern medicine, their development has encountered various challenges over the years.[63] In late 1987, Robert Malone pioneered the mixing of mRNA with lipid droplets, leading to protein expression in human cells.[64] Following this, Jon A. Wolff successfully utilized *in vitro* transcription (IVT) mRNA to achieve transfection and expression in mouse skeletal muscle cells, demonstrating the feasibility of mRNA therapy in 1990.[65] Since then, advancements in mRNA manufacturing and intracellular delivery strategies have facilitated significant progress in mRNA-based therapies. Today, mRNA-based therapeutics are utilized in a variety of applications, including protein replacement therapy,[66] vaccines,[67] immunotherapeutics,[68] genomic editing,[69] and targeting delivery drugs.[70] Notably, the rapid development and widespread deployment of mRNA vaccines over the past five years have been instrumental in addressing the COVID-19 pandemic.[71] The success of nucleoside-modified mRNA lipid nanoparticle (LNP) vaccines developed by Moderna and Pfizer/BioNTech against SARS-CoV-2 represents a pivotal moment, solidifying mRNA therapeutics as a viable approach in contemporary medicine. In 2023, because of discoveries concerning nucleoside base modifications that enabled the development of effective mRNA vaccines against COVID-19, Katalin Karikó and Drew Weissman won the Nobel Prize in Physiology or Medicine.

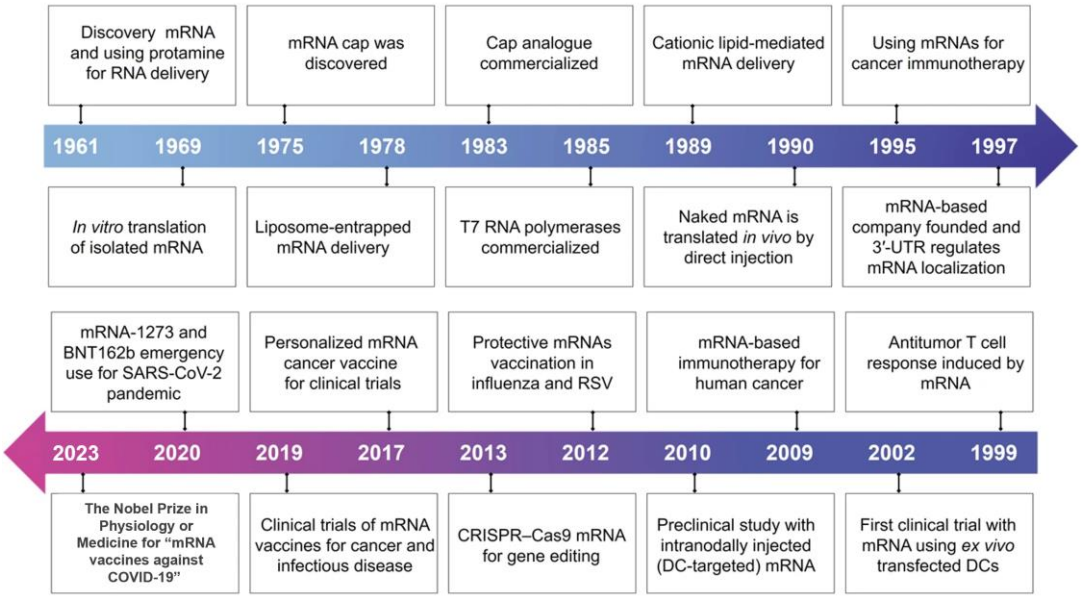

Figure 3. The development of mRNA-based therapeutics. Reproduced from Ref.72 Copyright ©2022, with permission from Springer Nature.

2.2.2 Structure and Pharmacology of Therapeutic mRNA

To understand the mechanism and pharmacology of mRNA therapeutics, it is crucial to clarify the structure of mRNA. Therapeutic mRNA is synthesized through IVT to closely resemble natural mRNA found in the eukaryotic cytoplasm.[73] IVT mRNA can function in the cytosol via *ex vivo* transfection of cells that are then adoptively transferred or through direct *in vivo* delivery. Both methods allow the target cells to synthesize the encoded protein in situ, with mRNA serving as the template for protein production. IVT mRNA consists of five key structural elements: the 5′ cap, the 5′ untranslated region (UTR), the open reading frame (ORF), the 3′ UTR, and the poly(A) tail.[74] Similar to DNA, mRNA is encoded with codons, which are sequences of three ribonucleotides. The initiation of eukaryotic mRNA translation is a highly regulated process that involves assembling a protein-RNA complex to direct ribosomes to the initiation codon.[72] Once the mRNA enters the cell, cap-dependent translation begins with the recognition of the cap structure by eukaryotic initiation factor 4F (eIF4F) and the formation of the preinitiation complex (PIC). Poly(A)-binding protein (PABP) binds to the poly(A) tail, facilitating the circularization of the mRNA with the assistance of eukaryotic translation initiation factors (eIFs). The 40S ribosomal

subunit then scans for the transcription initiation codon, after which the 60S ribosomal subunit is recruited, leading to the release of eIFs and the initiation of amino acid chain extension. Consequently, mRNA is decoded within the ribosome to produce a specific amino acid chain or polypeptide.[75,76] Thus, IVT mRNA is engineered to replicate the endogenous mRNA processing mechanisms to ensure effective protein translation *in vivo*. The final protein's structure and function are determined by the coding sequence within the mRNA. For instance, the protein produced from mRNA vaccines serves as an antigen, capable of eliciting robust pathogen-specific humoral and cell-mediated immune responses.[67] Therefore, engineered IVT mRNA can be tailored to deliver specific proteins to targeted cellular compartments, optimizing their functional effects.

2.2.3 Advantages and Challenges to mRNA Delivery

Advantages

While mRNA vaccines have showcased the potential of mRNA delivery in gene therapy, the therapeutic applications of mRNA extend well beyond infectious disease vaccines. mRNA-based therapeutics offer several distinct advantages.[7,8] One significant benefit is the ability to achieve transient expression, allowing for controlled and time-limited therapeutic effects.[72] This characteristic reduces the risk of insertional mutagenesis and genomic integration, enabling more precise and safer delivery while preserving the integrity of the host genome.[56] Coupled with their lower immunogenicity compared to viral vectors, these factors highlight the safety and increasing interest in mRNA-based CRISPR-Cas9 delivery.[8] Moreover, mRNA holds broad potential for treating diseases that require protein expression, enhancing therapeutic efficacy through bioengineered structures and modified ribonucleotides. The use of nanomaterial carriers further optimizes the pharmacokinetics of nucleic acid drugs, providing adjustable delivery profiles. However, despite these advantages, the efficient delivery of mRNA *in vivo* and *in vitro* remains a significant challenge, limiting the full potential of mRNA-based therapeutics.[56]

Challenges based on mRNA structure

As previously noted, mRNA is inherently unstable due to its long single-stranded nature, which can span kilobases and form complex secondary structures, making it susceptible to degradation by nucleases both *ex vivo* and *in vivo*.[57] Natural base modifications and site-specific introduction of artificial nucleotides not only enhance mRNA stability but also reduce its immunogenicity. Bin Li compared luciferase mRNA and enhanced green fluorescent protein (eGFP) mRNA modified with N1-methylpseudouridine (m1ψ), 5-methoxyuridine (5moU), and pseudouridine (ψ).[77] Their findings indicated that chemical modifications significantly improved protein expression, with 5moU-modified eGFP mRNA demonstrating greater stability than the other variants. Similarly, Melamed and colleagues reached a comparable conclusion in their study of IV-injected lipid nanoparticles formulated with reporter mRNA incorporating various base modifications.[78] They reported that m1ψ-modified mRNA significantly reduced innate immunogenicity compared to unmodified mRNA.

There is a balance between the processes of mRNA translation and decay.[72] Structural elements of mRNA, particularly the 5′ cap and the poly(A) tail, play a crucial role in both translation and degradation.[67] The 5′ cap protects mRNA from 5′ to 3′ exoribonucleases, while the length of the poly(A) tail influences 3′ to 5′ exonucleolytic decay.[74] Given the importance of these functional elements, numerous studies have focused on optimizing mRNA structure. Approaches include developing various 5′ cap analogs,[79] modifying poly(A) tail lengths,[80] screening different UTRs,[81] and encoding various functional peptides within the ORFs.[82] The 7-methylguanosine (m7G) found in 5′ caps facilitates translation initiation by linking the subsequent nucleotide through a 5′-5′ triphosphate bridge (ppp) in eukaryotes.[83] Therefore, modifying m7G is a critical strategy for enhancing mRNA translation efficiency. Studies have shown that replacing the m7G with 7-benzylated guanosine significantly enhances translation efficiency.[84] Additionally, another synthetic 5′ cap analog based on phosphorothioate has improved RNA stability and translational efficiency *in vivo*

in mice.[85]

Challenge on biomembrane crossing

Crossing the biomembrane presents a significant obstacle to mRNA delivery. Once mRNA formulations extravasate into the interstitium, they must traverse the cell membrane to reach the cytoplasm. However, the cell membrane poses a formidable barrier, particularly for naked mRNAs.[8] As negatively charged and hydrophilic macromolecules, mRNAs cannot cross cell membranes passively, which limits their cellular uptake.[86] To address this challenge, various methods and vehicles for mRNA delivery have been developed, including viral vectors,[87] mechanical transfections,[88] and nonviral carriers.[89] For example, Melanie Galla and colleagues created mouse leukemia virus-based vectors encoding the site-specific recombinase Cre for receptor-mediated, dose-controlled, and transient nucleic acid delivery into targeted cells.[90] These vectors were engineered to disable the primer binding site, preventing the reverse transcription of the virion mRNA. Their research revealed that the effective transfer of Cre required a retroviral packaging signal, cap-proximal positioning of the translation unit, and the expression of gag and env proteins in producer cells, illustrating that retroviral mRNA transfer serves as a potential immediate translation template, provided it is not reverse transcribed. However, viral vectors also have disadvantages, including potential carcinogenicity, high immunogenicity, limited gene packaging capacity, and challenges with large-scale production.[91] After cellular internalization, endosomal entrapment of the nanocarrier presents another major hurdle to effective mRNA delivery, often contributing to low transfection efficiency.[92] While the mechanisms of endosomal escape for nanocarriers are not fully understood, several widely accepted hypotheses exist,[93,94] including the proton sponge effect,[95] membrane pore formation,[96] and membrane fusion.[97] Thus, selecting an appropriate carrier that facilitates both cellular internalization and endosomal escape is essential for the success of mRNA-based therapeutics.[92]

2.3 Non-viral Delivery Strategies with CRISPR mRNA/sgRNA

Non-viral vectors have emerged as a promising alternative for addressing the challenges associated with mRNA delivery. Compared to viral vectors, non-viral gene vectors provide several key advantages, such as an abundance of raw materials, flexible chemical compositions, customizable topology, higher DNA loading capacity, lower toxicity, easier preparation, and reduced immune reactions.[98,99] These features make non-viral vectors a valuable tool for gene therapy and other mRNA-based therapeutics. However, for the co-delivery of Cas9 mRNA and sgRNA, the efficiency of each component must be carefully optimized to ensure effective gene editing. Various non-viral delivery strategies are under investigation, including polymeric carriers,[100] LNPs,[101] extracellular vesicles (EVs),[102] carbon spots,[103]and more.[49,53,104]

2.3.1 Polymeric Carriers

In recent decades, polymeric carriers have played a crucial role in delivering a wide variety of nucleic acids, including DNA[105,106], RNAs[107-109], and oligonucleotides[110,111], These carriers offer numerous advantages, such as simple synthesis, structural flexibility, ease of functionalization, and degradability, making them highly effective for gene therapy and other applications.[112] Polymeric nanoparticles, which typically range from 100–500 nm,[113] have been particularly useful for nucleic acid delivery, including CRISPR-Cas9 cargoes. They function similarly to lipid nanoparticles (LNPs), encapsulating CRISPR components into positively charged complexes that can facilitate cellular uptake via endocytosis. Various types of polymers have been explored for CRISPR-Cas9 delivery, such as dendrimers[114], PEG-based nanocarriers[115], poly(β-amino ester)s (PBAEs)[114], supramolecular polymers[116], and degradable polymers, like polypeptides[6] and polysaccharides[117]. These polymers help overcome the challenges associated with efficient intracellular delivery, endosomal escape, and protection from enzymatic degradation. For instance, in a recent study, Blanchard et al. used PBAE-based polymers to

deliver Cas13a mRNA to mitigate influenza virus A and SARS-CoV-2 infections in mice and hamsters.[118] When administered via nebulization, the Cas13a system significantly reduced viral replication and symptoms in infected animals. Similarly, Kataoka's group developed a block-copolymer system using polyethylene glycol and poly(aspartamide) to create Cas9 mRNA/sgRNA polyplex micelles for genome editing in the brain.[100] This co-encapsulation strategy enhanced sgRNA stability, leading to highly efficient genome editing in various brain cells. Another example comes from Sukhorukov's research, where polymeric and hybrid microcarriers, made from degradable polymers and modified with a silica shell, were used to deliver CRISPR-Cas9 components to HEK293T cells.[104] These microcarriers outperformed commercially available liposome-based transfection reagents, achieving higher transfection efficiencies (>70% for mRNA and >40% for plasmid DNA). These examples highlight the potential of polymeric carriers for advancing CRISPR-based therapies by improving delivery efficiency and overcoming biological barriers.

2.3.2 Lipid-Based Nanoparticles

Lipid-based nanoparticles, particularly cationic and ionizable lipids, have emerged as leading nonviral vehicles for mRNA delivery. The most commonly used lipid nanoparticles include N-(1-(2,3-dioleyloxy) propyl)-N,N,N-trimethylammonium chloride (DOTMA), the first synthetic cationic lipid, which has been applied to deliver mRNA into several cell lines.[64] Cationic lipids such as DOTMA facilitate the encapsulation of negatively charged nucleic acids, such as mRNA, into positively charged liposomes, which aids in their fusion with cell membranes and promotes cellular entry.[119] Ionizable lipids, when combined with other components, form lipid nanoparticles (LNPs), a delivery system widely recognized for its clinical advancement in mRNA-based therapies.[120] LNPs have been demonstrated as highly efficient for delivering CRISPR systems, whether in plasmid form or as a combination of Cas9 mRNA and sgRNA.[7] These platforms, originally developed for delivering plasmids and siRNAs, are often directly adaptable for CRISPR without significant modification. The efficacy of LNPs for CRISPR delivery has been validated in

multiple studies. For example, Daniel Rosenblum et al. developed LNPs using ionizable amino lipids with hydrazine, hydroxylamine, and ethanolamine linkers, along with linoleic fatty acid chains.[121] In their study, a single intracerebral injection of CRISPR-LNPs targeting *PLK1* (sgPLK1-cLNPs) in aggressive glioblastoma models achieved up to 70% gene editing *in vivo*, leading to significant tumor cell apoptosis, 50% tumor growth inhibition, and a 30% improvement in survival. Moreover, antibody-targeted LNPs increased gene editing efficiency to 80%, inhibited tumor growth, and improved survival by 80%. Another study by the Michael J. Mitchell group utilized a barcoded high-throughput screening system to evaluate 180 cationic, degradable lipids for LNP-based Cas9 mRNA/sgRNA co-delivery.[119] Their results demonstrated that this LNP platform significantly reduced *VEGFR2* expression in lung endothelial cells, indicating its potential in antiangiogenic therapy for tumor suppression. It also outperformed the gold-standard lung-tropic MC3/DOTAP LNP system in a lung tumor model, highlighting the versatility and efficiency of LNPs for CRISPR-Cas9 applications.[122] While LNP delivery holds significant promise, it still requires further research and optimization to address challenges related to low encapsulation efficiency, main accumulation in the liver and kidney, and stability in transport and storage.[123] By contrast, polymer-based approaches have a significant variety of formulations and more flexibility for modifications, making them more possibilities for gene therapy applications.[124] Parts of reported lipid and polymer materials for gene delivery are shown in Figure 4.[125] Nevertheless, the unique advantages of LNPs, such as low toxicity and efficient bioavailability, highlight the need for continued investigation into their design and development for therapeutic applications. Ultimately, both approaches have distinct advantages and limitations, and future innovations may combine the strengths of both strategies for more effective and safer mRNA-based therapies.

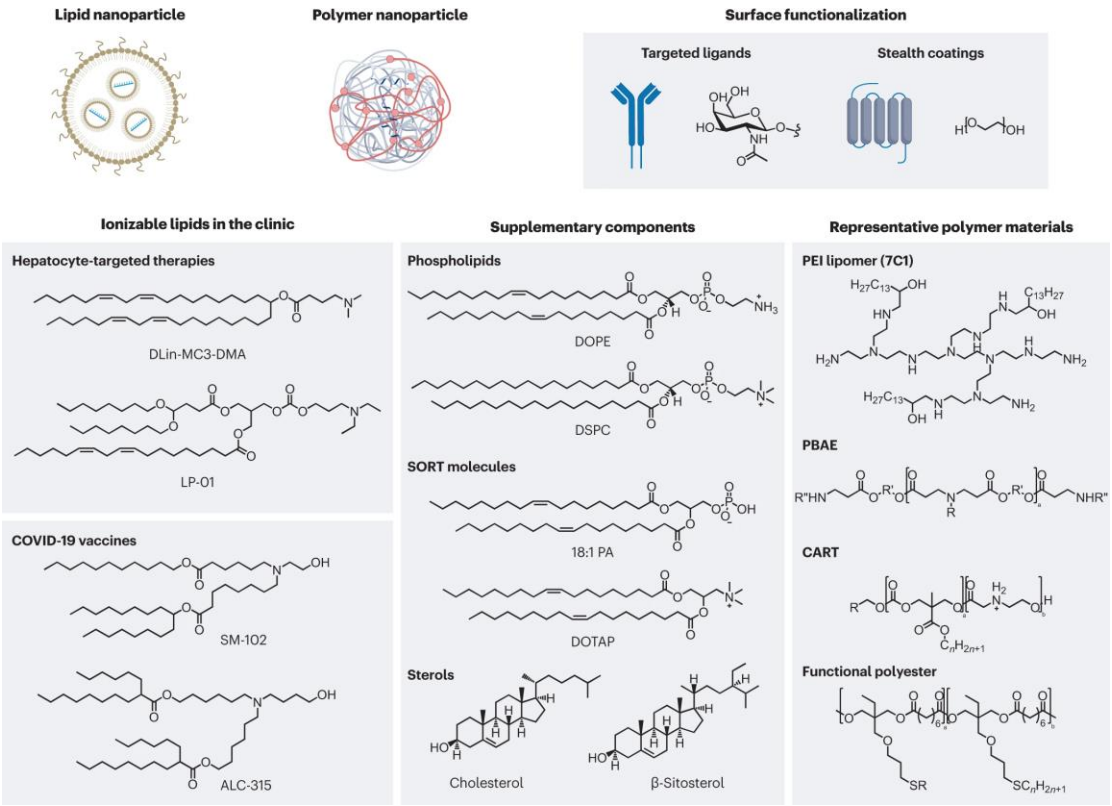

Figure 4. Self-assembled nanoparticles based on lipid and polymer materials are the state of the art for the delivery of genetic drugs. With permission from Ref.125 Copyright © 2023, Springer Nature.

2.3.3 Other Formulations

Several studies have explored alternative materials for CRISPR delivery beyond traditional lipid and polymer-based platforms,[49] such as extracellular vesicles (EVs)[102] and carbon-based nanomaterials (Carbon Dot).[103] EVs, including apoptotic EVs, ectosomes, and exosomes, are nanosized membrane-bound vesicles secreted by various cell types.[126] These vesicles carry a range of biomolecules, such as proteins, lipids, and nucleic acids, from their parent cells, making them key mediators of intercellular communication. EVs play critical roles in both physiological and pathological processes. Due to their natural biogenesis, EVs possess several advantages as gene delivery systems over traditional synthetic vehicles, including high biocompatibility, enhanced stability, and reduced immunogenicity.[127] These features make EVs a promising platform for therapeutic delivery, particularly red blood cell-derived EVs (RBCEVs), which offer a promising approach for delivering CRISPR

components. In a study by Tin Chanh Pham and colleagues, RBCEVs were generated in large-scale quantities and utilized for RNA drug delivery.[102] They designed a gRNA targeting the human mir-125b-2 locus, an oncogenic microRNA implicated in leukemia. The treatment resulted in a 98% reduction in miR-125b expression and a 90% reduction in miR-125a after just two days, demonstrating the potential of RBCEVs as effective carriers for CRISPR-Cas9 genome editing in leukemia cells. In another study, Akbar Hasanzadeh and his team developed fluorescent nitrogen- and zinc-doped carbon dots (N-Zn-doped CDs) through one-step microwave-aided pyrolysis using citric acid, branched PEI25k, and zinc salts.[103] These carbon dots exhibited a quantum yield of around 60% and were effective in delivering mRNA into HEK 293T cells. Moreover, they mediated high gene disruption efficiency by delivering CRISPR-Cas9 into HEK 293T-GFP cells, effectively disrupting the GFP gene. The N-Zn-doped CDs also displayed remarkable photoluminescence properties, making them versatile nanovectors with excellent transfection efficiency for both CRISPR-Cas9 and mRNA delivery. These findings highlight the growing range of materials being developed to overcome the challenges of CRISPR delivery, offering new avenues for efficient and targeted gene editing therapies.

2.4 Applications of CRISPR Delivery

CRISPR, initially developed as a tool for generating simple genetic mutants, has evolved into a versatile platform capable of a wide range of genomic modifications. These tools can now replace, rearrange, silence, activate, and remodel genomic elements, making CRISPR one of the most flexible and user-friendly methods for genome manipulation across nearly any cell type. This versatility opens up new possibilities for exploring the genetic underpinnings of diseases and developing therapeutic approaches.

2.4.1 Animal Models

CRISPR-based genome editing, a technology derived from bacterial defense mechanisms, is transforming the way gene function is studied across nearly all

model organisms, from flies to primates. This breakthrough has significantly advanced animal modeling for a wide range of diseases. Among the most commonly used model organisms, the mouse has been at the forefront of CRISPR research. By directly injecting Cas9 mRNA and sgRNAs into fertilized zygotes, researchers have been able to generate genome-edited mice with single (95%) or double mutations (70–80%) at remarkably high efficiency.[128] As a result, CRISPR-generated mutant mice have become a popular and relatively affordable tool offered by commercial entities and research institutions alike, enabling even labs with minimal experience in mouse models to create custom genetic tools for their studies. CRISPR's application in mice has led to the development of models for diseases like medulloblastoma (MB) and glioblastoma (GBM).[129] For example, Gronych's group successfully applied PEI-mediated transfection or in-utero electroporation to deliver CRISPR components into the developing mouse brain, targeting genes such as Ptch1, Trp53, Pten, and Nf1. They found that the deletion of Ptch1 in Trp53-deficient mice induced MB, while GBM could be triggered by targeting Nf1, Pten, and Trp53. These findings align with previous research on these cancers. Although large animals are not traditionally popular model organisms, CRISPR has also proven successful in disease modeling in species such as pigs due to their unique advantages in specific research areas. For instance, Hai et al. designed an sgRNA targeting exon 5 of the pig vWF gene, which, when mutated, causes von Willebrand disease (vWD) in humans.[130] They observed that pigs with biallelic mutations exhibited prolonged bleeding times (512 ± 121 minutes) compared to wild-type pigs (34 ± 11 minutes), mimicking the human vWD phenotype. Similar studies are underway to generate gene-targeted dogs and monkeys for disease modeling.[131,132] While CRISPR-based animal models are efficient and offer rapid generation times, there are limitations. These models involve constitutive germline modifications, making it difficult to study homozygous disruptions of essential genes or non-synonymous mutations that affect embryonic development. Additionally, variations in phenotypes among founders due to allelic segregation, low frequencies of multiplexed knock-in mutations, and random indels in most alleles can complicate analyses and studies.[128]

2.4.2 Monogenic Disease

The application of CRISPR-Cas genome editing tools for treating monogenic diseases is an emerging and promising strategy with the potential to create personalized therapies. By enabling the precise correction of gene mutations, CRISPR offers a significant opportunity to restore normal gene function in patients with monogenic disorders. However, the complexity of these diseases often requires patient-specific genome editing strategies, which take into account DNA repair mechanisms, the type of CRISPR-Cas system used, and the method of delivery. Different CRISPR-Cas systems, each with unique enzymatic capacities, must be tailored for various therapeutic applications. Of the approximately 20,000 protein-coding genes in the human genome, nearly 4,000 have been implicated in monogenic diseases.[133] Genetic lung disorders, such as surfactant protein (SP) deficiency, cystic fibrosis (CF), and alpha-1 antitrypsin (AAT) deficiency, are a major category of these diseases.[134] Many infants and children suffer from severe respiratory failure due to limited treatment options, often resulting in death. Recent advances in CRISPR-Cas gene editing provide a new approach for repairing or inactivating disease-causing mutations. For example, Alapati et al. demonstrated that intra-amniotic delivery of CRISPR-Cas9 during fetal development can achieve targeted gene editing in the lungs of mice with SP deficiency.[135] Their study showed that inactivation of the mutant *Sftpc*^{I73T} gene, responsible for severe lung damage, improved lung morphology and increased survival in postnatal mice. The therapeutic potential of CRISPR-Cas extends beyond lung diseases. CRISPR-Cas technology has also shown positive results in animal models of other monogenic diseases. These include Leber congenital amaurosis (LCA),[136] a mutation in the ornithine transcarbamylase (OTC) gene,[137] and Fanconi anemia (FA).[138] These developments highlight the potential of CRISPR-Cas to treat a wide range of genetic disorders, bringing hope to patients who previously had few or no treatment options.[133]

2.4.3 Neurodegenerative Diseases

Neurodegenerative diseases (ND) are a diverse group of disorders marked by the progressive deterioration of the central and peripheral nervous systems. Among the most common NDs are Alzheimer's disease (AD), Parkinson's disease (PD), and Huntington's disease (HD), all of which share a notable characteristic: the lack of effective therapies.[139,140] Current treatments primarily manage symptoms without halting or reversing disease progression. In this context, the CRISPR system, known for its precision, affordability, and simplicity, has attracted significant attention for its potential to modify defective genes and offer therapeutic solutions for NDs.[141] AD is a fatal neurodegenerative disorder and the leading cause of dementia, primarily affecting older adults. It progressively worsens, typically leading to death within 5 to 10 years of diagnosis.[142] A key genetic factor in AD is the *APPswe* mutation in the amyloid precursor protein (APP) gene, which enhances the cleavage of the amyloid-β (Aβ) precursor protein by β-secretase, leading to increased Aβ levels—a hallmark of AD pathology. In a proof-of-concept study, György and colleagues demonstrated that CRISPR-Cas9 could selectively disrupt the *APPswe* allele, both in *ex vivo* and *in vivo* models, leading to a reduction in pathogenic Aβ. This approach holds potential as a gene therapy for AD caused by the *APPswe* mutation and other mutations that elevate Aβ levels.[143] PD is another common neurodegenerative disorder, characterized by the loss of dopaminergic neurons, leading to motor dysfunction. Despite extensive research, no therapy has been found that halts the progression of PD.[144] Genetic risk factors for PD include mutations in genes such as *SNCA*, *LRRK2*, *Parkin*, *DJ-1*, and *p13*.[145] In a study, Arasaki and colleagues utilized CRISPR-Cas9 to generate a knockout mouse model lacking *p13* expression. They observed that heterozygous knockout of *p13* mitigated toxin-induced motor deficits and prevented the loss of dopaminergic neurons in the substantia nigra, suggesting that the knockdown of p13, a mitochondrial protein, could protect against PD.[146] These promising applications of CRISPR-Cas9 in AD and PD research showcase its potential for developing gene-editing therapies for NDs, providing hope for addressing these currently untreatable diseases.

2.4.4 Cancer Therapy

Initially, gene therapy aimed to manage genetic diseases, but it has since expanded to address both acquired and inherited disorders. Cancer arises from a series of genomic and epigenomic alterations, often leading to the activation of oncogenes or inactivation of tumor suppressor genes.[147] Since mutations are a leading cause of cancer and complicate the development of effective therapeutics, genetic engineering, particularly CRISPR-Cas9, has become essential in cancer treatment. Research utilizing CRISPR components to treat cancer generally focuses on two main strategies. The first involves epigenome editing of cancer cells for therapeutic purposes. Epigenetic modifications, such as DNA methylation and histone modifications, create an environment that regulates gene expression, influencing cell proliferation and differentiation. Histone proteins, which package DNA in eukaryotic cells, undergo various reversible modifications, including ubiquitination, phosphorylation, SUMOylation, and acetylation, all regulated by specific enzymes.[148] Given that a significant portion of human cancers result from global methylation loss or hypermethylation at specific loci, advancements in epigenome editing tools will be crucial in cancer treatment.[149] For example, a study by Anastas et al. revealed that knocking out *KDM1A*, which encodes lysine-specific demethylase 1 (LSD1), sensitizes diffuse intrinsic pontine glioma (DIPG) cells to histone deacetylase (HDAC) inhibitors.[150] Co-inhibiting *LSD1* and *HDACs* with Corin reduced *DIPG* growth by reprogramming chromatin, inhibiting the cell cycle while promoting cell death and differentiation. Additionally, noncoding RNAs (ncRNAs) play a significant role in the epigenetic regulation of cancer genes and their pathways. CRISPR-Cas9-mediated editing of ncRNAs offers a promising approach to cancer treatment.[151] Zhou et al. used CRISPR-Cas9 to knockout miR-3188 in hepatocellular carcinoma (HCC) cell lines, demonstrating that this knockout suppressed cell growth, migration, and invasion while inhibiting tumor growth in nude mice.[152] Recently, Yu et al. reported that modulating the expression of colon cancer-associated transcript-2 (CCAT2), a long noncoding RNA (lncRNA), regulates miR-145 expression in colon cancer cells.[153] They found that knocking out *CCAT2* with CRISPR

increased miR-145 levels and negatively regulated miR-21 in HCT-116 cells, impairing proliferation and differentiation.

The second strategy focuses on directly targeting oncogenes or tumor suppressor genes. Cancer is often associated with mutations in these genes. Many oncogenes and tumor suppressor genes, such as Kirsten rat sarcoma virus (*KRAS*), epidermal growth factor receptor (*EGFR*), *C-myc*, *p53*, and *BRCA1/2*, are known to drive cancer development and progression.[154] Lung cancer, the most common malignancy worldwide, poses significant morbidity and mortality challenges.[1] Approximately 15% of non-small cell lung cancer cases involve mutations in the *EGFR* gene, which is critical for tumor progression.[155] Koo et al. successfully targeted an *EGFR* oncogene with a specific single-nucleotide missense mutation (CTG > CGG), achieving precise disruption at the mutation site.[156] Their findings showed that CRISPR-Cas9-mediated disruption of the mutant allele significantly enhanced cancer cell killing and reduced tumor volumes in xenograft models, with tumor size reductions of 81.5% and 78.3% compared to controls. *KRAS*, a frequently mutated oncogene in various cancers, including lung, colon, and pancreatic cancers, plays a pivotal role in cancer initiation and maintenance.[157] Targeting mutant *KRAS* alleles with CRISPR has been shown to inhibit cancer cell proliferation both *in vitro* and *in vivo*.[158] In xenograft models, tumor weights in mice implanted with SW403 or SW480 cells targeted by CRISPR for *KRAS* c.35G>T were reduced by 7.2-fold and 10-fold, respectively. Additionally, other strategies can complement CRISPR for cancer therapy.[147,159] Editing drug-resistance genes can enhance the sensitivity of malignant cells to chemotherapeutics, improving treatment efficacy. For example, a study demonstrated that knocking out the *RSF1* gene in H460 and H1299 cells, in combination with paclitaxel, resulted in G1 cell-cycle arrest, increased apoptosis, and reduced cell migration and proliferation.[160]

2.4.5 Others

Moreover, numerous clinical applications have emerged from CRISPR gene editing.[161] Due to its significant benefits in treating various cancers, cancer

immunotherapy is a rapidly growing field. Rather than directly attacking tumors, cancer immunotherapy harnesses the body's adaptive or innate immune responses to combat cancer using various strategies.[162] One approach involves modifying T cells through the CRISPR system to enhance their antitumor properties, thereby mobilizing the patient's immune system to eliminate tumor cells.[72] Recent studies have reported the efficient generation of clinical-scale gene-disrupted chimeric antigen receptor (CAR) T cells with strong anti-tumor activity and reduced alloreactivity using multiplex CRISPR technology.[163] These CAR T cells hold promise as off-the-shelf universal T cells. Furthermore, by employing multiplex genome editing to disrupt the *PD1* gene, these CAR T cells demonstrated enhanced anti-tumor activity in both *in vitro* and animal models.[164] Additionally, mRNA-based genome editing has been successfully applied to stem cells for treating various diseases.[165] In 2023, the first CRISPR/Cas9 gene editing therapy, Casgevy (Exagamglogene autotemcel), received approval in the UK and US for treating sickle cell disease (SCD).[166] This gene therapy involves modifying the recipient's blood stem cells, which are then reinfused as a one-time treatment during a hematopoietic stem cell transplant for patients aged 12 and older, including those experiencing recurrent vaso-occlusive crises.[167]

2.5 Perspectives

Genome editing has entered a flourishing period of development in recent years, driven by its extensive potential for scientific research and disease treatment. The advent of the CRISPR-Cas system is revolutionizing methodologies in biology, medicine, agriculture, and industry, ushering in a new era of innovation. With advancements in mRNA-based therapeutics and their delivery methods, CRISPR has the potential to become a reliable and widely adopted genome editing tool across various fields, provided that challenges related to delivery efficiency, biosafety, and system performance are addressed. However, like many emerging technologies, the CRISPR-Cas system faces significant challenges, particularly regarding government regulation and social ethics. In 2018, Jiankui He announced the creation of the first genetically edited human

babies, claiming they had been made resistant to the human immunodeficiency viruses (HIV).[168] This revelation sent shockwaves through both society and the scientific community, provoking widespread controversy and condemnation due to the bypassing of established scientific and clinical protocols. Such actions raised serious ethical concerns and highlighted the potential dangers of genome editing technology when applied irresponsibly.

As we look to the future, the advances in CRISPR-Cas technology hold the potential to significantly impact people's lives. Scientists are making remarkable progress in understanding and applying CRISPR-based techniques. We can expect an increasing number of CRISPR-driven therapies, medicines, and vaccines.[161,169] Examples include CTX112™ (NCT05643742) and CTX131™ (NCT05795595) for allogeneic CAR T cell treatments targeting lymphoid and solid tumors,[170] a CRISPR formulation (NCT04560790) targeting herpes simplex virus 1 (HSV-1) in herpetic stromal keratitis (HSK),[171] and NTLA-2001 (NCT04601051) for transthyretin (ATTR) amyloidosis.[172]

Overall, CRISPR-Cas technology continues to evolve rapidly, alongside advancements in mRNA delivery. The intersection of CRISPR gene editing and mRNA-based therapeutics presents both exciting opportunities and challenges, shaping the future of precision medicine.

3. Aims of The Projects

This Ph.D. thesis primarily aims to screen various polymeric materials, with a focus on optimizing PEI-based nanoparticles for the co-delivery of Cas9 mRNA and sgRNA specifically targeting *KRAS*-mutated lung cancer. As previously discussed, mRNA-based CRISPR gene editing represents a promising approach for addressing challenging targets such as *KRAS* mutations in lung cancer. However, effective delivery of mRNA remains hindered by multiple barriers. Therefore, the urgent development of safe and efficient polymers for CRISPR-Cas9 mRNA and sgRNA delivery is essential in this field. The project involves developing a novel PEI-based micelleplex, optimizing its formulation, and exploring receptor-targeted applications through ligand conjugation. The objectives for each chapter are summarized as follows:

Chapter 1. focuses on screening polymeric materials for mRNA delivery. This chapter includes the synthesis and characterization of a lipid-modified PEI-based polymer, C14-PEI. A novel micelleplex is then prepared using C14-PEI, with *in vitro* assessments of eGFP mRNA expression and gene editing mediated by Cas9 mRNA and sgRNA.

Chapter 2. utilizes a di-block anionic polymer (PEG-PLE) to coat and shield the surface charges of C14-PEI nanoplexes. This chapter aims to optimize the properties of the nanoplexes and enhance mRNA expression and gene editing efficiency specifically targeting the *KRAS* mutation in lung cancers.

Chapter 3. explores the potential for Erbb3 receptor-targeted applications of C14-PEI conjugated with ligands in *KRAS* mutant lung cancer. This chapter discusses the development of affibody conjugation methods with polymers and evaluates the effects of various formulation and conjugation approaches on polyplex preparation and performance.

4. Chapter I

A Novel Micelleplex for Tumour-Targeted Delivery of CRISPR-Cas9 against KRAS-Mutated Lung Cancer

Siyu Chen,[1] Mariem Triki,[1] Simone Pinto Carneiro,[1] and Olivia Monika Merkel[1]

[1]Ludwig-Maximilians-University, Department of Pharmacy, Pharmaceutical Technology and Biopharmaceutics, Butenandtstraße 5-13, Munich, 81377, Germany

The following sections are adapted from the submitted manuscript.

4.1 Abstract

CRISPR-Cas9 has emerged as a highly effective and customizable genome editing tool, holding significant promise for the treatment of KRAS mutations in lung cancer. In this study, we introduce a novel micelleplex, named C14-PEI, designed to co-deliver Cas9 mRNA and sgRNA efficiently to excise the mutated KRAS allele in lung cancer cells. C14-PEI is synthesized from 1,2-epoxytetradecane and branched PEI 600 Da via a ring-opening reaction. The resulting C14-PEI has a critical micelle concentration (CMC) of approximately 20.86 ± 0.15 mg/L, indicating its ability to form stable micelles at low concentrations. C14-PEI efficiently encapsulates mRNA into micelleplexes through electrostatic interactions. When the mass ratio is 8 (w/w 8), the C14-PEI formulation exhibits conductive properties, which showed encapsulation efficiency of eGFP mRNA at 99% and led to a 130-fold increase in eGFP expression in A549 cells compared to untreated cells, demonstrating the robust delivery and expression capability of the micelleplexes. Importantly, toxicity tests using intracellular reduction of a tetrazolium salt revealed no significant cytotoxicity, underscoring the biocompatibility of C14-PEI. C14-PEI also shows high efficiency in co-encapsulating Cas9 mRNA and sgRNA, as confirmed by agarose gel electrophoresis. At an sgRNA to Cas9 mRNA molar ratio of 10, the

micelleplexes successfully mediate the cutting of mutated *KRAS* with an indel efficiency exceeding 60%, as determined by the T7 Endonuclease I (T7EI) assay. Droplet digital PCR (ddPCR) further demonstrates that the gene editing efficiency, measured by edited gene copies, is 48.5% in the w/w 4 group and 37.8% in the w/w 8 group. Treatment with C14-PEI micelleplexes containing Cas9 mRNA and sgRNA targeting the *KRAS* G12S mutation significantly impairs the migration capability of A549 cells and increases apoptosis rates. These findings suggest that C14-PEI effectively disrupts *KRAS* signaling pathways, leading to reduced tumor cell proliferation and enhanced cell death.

4.2 Introduction

According to the Global Cancer Statistics 2022, lung cancer is the most commonly diagnosed cancer and the leading cause of cancer-related death.[1] Lung cancer may be induced by a variety of genomic variations, such as *EGFR*, *ALK*, and *MET*. Among these mutations, Kirsten rat sarcoma 2 viral oncogene homolog (*KRAS*) mutations are observed in 25% of all cases, making it the most commonly mutated gene.[173] Although *RAS* genes were the first human oncogenes to be identified, mutant *KRAS* has long been considered an undruggable target due to its spherical structure. The relatively smooth shape of the protein made it difficult to design inhibitors that could bind to surface grooves, stalling progress in drug development for many years.[174] Despite decades of research, significant progress in *KRAS* drug discovery remained elusive until the pivotal discovery in 2013 of covalently targeting the *KRAS* p.Gly12Cys (G12C) mutation, which catalysed transformative advancements in *KRAS*-targeted therapy[4]. To date, two small molecule inhibitors, Sotorasib and Adagrasib, have received accelerated approval for the treatment of non-small cell lung cancer (NSCLC) harbouring *KRAS* G12C mutations.[175] Moreover, pan-RAS/KRAS inhibitors, combination strategies, and immunotherapeutic approaches have shown significant progress from bench to bedside.[174] However, the adaptive resistance and toxicity of pan-RAS inhibitors remain challenging drawbacks.

Recently, thanks to the discovery of CRISPR-Cas9, gene therapy has seen exciting developments. Clustered regularly interspaced short palindromic repeats (CRISPRs) are a type of repeat sequences found in prokaryotic bacteria and archaea, functioning as part of their adaptive immune system. CRISPR-Cas9 proves to be an efficient and customizable genome editing tool due to its benefits, such as quick onset, transient expression, low off-target effects (OTEs), and low costs.[7] It is a promising strategy for regulating gene expression, especially for correcting pathogenic mutations, and could specifically correct *KRAS* mutations.[3] To deliver CRISPR-Cas9, the most common forms include plasmid DNA,[4] mRNA/sgRNA,[5] and protein/sgRNA ribonucleoprotein complexes (RNPs).[6] Various advantages of the Cas9 mRNA formulation delivery strategy have been reported. First, compared with plasmids, mRNAs only need to enter the cytoplasm to exert its effects.[8] The delivery of the Cas9 mRNA formulation combined with sgRNA into target cells can express the Cas9 protein transiently, which shortens the duration of gene editing and reduces the chance of OTEs.[7] Secondly, the intracellular presence of the Cas9 protein is more persistent after mRNA expression compared to the delivery of Cas9-RNPs,[49] and systemic RNP delivery in clinical settings still requires evaluation compared to more established mRNA-based approaches.[176,177] During the COVID-19 pandemic caused by the SARS-CoV-2 virus, the rapid development and clinical maturation of mRNA-based vaccines promoted advancements in mRNA delivery techniques.[178] Additionally, the ability to modify mRNA sequences to encode regulatory elements provides a means to control the expression of gene-editing tools in a cell-specific manner.[8] In 2013, Shen and colleagues first used the CRISPR-Cas system to cut DNA in zebrafish and mouse embryos using Cas9 mRNA and sgRNA, paving the way for its use in the generation of gene-disrupted animals.[50]

However, unlike mRNA vaccines, the efficiency of each component must be considered in the co-delivery of Cas9 mRNA and sgRNA. Yin and colleagues used nanoparticle-mediated delivery of Cas9 mRNA in combination with adeno-associated viruses (AAVs) encoding an sgRNA and a repair template to edit the *fumarylacetoacetate hydrolase* (*Fah*) gene with significant correction (more

than 6%), demonstrating that this method relies on viral co-delivery to supplement mRNA delivery.[53] Over the past several decades, polymeric nanoparticles have been extensively used to deliver various types of nucleic acids, including plasmid DNA,[105,106] RNAs,[107-109] and oligonucleotides,[110,111] due to their advantages such as facile synthesis, flexible structures and components, ease of functionalization, and degradability.[112] Polymeric nanoparticles are a collective term used for any type of polymer nano-sized particles, specifically polymer nanospheres and nanocapsules, generally ranging from 100 to 500 nm in size.[113] Polycationic polymers mediate the encapsulation of CRISPR-Cas9 cargoes into positively charged complexes to enable endocytosis into cells. To date, various polymers have been employed for intracellular CRISPR delivery, such as dendrimers,[114] PEG-based nanocarriers,[115] poly(β-amino ester)s (PBAEs),[114] supramolecular polymers,[116] and degradable polymers (such as polypeptides[6] and polysaccharides[117]). PEI-based nanoparticles have demonstrated higher editing efficacy compared to unmodified Cas9/sgRNA complexes with conventional lipids.[179] Yue and colleagues constructed a graphene oxide (GO)-polyethylene glycol (PEG)-polyethylenimine (PEI) nanocarrier for the delivery of high-molecular-weight Cas9/sgRNA complexes, showing that the nanocarrier could be successfully used for efficient gene editing in a human gastric adenocarcinoma cell line (AGS cells) with an efficiency of approximately 39%, while also exhibiting high stability to protect sgRNA from enzymatic degradation.[104]

In this study, following a series of screenings, we designed a novel PEI-based micelleplex, C14-PEI, to deliver Cas9 mRNA and sgRNA targeting mutated *KRAS*. We tested the encapsulation efficiency and stability of the polymers, characterized the nanoparticles, and evaluated cytotoxicity and eGFP-mRNA expression of the micelleplexes *in vitro* using A549, H1299, and Hop62 cells. The endosomal entrapment and escape of the micelleplex were also investigated using confocal laser scanning microscopy (CLSM). To achieve therapeutically relevant gene editing, Cas9 mRNA and sgRNA targeting mutant *KRAS* were delivered to A549 cells using the C14-PEI micelleplex, and gene editing efficiency was estimated by T7EI assay, ddPCR, and Sanger

sequencing. Western blot analysis, cell migration assays, and cell apoptosis assays were conducted to evaluate cellular responses after treatment.

4.3 Materials & Methods

4.3.1 Materials

1,2-epoxytetradecane, Branched PEI 600 Da, 4-(2-hydroxyethyl)-1-piperazineethanesul-fonic acid (HEPES), Dulbecco's Phosphate Buffered Saline (PBS), 0.05% trypsin-EDTA, Tris-buffered saline, Tween 20, RPMI-1640, fetal bovine serum (FBS), Penicillin-Streptomycin solution, 6-diamidino-2-phenylindole dihydrochloride (DAPI), skim milk, heparin, pyrene, paraformaldehyde (PFA), agarose powder, and Cell Counting Kit-8 (CCK-8) were purchased from Sigma-Aldrich, Germany. SYBR™ Gold Stain, SYBR Safe DNA Gel Stain, Lipofectamine™ 2000, LysoTracker™ Green DND-26, Annexin V-AF488, GeneArt™ Genomic Cleavage Detection Kit, Phusion Hot Start II High-Fidelity PCR Mastermix, ExoSAP-IT™ Express PCR Product Cleanup Reagent, Pierce™ BCA Protein Assay kit, Novex™ WedgeWell™ 8-16% Tris-Glycin gel, Pierce™ Protease Inhibitor Tablets, RIPA buffer, SuperSignal™ West Femto Maximum Sensitivity Substrat were bought from Thermo Fisher Scientific, Germany. ddPCR NHEJ Gene Edit Assay (primers and probes), ddPCR Supermix for Probes (no dUTP), cartridges, gaskets, droplet generation oil, and droplet reader oil were obtained from Bio-Rad, US. eGFP mRNA (RiboPro, The Netherlands), CleanCap® Cas9 mRNA (5moU) (Trilink Biotechnologies, US), cOmplete™ EDTA-free Protease Inhibitor Cocktail (Roche, Germany), Rotiphorese®NF 10x TBE Buffer (Carl Roth, Germany), propidium iodide (PI) (BD Biosciences, US), DNeasy Blood & Tissue Kit (Qiagen, US), and Amersham™ Protran® Western blotting nitrocellulose membranes (Cytiva technologies, Germany) were purchased from the suppliers indicated. Methanol, ethanol, and acetone were provided by Ludwig-Maximilians-University Munich. The primary antibodies for p44/42 MAPK (Erk1/2), Phospho-p44/42 MAPK (T202/Y204), and AKT were from Cell Signaling, US. KRAS polyclonal antibody, Histone-H3 polyclonal antibody, and

HRP-conjugated affinipure goat anti-rabbit IgG (H+L) secondary antibody are from Proteintech, Germany. Cy5-mRNA was synthesized and labeled in the laboratory. sgRNA (*KRAS* G12S: 5'-CUUGUGGUAGUUGGAGCUAG-3') was synthesized by Sigma-Aldrich. Primers for PCR (F: TTTGAGAGCCTTTAGCCGC, R: TCTACCCTCTCACGAAACTC) and primers for Sanger sequencing (F: TCTTAAGCGTCGATGGAG, R: ACAGAGAGTGAACATCATGG) were synthesized by Sigma-Aldrich.

4.3.2 Cell Culture

A549, H1299, and Hop-62 cells were cultured in complete RPMI-1640 medium supplemented with 10% heat-inactivated fetal bovine serum (FBS) and 1% penicillin-streptomycin. All cells were subcultured, maintained, and grown in an incubator at 37°C in humidified air with 5% CO_2.

4.3.3 C14-PEI Synthesis and Characterization

C14-PEI is prepared by reacting 1,2-epoxytetradecane with branched PEI 600 Dalton (Sigma-Aldrich, Germany) through a ring-opening reaction. Briefly, 1,2-epoxytetradecane and bPEI 600 Da were heated at 95°C in absolute ethanol for 72 h while stirring. The product was then dialyzed with a 1000 Da cut-off in absolute ethanol, followed by ethanol removal using high-pressure nitrogen gas.[180,181] The final polymer was confirmed by nuclear magnetic resonance spectroscopy (^{1}H NMR) and gel permeation chromatography (GPC).

4.3.4 Critical Micelle Concentration

The critical micelle concentration (CMC) of C14-PEI was determined using a fluorescence spectrometer with pyrene as the fluorescence probe.[182] The fluorescence scanning ranged from 300 to 350 nm, and the emission wavelength was set at 373 nm. Pyrene was first dissolved in 0.5 mL of acetone, and the acetone was then allowed to volatilize overnight at room temperature in the dark. The initial polymer solution obtained was diluted into a series of concentrations ranging from 0.0001 to 0.1 mg/mL and added to vials containing

pyrene. The mixture was left to equilibrate in the dark for 24 h before measurement. The final concentration of pyrene in the aqueous solution was $6.5x10^{-7}$ M.

4.3.5 Micelleplex Preparation

Micelleplexes were prepared using C14-PEI and RNA through electrostatic interactions. Briefly, 500 ng of eGFP mRNA and a specific amount of C14-PEI based on mass ratios were dissolved in high-purity water and mixed by pipetting and vortexing in 100 µL of 10 mM HEPES buffer, pH 7.4 or pH 5.4. The mixture was then incubated at room temperature for 1 h. For the co-encapsulation of Cas9 mRNA and sgRNA, a similar method was employed, but Cas9 mRNA and sgRNA were premixed at a molar ratio of 1:10 before diluting in the HEPES buffer. The morphology of the micelleplexes was examined using cryo-electron microscopy (Cryo-EM).

4.3.6 Micelleplex Characterization

The micelleplexes were characterized using a Zetasizer Ultra (Malvern, UK). The micelleplexes suspension was added to a disposable micro-cuvette, and the hydrodynamic diameter and polydispersity indices (PDI) were measured three times per sample using dynamic light scattering (DLS) at a 173° backscatter angle. Subsequently, the same suspension was transferred to a folded capillary cell for each sample to determine the zeta (ζ) potential in triplicate using laser Doppler anemometry (LDA), with each run consisting of up to 100 scans. Results are presented as mean ± standard deviation (SD, n=3).

4.3.7 Encapsulation Efficiency Test

To evaluate the mRNA encapsulation capacity of C14-PEI, SYBR Gold assays were conducted. SYBR Gold is a cyanine dye that binds to nucleic acids and exhibits fluorescence upon intercalation. Briefly, micelleplexes were prepared as described earlier at weight-to-weight (w/w) ratios of 0, 0.5, 1, 2, 4, 8, and 15. Subsequently, 100 µL of each micelleplex suspension was added to black

FluoroNunc 96-well plates (Fisher Scientific, Germany). A 4X SYBR Gold aqueous solution (30 µL per well) was then added to each well and incubated for 10 minutes in the dark. The fluorescence intensity was measured using a fluorescence plate reader (TECAN, Switzerland) with excitation at 485/20 nm and emission at 535/20 nm.[183] The fluorescence intensity of free mRNA (w/w = 0) was used as a control and set as 100% fluorescence.

4.3.8 Heparin Competition

To assess the stability of micelleplexes, SYBR Gold assays were conducted in the presence of competing heparin.[184] Micelleplexes were prepared at a weight-to-weight (w/w) ratio of 8. Subsequently, 60 µL of the micelleplex suspension was pipetted into black FluoroNunc 96-well plates (Fisher Scientific, Germany). Next, 10 µL of heparin solutions prepared beforehand at various mass ratios of heparin to mRNA (w/w ratios of 0, 0.5, 1, 2, 4, 6, 8, 10, and 20) were added to each well. After incubating for 30 minutes at room temperature, 30 µL of a 4x SYBR Gold solution was added to each well, and the plate was further incubated for 10 minutes in the dark to allow binding. Fluorescence intensity was measured using a fluorescence plate reader (TECAN, Switzerland) with excitation at 485/20 nm and emission at 535/20 nm. The percentage of free mRNA was calculated by comparing the fluorescence intensity of each sample to that of free mRNA performed as described in section 4.3.7. All measurements were performed in triplicate, and the results are presented as mean values (n = 3).

4.3.9 CCK-8 Cytotoxicity Test

The cytotoxicity of micelleplexes was assessed using a CCK-8 assay in A549, H1299, and Hop-62 cell lines. Specifically, 10,000 cells per well were seeded 24 h prior in a transparent 96-well plate (Fisher Scientific, Hampton, NH, USA). Micelleplexes were freshly prepared at w/w 15, w/w 8, w/w4 at pH 7.4, and w/w 4 at pH 5.4. After removing the old medium, 100 µL of micelleplex containing medium was added to each well and incubated for 24 h at 37°C and 5% CO_2. Subsequently, the medium was aspirated, and fresh medium containing CCK-

8 solution (10 µL CCK-8 in 100 µL RPMI-1640 media) was added to each well. After incubating for 3 h, a water-soluble orange formazan product formed in the medium, and absorbance was measured at 450 nm using a Tecan plate reader. The experiment was conducted in triplicate, and the results are presented as mean values (n=3), normalized to the percentage of viable cells relative to untreated cells (100% viability).

4.3.10 Endosomal Escape Test by Confocal Laser Scanning Microscopy

To visualize the endosomal entrapment behavior of micelleplexes, A549 cells were imaged using confocal laser scanning microscopy (CLSM, Leica SP8 inverted, software: LAS X, Leica Microsystems GmbH, Germany) after transfection with fluorescent mRNA. Specifically, 10,000 A549 cells were seeded in ibiTreat µ-Slide 8 well plates (ibidi, Germany) and transfected with C14-PEI micelleplexes containing Cy5-mRNA at weight-to-weight ratios (w/w) of 4 and 8. Polyethyleneimine (PEI) and free Cy5-mRNA served as controls. Following incubation at 37°C with 5% CO_2 for 4, 8, or 24 h, cells were stained with LysoTracker Green DND-26 in pre-warmed cell culture medium for 1 h in the cell incubator. After removing the medium, cells were fixed with 4% paraformaldehyde (PFA) for 15 minutes in the dark and washed. DAPI was added to appropriate wells at a final concentration of 1 µg mL^{-1} in PBS and incubated for 20 minutes at room temperature in the dark. Subsequently, all cells were washed and maintained in PBS at 4°C for subsequent analysis using CLSM. Excitation was achieved using a diode laser at 405 nm, an argon laser at 488 nm, and a helium-neon laser at 650 nm. Emission was recorded in the blue channel (420 nm - 480 nm) for DAPI, the green channel (500 nm – 550 nm) for LysoTracker Green, and the red channel (650 nm - 720 nm) for Cy5-mRNA fluorescence.

4.3.11 eGFP Expression Test by Flow Cytometry

To evaluate the translational efficiency of mRNA delivered by C14-PEI, we quantified the expression of the enhanced green fluorescent protein (eGFP) reporter gene using flow cytometry. H1299, A549, and Hop-62 cell lines were seeded at a density of 30,000 cells per well in 24-well plates containing 500 µL of growth medium. Following incubation in a cell culture incubator (37°C, 5% CO_2) for 24 h, the cells were transfected with C14-PEI micelleplexes encapsulating eGFP-mRNA at w/w8 and w/w 4 prepared at pH 7.4, and at a w/w ratio of 4 prepared at pH 5.4. PEI served as a control treatment. After 24 h of transfection, cells were washed with PBS and detached using 0.05% trypsin-EDTA. The detached cells were collected in 1.5 mL Eppendorf tubes and centrifuged at 300 g for 5 minutes. The supernatant was aspirated, and cells were washed with PBS, followed by another centrifugation step. The cell pellet was resuspended in fresh PBS, and fluorescence intensity was measured using Attune NxT flow cytometry (Thermo Fisher, Germany) with excitation at 488 nm and emission at 510 nm. Results are presented as mean ± standard deviation (SD, n=2 or 3).

4.3.12 Agarose Gel Electrophoresis

Agarose gel electrophoresis was employed to confirm the co-encapsulation of Cas9 mRNA and sgRNA, as well as to perform the T7EI assay. A 1-1.5% agarose gel containing SYBR Safe (1:100,000 dilution) was prepared in TBE buffer. Subsequently, micelleplexes and free RNA samples, along with products from the T7EI assay, were mixed with 6x DNA loading dye and loaded onto the gel. Electrophoresis was conducted at 150 V for 40 minutes. The gel was visualized using the ChemiDoc imaging system (Bio-Rad, US).

4.3.13 Editing Efficiency Test by T7EI Assay

The T7EI assay was conducted according to the manufacturer's protocol using the GeneArt™ Genomic Cleavage Detection Kit. A549 cells were initially seeded in 6-well plates at a density of 100,000 cells per well in 1.5 mL of

medium 24 h prior to the experiment. Following a media change, cells were transfected with C14-PEI micelleplexes containing Cas9 mRNA and sgRNA at w/w 8, w/w 4 prepared at pH 7.4, and w/w 4 prepared at pH 5.4. Lipofectamine 2000 was included as a positive control. Transfected cells were then incubated at 37°C with 5% CO_2 for 48 h. Subsequently, cells were washed with PBS, harvested using 0.05% trypsin-EDTA, and collected by centrifugation into 1.5 mL Eppendorf tubes. The cell pellets were lysed using lysis buffer, and the resulting lysates were utilized for polymerase chain reaction (PCR) amplification of sequences containing *KRAS* alleles. Following PCR amplification, the PCR products underwent re-annealing and treatment with the detection enzyme as per the kit's instructions. Positive control samples provided in the kit, both with and without enzymes, were included for validation. Agarose gel electrophoresis was performed to visualize the cleavage products, and images were captured using the ChemiDoc imaging system as section 4.3.12 described. Data analysis was conducted using Image Lab Software.

4.3.14 Droplet Digital PCR

A549 cells were transfected in a 6-well plate using C14-PEI at w/w 4 and w/w 8 with Cas9 mRNA and sgRNA for 48 h, with lipofectamine 2000 used as a positive control. Genomic DNA was extracted from both untreated and treated A549 cells using the DNeasy Blood & Tissue Kit (Qiagen), and the DNA concentration was quantified using a Nanodrop spectrophotometer. Primers and probes were custom-designed and obtained from Bio-Rad. The reaction mixtures for droplet digital PCR (ddPCR) contained 2× ddPCR Supermix for Probes (no dUTP), with final concentrations of 900 nM for each primer and 250 nM for each FAM- or HEX-labeled probe. A total of 100 ng of template DNA was added to achieve a final reaction volume of 20 µL. Standard Bio-Rad reagents and consumables, including cartridges, gaskets, droplet generation oil, and droplet reader oil, were used. After droplet generation, droplets were carefully transferred to a 96-well PCR plate and sealed using the PX1 PCR Plate Sealer (Bio-Rad). The PCR conditions were as follows: initial denaturation at 95°C for 10 minutes, followed by 40 cycles of denaturation at 94°C for 30 seconds, annealing/extension at 55°C for 3 minutes, and a final extension step

at 98°C for 10 minutes, followed by a hold at 4°C. The ramp rate was set at 2°C/s. Droplets were read using the QX200 Droplet Reader (Bio-Rad), and each reaction included a no-template control (NTC). Data analysis was performed using QuantaSoft Software.[185]

4.3.15 Sanger Sequencing

Genomic DNA was extracted from A549 cells 48 h post-transfection with C14-PEI w/w 8 using the DNeasy Blood & Tissue Kit. To visualize the gene sequence after gene editing, PCR was performed using a pair of primers designed to target regions before and after the cleavage site, yielding a PCR product of approximately 500 base pairs. The Phusion Hot Start II High-Fidelity PCR Mastermix was utilized for PCR amplification. The cycling conditions were as follows: initial denaturation at 98°C for 30 seconds, followed by 35 cycles of denaturation at 98°C for 10 seconds, annealing at 61.5°C for 30 seconds, extension at 72°C for 30 seconds, and a final extension at 72°C for 10 minutes. PCR products were verified by electrophoresis on 1% agarose gels. Following gel verification, PCR products were purified using the ExoSAP-IT™ Express PCR Product Cleanup Reagent. The purified PCR products were subsequently used for Sanger sequencing to determine the sequence changes resulting from the gene editing process. The results were analyzed by the ICE CRISPR analysis tool.[186]

4.3.16 Western Blot

To assess the ability of C14-PEI micelleplexes to inhibit downstream signals in the KRAS pathway, A549 cells were seeded in 6-well plates and allowed to grow for 24 h to reach a density of $1x10^5$ cells per well. The cells were then treated with C14-PEI micelleplexes and incubated at 37°C with 5% CO_2 in a humidified incubator for 48 h. Following treatment, cells were washed with ice-cold PBS and lysed in lysis buffer consisting of 800 µL RIPA buffer, 100 µL Phosphatase inhibitor, and 100 µL Protease inhibitor. The protein content in the lysates was quantified using the Pierce™ BCA Protein Assay kit (Thermo Fisher), and equal amounts of protein were loaded for SDS-PAGE (Novex™

WedgeWell™ 8-16% Tris-Glycin gel). Separated proteins were then transferred onto nitrocellulose membranes, which were subsequently blocked with 5% skim milk in TBST (Tris-buffered saline with 1% Tween 20) for 1 h at room temperature. Membranes were then incubated overnight at 4°C with primary antibodies targeting specific proteins of interest in the KRAS pathway. After primary antibody incubation, membranes were washed three times with 1% TBST and then incubated with horseradish peroxidase (HRP)-conjugated secondary antibodies at room temperature for 1 h. Protein bands were visualized using chemiluminescence substrates and imaged immediately using the ChemiDoc imaging system (BioRad, US). Between antibody stainings, membranes were treated with stripping buffer for 30 minutes to remove bound antibodies, followed by washing with TBST and re-blocking with 5% skim milk in TBST solution. This systematic approach allowed for the quantification of protein expression levels involved in the KRAS pathway inhibition following treatment with C14-PEI micelleplexes, providing insights into their therapeutic potential.[187]

4.3.17 Wound Healing Assay

The µ-Dish with culture-insert 2 well (ibidi, Germany) was utilized for conducting a wound healing assay.[188] Initially, 10,000 A549 cells suspended in 70 µL of RPMI-1640 media were added to each well of the Culture-Insert 2 Well and allowed to incubate at 37°C with 5% CO_2 for a minimum of 24 h to achieve a confluent cell layer. Following incubation, the insert was carefully removed using sterile tweezers, and the cell layer was washed twice with PBS to eliminate any cell debris and non-adherent cells. Subsequently, the µ-Dish was filled with 2 mL of fresh complete medium containing either C14-PEI micelleplexes or Lipofectamine 2000, as per experimental requirements. The cells were maintained in the incubator at 37°C with 5% CO_2 throughout the experiment, and images were captured at 0, 4, 8, 24, and 48 h using an EVOS microscopy (Thermo Fisher, Germany). The area of the wound gap was quantified and analyzed using ImageJ software, providing insights into the migration and healing dynamics of the A549 cell monolayer in response to the treatments administered.

4.3.18 Cell Apoptosis

Annexin V and propidium iodide (PI) staining allowed for the quantification of apoptotic and necrotic cells, providing insights into the cellular response to C14-PEI micelleplex transfection.[189] A total of $1x10^5$ cells per well were initially seeded onto a 6-well plate in RPMI-1640 complete medium and transfected with C14-PEI micelleplexes. Following a 48-h incubation at 37°C with 5% CO_2, the cells were washed twice with cold PBS and resuspended in Annexin V Binding Buffer at a concentration of $1x10^6$ cells/ml. Subsequently, 100 µL of the cell suspension was mixed with 10 µL of Annexin V-AF488 (Thermo Fisher) and 1 µL of PI (BD Biosciences), and the mixture was incubated for 15 minutes at room temperature in the dark. After incubation, 400 µL of Annexin V Binding buffer was added to each tube to halt the reaction. Fluorescence signals from Annexin V-AF488 and PI staining were measured using the Attune NxT flow cytometry (Thermo Fisher, Germany), and the data were analyzed using FlowJo software.

4.3.19 Statistics

Unless otherwise specified, all results are presented as the mean value ± standard deviation (SD) based on triplicate experiments (n=3). Statistical analyses were performed using GraphPad Prism software (GraphPad Software, USA).

4.4 Results

4.4.1 C14-PEI Synthesis and Characterization

It has been reported that modifying polymeric micelleplexes with hydrophobic groups can enhance their affinity for cell membranes and improve the delivery of nucleic acids.[180,181] Specifically, substituting free amines on cationic polymers with alkyl tails yields amphiphilic polymers, which promote particle formation through hydrophobic aggregation. Due to the hydrophobic nature of

cell lipid bilayers, hydrophobic micelleplexes exhibit more favorable interactions with cell membranes.[190] However, identifying suitable cationic polymeric carriers for mRNA delivery remains challenging due to mRNA's large molecular size, secondary structure, and intrinsic single-strand instability.[67] To address this challenge, we conducted rapid screenings of eGFP mRNA expression in immortalized cell lines using a series of polymeric delivery systems with various modifications. Among these materials, C14-PEI exhibited superior characteristics and delivery efficiency.

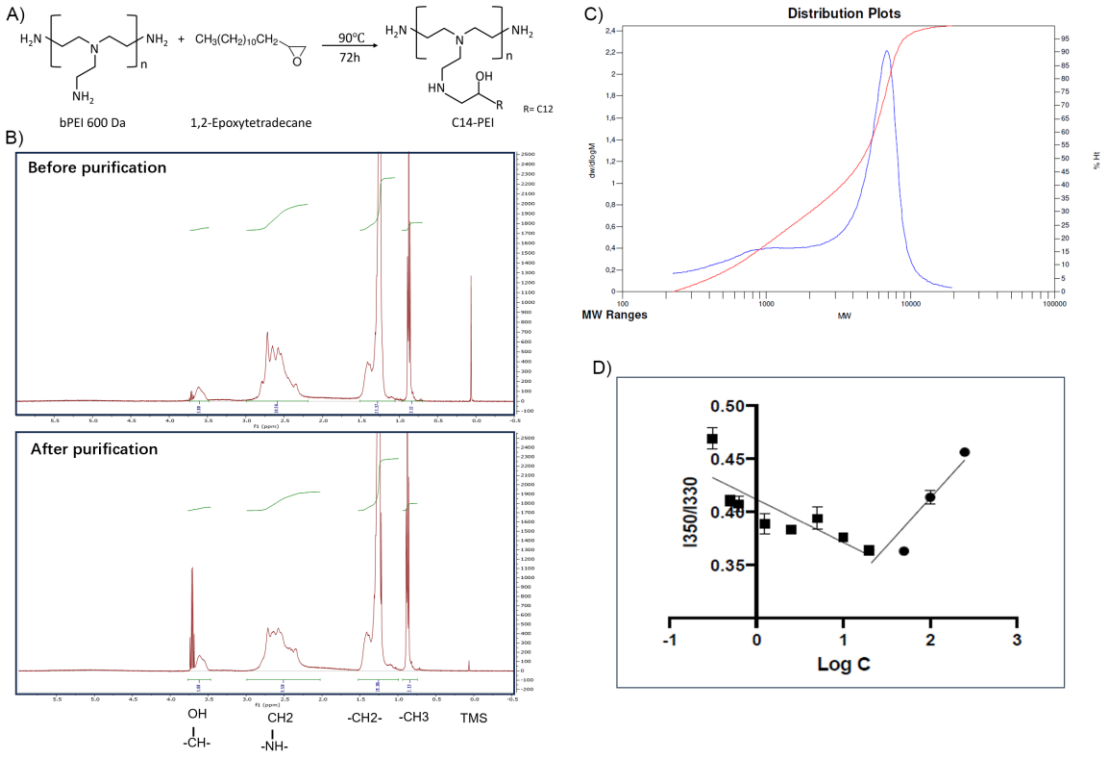

Figure 1. Characterization of C14-PEI. A) The schematic of C14-PEI synthesis; **B)** ^{1}H NMR spectra of C14-PEI before and after dialysis; **C)** The molecular weight of Mn 1697 Da of the final product (blue) was confirmed by GPC; **D)** Pyrene fluorescence intensity at 350/330 as a function of polymer concentration (n=3). CMC is noted as the point of inflection where fluorescence intensity begins to increase.

C14-PEI was synthesized by reacting 1,2-epoxytetradecane with branched PEI via a ring-opening reaction (Figure 1A), followed by purification through dialysis with a 1,000 Dalton cut-off membrane. Our initial experiments involved varying the concentration of 1,2-epoxytetradecane in the reaction system, starting at a molar ratio of 10% epoxy groups in 1,2-epoxytetradecane to amine groups in PEI (Figure SA-SB). Ultimately, we determined that 33% C14-PEI,

corresponding to a 1:1 ratio of epoxy groups to primary amines, demonstrated the highest transfection efficiency. Therefore, 33% C14-PEI was selected for subsequent experiments unless otherwise specified.

Nuclear magnetic resonance spectroscopy (NMR) was employed to evaluate the modification of C14-PEI before and after purification. The ^{1}H NMR spectrum of C14-PEI exhibited characteristic signals corresponding to both the PEI backbone and the pendant carbon strand moieties (Figure 1B). The PEI backbone displayed major peaks at δ 2.2-3.8 parts per million (ppm). Additionally, characteristic proton peaks influenced by the hydrophobic moieties were observed at δ 3.5-3.75 ppm. Strong signals at 0.75 and 1.25 ppm were attributed to the methyl and alkyl groups on the carbon strands, respectively. Importantly, the ^{1}H NMR analysis revealed the complete disappearance of the epoxy group, confirming the absence of free 1,2-epoxytetradecane starting material. In comparison to unpurified C14-PEI, the purified sample exhibited similar chemical shifts for the main functional groups but with notable improvements: reduced noise, sharper peaks, better resolution, and decreased overlap. These characteristics collectively indicated a purer sample with successful removal of impurities during the purification process.

The molecular weight of the final product, determined by gel permeation chromatography (GPC), was Mn 1700 Da (Figure 1C), consistent with theoretical calculations (Mn 1600–1800 Da) based on the modification of primary amines at a 1:1 molar ratio. The polydispersity index (PDI) of the final product was 2.6, indicating a more uniform polymer distribution compared to the unpurified polymer (PDI: 3.16, Figure SE), which is advantageous for subsequent drug delivery applications.

Due to its amphiphilic nature, C14-PEI forms micellar structures in aqueous media. The critical micelle concentration (CMC) was determined using pyrene as a probe molecule, based on its linear relationship with polymer concentration.[182] The CMC of C14-PEI was measured at 20.86 ± 0.15 mg/L

(Figure 1D), which was lower than small-molecule surfactants, supporting the stability of micelles and potential protection from opsonization *in vivo.*[184]

4.4.2 Preparation and Characterization of Micelleplexes

Various formulations of C14-modified PEI were synthesized by modifying different percentages (10%, 20%, 33%, and 100%) of the amine groups on PEI. Micelleplexes were subsequently prepared with eGFP mRNA at different mass ratios as described in the methods section 4.3.5. The efficiency of eGFP expression was evaluated using flow cytometry to quickly screen the modifications. Based on the results (Figure SC-SD), 33% C14-PEI at a weight-to-weight ratio (w/w) of 8 at pH 7.4 was chosen for further testing. Additionally, formulations at w/w 4 prepared at pH 7.4 and w/w 4 prepared at pH 5.4 were selected for comparison. To characterize the micelleplexes, dynamic light scattering (DLS) and laser Doppler anemometry (LDA) were employed to measure their size and zeta (ζ) potential. Specifically, micelleplexes at w/w 8 exhibited a hydrodynamic diameter of approximately 300 nm (PDI: 0.16) with a zeta potential of 40 mV (Figure 2A and 2B). However, at a lower mass ratio of w/w 4, the particle size increased to over 1000 nm (PDI: 0.27), indicative of aggregation. When the pH was reduced to 5.4, the size of the w/w 4 formulation decreased (size: 200 nm, PDI: 0.14), likely due to enhanced electrostatic interactions. All three groups exhibited a zeta potential of approximately 40 mV. This moderately positive zeta potential suggests adequate electrostatic repulsion, crucial for preventing particle aggregation and maintaining stability in suspension.[191] Given that most cellular membranes are negatively charged, positively charged nanoparticles may facilitate enhanced cellular uptake through strong interactions. However, cationic particles are generally associated with increased toxicity due to potential cell membrane disruption.[192] Moreover, an excessively positive zeta potential could lead to over-stabilization, potentially affecting drug release profiles.[191] Therefore, careful consideration of particle stability, toxicity, and cellular uptake is essential for subsequent experiments.

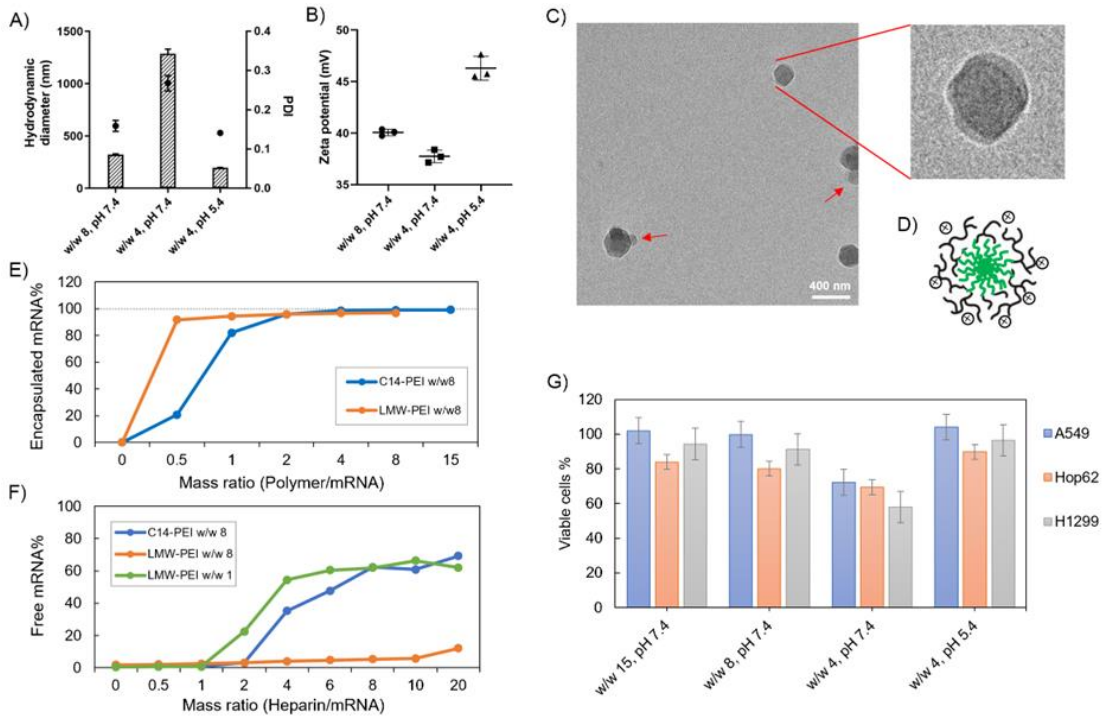

Figure 2. Characterization of C14-PEI formulation. A) the hydrodynamic diameter (bars) and polydispersity index (PDI, dots) of micelleplexes (n=3); **B)** the zeta potential of micelleplexes (n=3); **C)** Cryo-EM image of C14-PEI w/w 8; **D)** schematic drawing of C14-PEI w/w 8; **E)** SYBR Gold assay to assess the encapsulation and **F)** heparin competition assay to determine release (n=3); **G)** the percentage of viable cells after 24h transfection in A549 cells (n=3).

The C14-PEI delivery system tends to form micelleplexes, where the hydrophobic chains constitute the core and the hydrophilic portions form the shell. Cryo-electron microscopy (Cryo-EM) imaging confirmed the presence of a core-shell spherical structure in these micelleplexes. Figure 2C displays the particle sizes of C14-PEI micelles at w/w 8, pH 7.4, which align with the DLS results, showing sizes around 300 nm. In the images, a distinct dark core is surrounded by a blurred corona structure. Additionally, in Figure 2C, bleb-like structures are observed in the nanostructures. Similar bleb structures have been reported in lipid nanoparticles (LNPs) by Cheng and colleagues.[193] They noted that alterations in pH and buffer concentration could induce the formation of these structures, thereby enhancing *in vitro* transfection efficiency. This enhancement is attributed to improved mRNA stability when sequestered within bleb structures in LNPs.

4.4.3 The Assessment of The Formulation Properties

Encapsulation

As previously noted, mRNA is inherently unstable due to its single-stranded structure, making it susceptible to degradation by nucleases.[57] Protecting mRNA from nuclease digestion is crucial, and the ability of polymers to encapsulate mRNA is a key factor in assessing their suitability as mRNA carriers. SYBR Gold, a fluorescent intercalating dye that stains free nucleic acids and emits fluorescence upon excitation at 495 nm, is commonly used for this purpose.[194] Cationic polymers interact electrostatically with the negatively charged phosphate groups present in mRNA molecules, facilitating the encapsulation of mRNA within micelleplexes through charge complexation. This interaction decreases accessibility for intercalation and thus reduces the fluorescence intensity of SYBR Gold, allowing for the quantification of free mRNA in the micelleplex suspensions by measuring fluorescence intensity.

Figure 2E illustrates the use of low molecular weight PEI (LMW-PEI) as a control, where fluorescence measured with free mRNA was established as 100%. The percentage of free mRNA decreased with increasing the formulations' mass ratio, indicating polymer-mediated encapsulation of mRNA into polyelectrolyte complexes. Below a mass ratio of w/w 2, C14-PEI demonstrated less efficient mRNA condensation compared to LMW-PEI. Specifically, C14-PEI exhibited only 20% encapsulation efficiency at w/w 1, whereas LMW-PEI efficiently encapsulated mRNA even at very low mass ratios. However, at a mass ratio of w/w 2, the encapsulation efficiency of C14-PEI began to approach that of LMW-PEI, showing approximately 4% free mRNA. As the mass ratio increased further, C14-PEI demonstrated superior condensation capability compared to LMW-PEI, achieving mRNA encapsulation efficiencies of around 98% and nearly 100% at w/w 4 and w/w 8, respectively. This behavior can be attributed to the occupation of primary amine groups by C14 chains, which reduces positive charges. Initially, at low mass ratios, C14-PEI exhibited lower mRNA encapsulation efficiency compared to LMW-PEI. However, with increasing polymer concentration, as observed

elsewhere,[195] amphiphilic materials condense mRNA through electrostatic and hydrophobic interactions, demonstrating high nucleic acid-binding affinity.

mRNA release

The stability of micelleplexes can be disrupted by the presence of competing anions.[196] To assess the stability of C14-PEI/mRNA complexes and gain deeper insights into micelleplex behavior, we investigated the integrity of micelleplexes in the presence of a competing polyanion (heparin) using SYBR Gold staining. LMW-PEI was included as a control at polymer-to-mRNA mass ratios of w/w 1 and w/w 8. In Figure 2F, at the w/w 8 polymer/mRNA mass ratio, mRNA remained tightly bound to LMW-PEI even with a 20-fold excess of heparin relative to mRNA (heparin/mRNA w/w 20, approximately 2 units of heparin). This strong binding is attributed to the excessive positive charges in PEI, which result in a robust interaction with mRNA, hampering its release. While stable complexes in the presence of competing anions are desirable, overly strong binding can hinder mRNA release from micelleplexes into the cytoplasm.[197] Reducing the amount of LMW-PEI improved the situation; at a w/w 1 polymer/mRNA mass ratio, the LMW-PEI/mRNA complexes remained stable until the heparin to mRNA ratio reached 1 unit (heparin/mRNA w/w 1).

In contrast, C14-PEI w/w 8 exhibited a release profile similar to LMW-PEI at w/w 1. mRNA began to release from C14-PEI at a heparin to mRNA mass ratio of w/w 2. Notably, the micelleplexes demonstrated stability in the presence of up to a 2-fold excess of heparin/mRNA and released approximately 70% of mRNA at a 20-fold excess of heparin (Figure 2F). Optimizing polymer concentrations advantageously contributes to micelleplex stability after introduction into serum-containing cell culture media or administration *in vivo*, and facilitates mRNA release from micelleplexes into the cytoplasm.

Cytotoxicity

A significant drawback of cationic delivery systems is their potential toxicity arising from high positive charge densities, which can disrupt cellular

membrane integrity and lead to pore formation.[198] To assess cytotoxicity, the cell counting kit-8 (CCK-8) assay was employed, which measures the intracellular reduction of tetrazolium salt (WST-8) to produce an orange water-soluble formazan dye through bioreduction in the presence of an electron carrier, 1-Methoxy PMS. The absorbance of this dye correlates linearly with the number of viable cells, providing a direct measure of toxicity. Cytotoxicity testing was conducted using different cell lines, A549, H1299, and Hop62. C14-PEI/mRNA complexes at various mass ratios (w/w 15, w/w 8, w/w 4 prepared at pH 7.4, and w/w 4 prepared at pH 5.4) were evaluated. After 24 h of transfection, all groups exhibited low toxicity across the three cell lines, except for the w/w 4 group prepared at pH 7.4 (Figure 2G). Specifically, cell viability with C14-PEI at w/w 15 and w/w 8 prepared at pH 7.4 exceeded 80%. In contrast, the w/w 4 group prepared at pH 7.4 displayed higher toxicity, resulting in less than 60% cell viability. Interestingly, reducing the pH to 5.4 mitigated toxicity in the w/w 4 group, achieving comparable cell viability (around 80%) to those observed in the w/w 15 and w/w 8 groups prepared at pH 7.4. This observation is consistent with the tendency of particles to aggregate at w/w 4 at pH 7.4, as indicated by DLS results.

4.4.4 Delivery of mRNA

Endosomal escape test

The endocytic pathway is the major uptake mechanism for nanocomplexes.[199] Micelleplexes become entrapped in endosomes and are subsequently degraded by specific enzymes in lysosomes. Therefore, facilitating endosomal escape to ensure the cytosolic delivery of therapeutics is a critical step in achieving effective macromolecule-based therapy.[94] To accurately depict the endosomal release of micelleplexes internalized by cells, A549 cells were transfected with Cy-5 mRNA and stained with LysoTracker Green DND-26, a fluorescent probe that accumulates in acidic vesicles, along with DAPI staining before analysis by confocal laser scanning microscopy (CLSM). Figure 3A illustrates different formulation treatments and their effects on cellular uptake and endosomal release of Cy-5 labeled mRNA. Blue areas depict cell nuclei

stained with DAPI, green staining indicates lysosomes, red staining represents incorporated Cy-5 labeled mRNA, and yellow dots reflect mRNA co-localized within lysosomes.

As shown in Figure 3A, no red signal is detected in samples with free mRNA or PEI formulation, indicating that successful uptake cannot occur without an appropriate delivery system. However, C14-PEI transfection at w/w 4 and w/w 8 results in a punctate distribution of Cy-5 labeled mRNA, suggesting endosomal entrapment of the delivered cargo. Despite the persistence of yellow dots after 24 h, indicating partial entrapment in endosomes, a significant proportion of mRNA was able to escape and disperse into the cytoplasm. Specifically, at 4 h post-transfection, only a few red and yellow dots are observed in both the w/w 4 and w/w 8 groups, reflecting early cellular internalization. By 8 h, maximum uptake is observed in the C14-PEI w/w 4 samples, with the signal decreasing by 24 h. In contrast, uptake of C14-PEI at w/w 8 continues to increase, reaching a maximum at 24 h. Interestingly, Figure 3A shows that the red dots, representing Cy-5 labeled mRNA, were more enriched and appeared larger in the w/w 4 samples compared to the w/w 8 samples. This suggests that C14-PEI micelleplexes were more prone to aggregation at the w/w 4 ratio, which aligns with the larger sizes observed in the DLS results. Consequently, these aggregated micelleplexes exhibited faster sedimentation and higher sedimentation efficiency in the cell media. This resulted in faster internalization of C14-PEI at w/w 4 compared to C14-PEI at w/w 8.

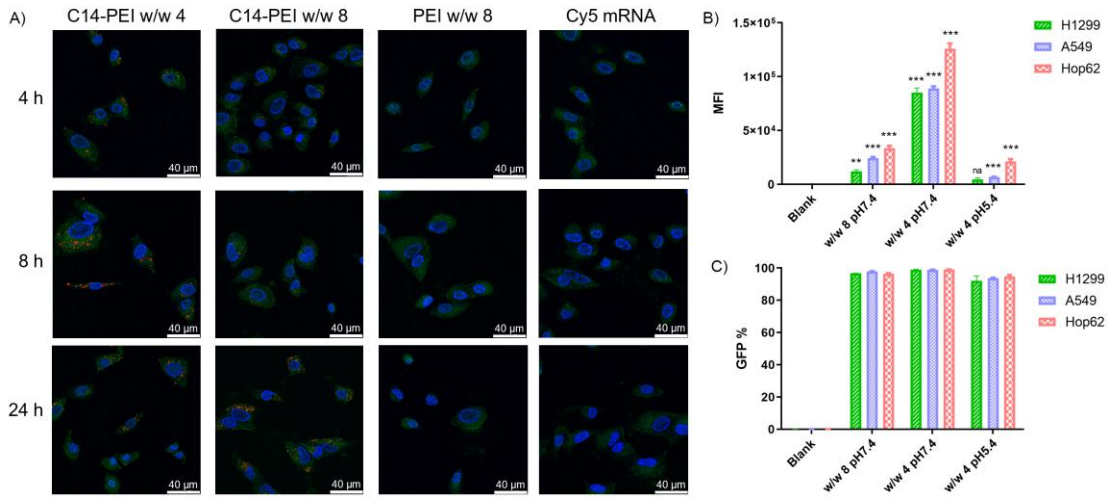

Figure 3. Delivery of eGFP mRNA. A) Endosomal entrapment of C14-PEI formulation via CLSM; **B)** Median eGFP fluorescence intensity after C14-PEI transfection 24h (n=3, *P ≤0.033, **P ≤0.002, ***P ≤0.001); **C)** the percentage of eGFP positive cells.

eGFP mRNA expression

To investigate the mRNA expression efficacy of the C14-PEI formulation, eGFP mRNA was transfected into H1299, A549, and Hop62 cell lines using formulations of w/w 8, w/w 4 prepared at pH 7.4, and w/w 4 prepared at pH 5.4. Following transfection, median fluorescence intensity (MFI) and the percentage of eGFP-positive cells were measured using flow cytometry (FACS). As shown in Figure 3C, all groups exhibited eGFP expression, with over 90% of cells in all three cell lines being eGFP-positive. The w/w 4 formulation prepared at pH 7.4 resulted in an MFI that was over 1000-fold higher than the blank control (Figure 3B). The lowest MFI was observed with the w/w 4 formulation prepared at pH 5.4, which showed a 30-40 fold increase compared to the blank. The w/w 8 formulation achieved an MFI increase of beyond 100-fold compared to the blank. The significantly high eGFP expression observed in the C14-PEI w/w 4 group at pH 7.4 can be attributed to rapid and efficient cellular internalization.

4.4.5 Co-delivery of Cas9 mRNA and sgRNA

Co-encapsulation

Given the structural and length differences between sgRNA and Cas9 mRNA, confirming their co-encapsulation is essential. Electrophoretic mobility shift assays (EMSA) were employed for this evaluation, leveraging the ability of electrophoresis to separate nucleic acid molecules of different sizes by electrophoretic mobility.[200] In these assays, free RNA migrates through the gel due to its negative charge, whereas encapsulated RNA remains in the loading slots, as the micelleplexes are larger than the gel's mesh size.[201] As shown in Figure 4A, lanes 2 and 3 display the free Cas9 mRNA and free sgRNA bands, located at 4500 nt and 100 nt, respectively. Lane 4 clearly shows the separated bands of the mixture of free Cas9 mRNA and sgRNA. In contrast, lanes 5 and 6, containing samples of C14-PEI w/w 4 and w/w 8, show no bands on the gel.

Instead, a bright signal is visible within the slots, indicating that both Cas9 mRNA and sgRNA are encapsulated within the micelleplexes.

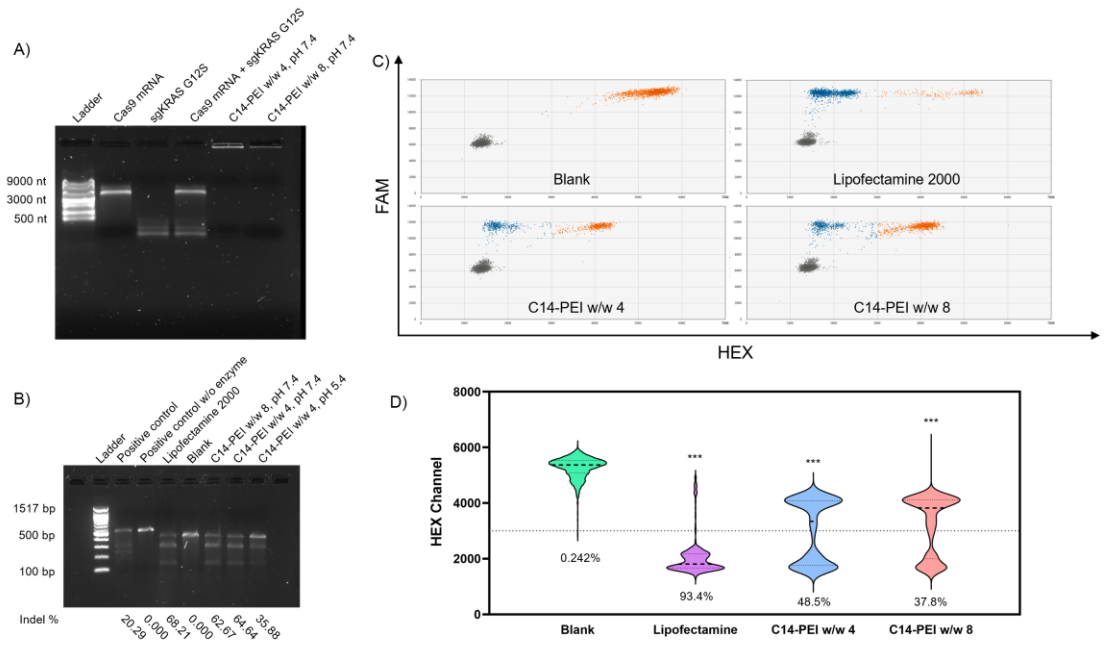

Figure 4. Co-delivery of Cas9 mRNA and sgRNA. A) Agarose gel shows the co-encapsulation of Cas9 mRNA and sgRNA in C14-PEI formulation; **B)** T7EI cleavage tests in agarose gel, gene editing efficiency is indicated below the image; **C)** Droplet distribution of ddPCR, X-axis is HEX channel, Y-axis is FAM channel, Gray dots represent the FAM-negative/HEX-negative group, orange dots represent the FAM-positive/HEX-positive group, blue dots represent the FAM-positive/HEX-negative group; **D)** Violin plots of the HEX channel (excludes FAM negative droplets) of ddPCR (***P≤0.001), intensity at 3000 is set as threshold, and editing efficiency is indicated below the plots.

T7EI assay

To further verify the ability of the C14-PEI formulation to co-deliver Cas9 mRNA and sgRNA and facilitate gene editing in cells, we transfected A549 cells, harboring a *KRAS* G12S mutation,[202] with Cas9 mRNA and sgRNA targeting the *KRAS* G12S allele using C14-PEI micelleplexes. Numerous methods for verifying CRISPR gene editing have been reported in the literature.[185,203-205] Due to the sensitivity limitations of experimental and analytical methods, a single detection method cannot accurately reflect gene knockout efficiency. We performed three different assays to evaluate the deletion of *KRAS* G12S alleles in A549 cells. Specifically, genomic DNA was isolated from transfected cells 48 h post-transfection. The T7 Endonuclease I (T7EI) assay, droplet digital PCR

(ddPCR), and Sanger sequencing were then conducted to measure gene editing efficiency.

Non-homologous end joining (NHEJ) is the primary mechanism for knockout mediated by CRISPR-Cas9.[206] During NHEJ, insertions and/or deletions (Indels) are commonly induced in the DNA strand. T7 Endonuclease I, a structure-selective enzyme, specifically recognizes indel sites on the DNA sequence and cleaves them into two fragments.[205] The digestion products can then be visualized and analyzed by agarose gel electrophoresis.

As shown in Figure 4B, the untreated sample exhibited only one band corresponding to the target sequence, while all treated samples displayed both the mother band and two cleaved bands. From the intensity analysis, the Lipofectamine 2000 group resulted in 68.21% indels. Similarly, the w/w 8 and w/w 4 formulations prepared at pH 7.4 mediated an average of 62.67% and 64.64% indels, respectively, demonstrating comparable gene editing efficiency to the Lipofectamine 2000 group. However, the cells treated with the w/w 4 formulation prepared at pH 5.4 exhibited only 35.88% indel formation, consistent with the eGFP expression results.

ddPCR analysis

To further confirm the gene editing, the number of gene copies was measured using droplet digital PCR (ddPCR) to quantify NHEJ-mediated events in the samples. In this assay, two specific probes within one amplicon were designed.[185,204] The first probe, a reference probe (FAM), is located away from the mutagenesis site and counts all genomic copies of the target. The second probe, an NHEJ probe (HEX), is located at the site where nucleases cut or nick genomic DNA and has a wild-type (WT) sequence. If nucleases induce NHEJ, the NHEJ probe loses its binding site, resulting in the loss of the HEX signal and leaving only the FAM signal from the reference probe. As shown in Figure 4C, the orange group indicates FAM and HEX double-positive droplets, reflecting WT DNA copies, while the blue group shows FAM-positive but HEX-negative droplets, representing edited DNA copies. No blue dots are present in

the blank group, while the groups treated with C14-PEI w/w 4 and w/w 8 show 961 and 1430 blue dots respectively (edited gene copies), indicating efficient gene editing events. Subsequently, we quantified the percentage of single-positive events (edited gene copies) in the total events. As shown in Figure 4D, the gene editing efficiency of Lipofectamine 2000 reached 93.4%, whereas C14-PEI w/w 4 showed 48.5% edited copies and 37.8% positive droplets in the C14-PEI w/w 8 group. The data from ddPCR did not align perfectly with the T7EI assay results. This discrepancy arises because the T7EI assay is semi-quantitative, has limited sensitivity, is prone to false positives, and suffers from high background signals when sequence polymorphisms are present.[205] For a typical diploid target locus, a clone with both alleles successfully altered via genome editing will be indistinguishable from a clone with one mutated allele and one wild-type allele.

Sanger sequencing

To visualize the gene editing behavior of the C14-PEI w/w 8 micelleplexes, we performed Sanger sequencing on the PCR products and analyzed the data using the ICE CRISPR analysis tool.[186] Figure 5D demonstrates that indels occurred in the *KRAS* G12S allele edited by C14-PEI w/w 8. Sequencing confirmed that gene editing occurred after the PAM sequence, primarily resulting in insertions and deletions in the DNA backbones. Specifically, Figure 5B shows a significant signal shift (R^2=0.98) following gene editing compared with the control sequence. Among the generated mutations (Figure 5C and 5D), a 1 bp insertion was the most frequent, contributing to 13% of the indels, which aligns with previously reported findings.[202] Deletions ranging from 4 to 16 bases were found at various positions near the mutagenesis site, constituting 14% of the indels. These indels cause frameshift mutations in the gene, leading to the functional inactivation of the mutant KRAS protein. In summary, the sequencing data confirmed that *KRAS* in A549 cells was disrupted around the PAM (TGG) sequence, further validating the efficacy of our C14-PEI delivery system in achieving efficient and specific targeting of *KRAS* G12S alleles.

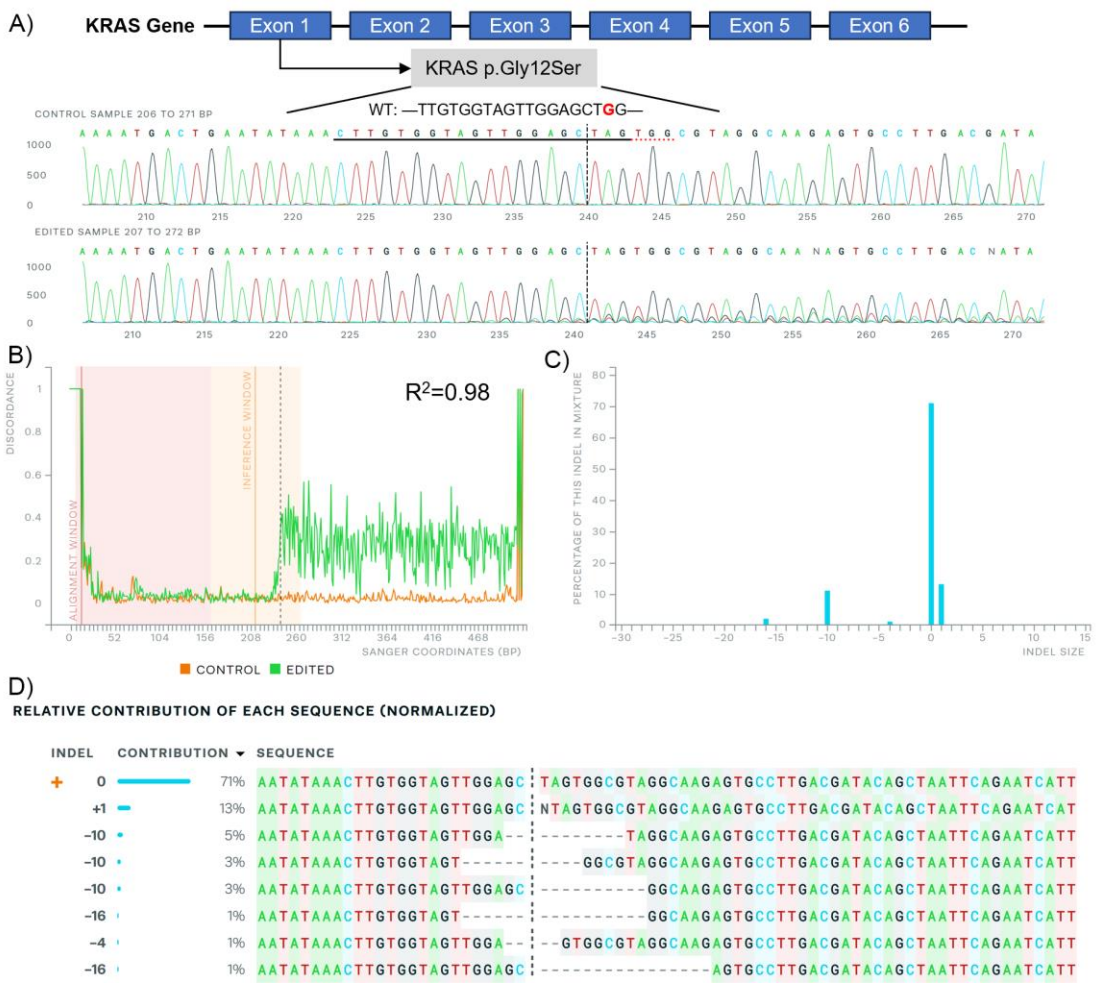

Figure 5. Sanger sequencing after C14-PEI w/w 8 treatment in A549 cells analyzed by the ICE CRISPR analysis tool. A) *KRAS* exon map (up), G12S mutation sequence (middle), and edited sequence (down) illustrate; **B）** alignment of Sanger sequencing; **C）** distribution of indel sizes; **D）** contribution of each sequence after gene editing.

4.4.6 Cell Capability Assessment

Western Blot

The *KRAS* gene mediates the translation of the KRAS protein, which relays signals from outside the cell to the nucleus. KRAS is a small GTPase that cycles between the GTP-bound active state and the GDP-bound inactive state. In its GTP-bound state, KRAS interacts with and activates downstream effector molecules, such as those in the MAPK or AKT-mTOR signaling pathways, affecting cell proliferation and survival. However, activating mutations in KRAS result in impaired GTP hydrolysis or enhanced nucleotide exchange, causing continuous downstream signal activation. This leads to a sustained proliferation

signal within the cell, which is related to the migration and invasion of cancer cells. [207,208] To assess the translation level of different signal proteins, we isolated total proteins from transfected A549 cells and conducted western blot analysis to investigate if the C14-PEI formulation can down-regulate KRAS pathways on the protein level, including the expression and activation of AKT and ERK. PEI and Lipofectamine 2000 were used as controls. As shown in Figure 6A, compared to the housekeeping gene *Histone-3*, the treatment of A549 cells with C14-PEI w/w 8 did not suppress the expression of wild-type KRAS protein. However, the level of phosphorylated-ERK protein was significantly downregulated in A549 cells edited with the micelleplexes. According to the literature,[209] phosphoproteins usually will have a minor shift in molecular weight and total antibodies can recognize them. Hence, the upper bands in the AKT blot were deemed to represent phosphorylated-AKT, fitting the expectation of downregulation in the treated groups. As predicted, total AKT and ERK proteins were not affected by the treatment. These results suggest that while the overall levels of KRAS, AKT, and ERK proteins remain unchanged, the downstream signaling pathways, particularly those involving phosphorylated forms of AKT and ERK, are downregulated in cells treated with the C14-PEI micelleplexes. This indicates the potential effectiveness of the C14-PEI delivery system in mitigating the aberrant signaling caused by mutant *KRAS*, thereby affecting cell proliferation and survival pathways involved in cancer progression.

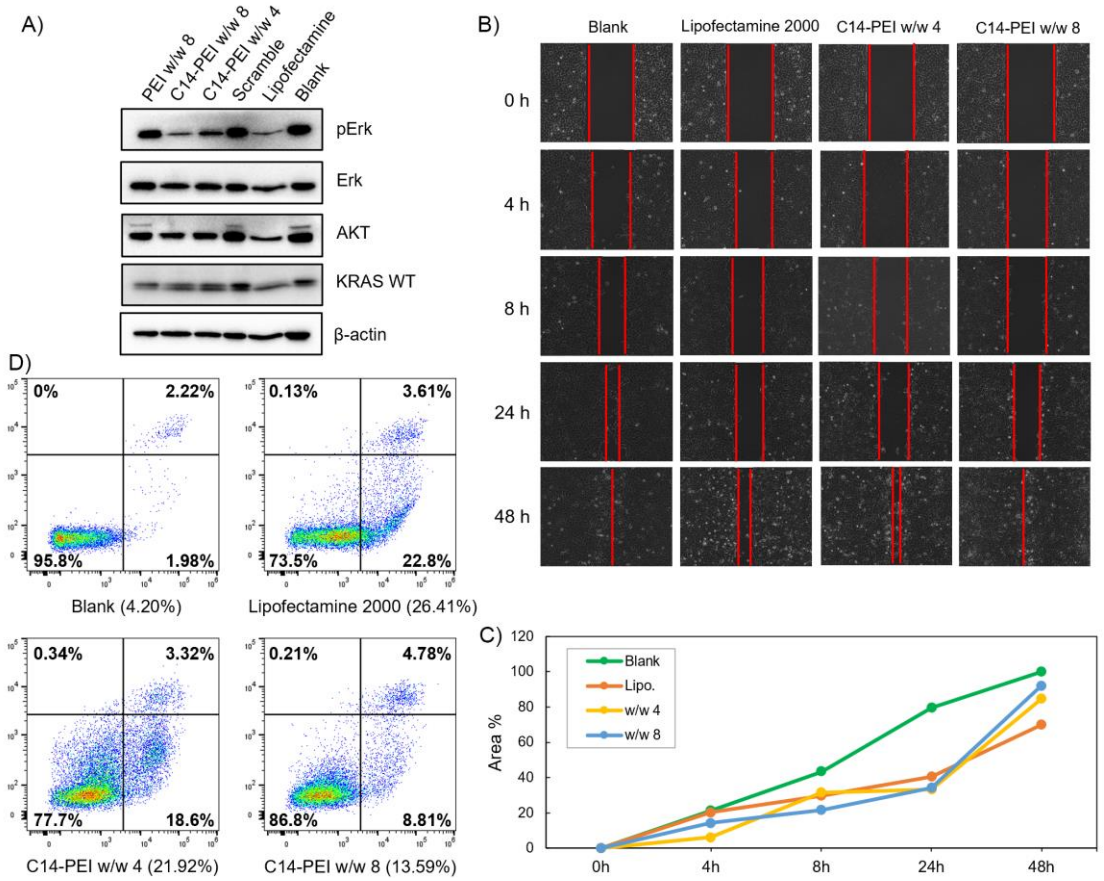

Figure 6. Cell capability assessment after the transfection of C14-PEI micelleplexes. A) Western blot after transfection 48h in A549 cells; **B)** images of A549 cells in the wound healing assay in 48h after transfection; **C)** percentage of covered area in wound healing assay; **D)** cell apoptosis after transfection 24h in A549 cells.

Cell migration

A wound healing assay was used to estimate the ability of cell migration after treatment with C14-PEI micelleplexes in A549 cells. The gap area closure was quantified by comparing images from time 0 h to 48 h using ImageJ. Generally, the treated groups showed slower cell migration compared to the blank group, and the group treated with Lipofectamine 2000 exhibited the slowest migration among all groups (Figure 6C and 6D). After 8 h, the blank group migrated and covered approximately 50% of the wound area quantified at time 0 h. Meanwhile, the C14-PEI w/w 8 group showed the lowest coverage of the wound area, occupying around 20%, while cells treated with C14-PEI w/w 4 and Lipofectamine 2000 covered nearly 30% of the wound area. After 48 h, the wound in the blank group was completely closed, and the coverage of the

wound area in the C14-PEI w/w 4 and w/w 8 groups grew to 85% and 92%, respectively. Only 70% of the wound area was covered in the Lipofectamine 2000 group at 48 h. Given that Lipofectamine 2000 is known to exhibit high cytotoxicity,[210] the slowest migration observed in this group is expected. However, since our C14-PEI formulation did not show significant cytotoxicity (Figure 2G), the results are reliable and suggest that the C14-PEI micelleplexes can effectively inhibit tumor cell migration.

Cell apoptosis

To further investigate whether C14-PEI micelleplexes inhibited A549 cell growth through the induction of apoptosis, the percentage of apoptotic cells was assessed using flow cytometry with Annexin V-AF488/propidium iodide (PI) double-staining assay following treatment with C14-PEI w/w 4 and w/w 8.[189] Lipofectamine 2000 was included as a positive control. The representative flow cytometry data are presented in Figure 6D. It was demonstrated that treatment with C14-PEI w/w 4, C14-PEI w/w 8, and Lipofectamine 2000 for 24 h significantly increased the numbers of apoptotic cells compared with the blank group. Notably, Lipofectamine 2000 exhibited the highest percentage of apoptotic cells (26.41%), followed by C14-PEI w/w 4 (21.92%) and C14-PEI w/w 8 (13.59%).

Protein translation and cell function don't always show a consistent tendency with gene editing, because of incomplete knockout efficiency and functional compensation.[211] When a gene is edited or knocked out, cells can activate alternative pathways to compensate for the loss of function. This can involve the upregulation of genes with similar functions or the activation of parallel pathways to maintain cellular homeostasis. In particular, genes involved in the cell cycle and DNA repair were identified as essential, suggesting compensatory mechanisms when these pathways are disrupted.[212] However, our results suggested that the deletion of mutant *KRAS* G12S alleles by C14-PEI micelleplexes can effectively inhibit tumor cell proliferation and migration, and promote the apoptosis of tumor cells after treatment, likely through downregulation of the AKT and ERK signaling pathways. These findings further

support the potential of C14-PEI micelleplexes as a delivery system for gene editing and other therapeutic applications.

4.5 Conclusions

CRISPR-Cas9 has emerged as a highly effective and customizable tool for genome editing, holding promise for the treatment of *KRAS* mutations in lung cancer,[202,213,214] however, developing an efficient and bio-safe material is a key barrier. In this study, we introduce C14-PEI as a micelleplex system capable of efficiently co-delivering Cas9 mRNA and sgRNA to excise mutated *KRAS* alleles in lung cancer cells. C14-PEI is synthesized from 1,2-epoxytetradecane and branched PEI 600 Da via ring-opening reaction, exhibiting a CMC of 20.86 ± 0.15 mg/L. Effective condensation of mRNA via electrostatic interaction was demonstrated across all tested polymers, even at low concentrations. Specifically, C14-PEI at w/w of 4 and 8, under pH 7.4 conditions, as well as at w/w 4 under pH 5.4, were selected for detailed investigation based on mRNA expression levels, particle size, and material toxicity considerations. Optimal conditions were identified with C14-PEI at w/w 8 and pH 7.4, revealing micelleplexes with a hydrodynamic diameter of approximately 300 nm (PDI: 0.16) and a zeta potential of 40 mV. Notably, C14-PEI at w/w 8, pH 7.4, exhibited stable complex formation under physiological conditions as confirmed by the heparin competition assay, along with efficient endosomal escape properties intracellularly. Encapsulation efficiency of eGFP mRNA by C14-PEI reached 99% at w/w 8, resulting in a 130-fold increase in expression compared to the blank control. These findings underscore C14-PEI's potential as a robust delivery system for CRISPR-Cas9 components, highlighting its suitability for targeted genome editing applications in cancer therapy. The study revealed that C14-PEI micelleplexes effectively co-deliver Cas9 mRNA and sgRNA for targeted genome editing of *KRAS* mutations in lung cancer cells. Notably, while C14-PEI at a w/w 4 and pH 7.4 exhibited the highest eGFP expression (>1000-fold increase), it also displayed larger particle sizes (>1000 nm) and increased cytotoxicity in the CCK-8 assay. This phenomenon was attributed to aggregation, as confirmed by confocal laser scanning microscopy (CLSM)

during endosomal escape testing. Agarose gel analysis confirmed efficient co-encapsulation of Cas9 mRNA and sgRNA by C14-PEI micelleplexes. For gene editing purposes, at a sgRNA to Cas9 mRNA molar ratio of 10, C14-PEI micelleplexes demonstrated successful excision of the *KRAS* mutant with 62.67% and 64.64% indel efficacy at w/w 8 and w/w 4 pH 7.4, respectively. Droplet digital PCR (ddPCR) further confirmed edited gene copies at 37.8% and 48.5% for w/w 8 and w/w 4 prepared at pH 7.4, respectively. Deletions and insertions under 16 base pairs were predominant in the edited gene sequences, as revealed by Sanger sequencing analysis. Following the deletion of *KRAS* G12S in A549 cells, downstream signaling was attenuated, as evidenced by decreased levels of phosphorylated-AKT and phosphorylated-ERK observed in western blot analysis. Moreover, the migration capability of A549 cells was impaired, and apoptosis was increased following treatment with C14-PEI micelleplexes containing Cas9 mRNA and sgRNA targeting *KRAS* G12S. These findings underscore the potential of C14-PEI as an efficient and relatively safe delivery system for CRISPR-Cas9-mediated genome editing, with implications for therapeutic interventions targeting *KRAS* mutations in lung cancer.

In conclusion, this study highlights the continuous evolution and potential of C14-PEI micelleplexes in advancing CRISPR-Cas9-based therapies for targeted genetic interventions, particularly in addressing mutations such as *KRAS* in cancer treatment. Leveraging the straightforward synthesis and functional groups of C14-PEI polymers, adjustments in chemical and physical properties can readily be made to enhance their efficacy as mRNA delivery agents and optimize their performance. This research affirms that hydrophobic modification of cationic polymers, C14-PEI, is conducive to designing drug delivery systems with improved cellular internalization capabilities and minimal toxicity. However, challenges remain, particularly concerning the size and zeta potential of micelleplexes, which may elicit immune responses and compromise efficiency *in vivo*. Addressing these issues is crucial for advancing toward clinical applications, and future efforts will focus on polymer modifications and composition adjustments to optimize micelleplex properties. Ongoing studies

also aim to incorporate anionic polymers into the optimized formulations to further tailor nanoparticle characteristics and enhance therapeutic outcomes.

4.6 Supplementary information

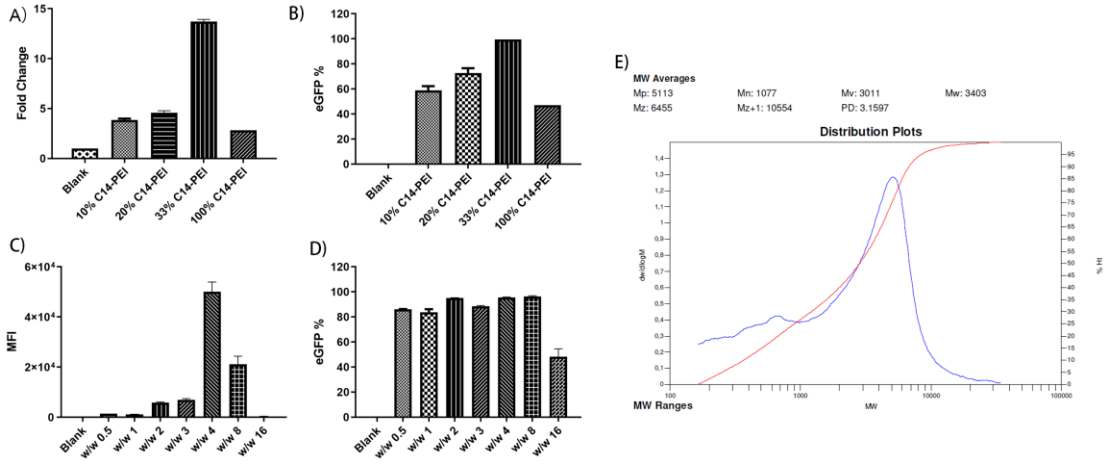

Figure S. Supplement data. A-B) eGFP mRNA expression with C14-PEI at different modification levels in A549 cells. Results are standardized fold change; **C-D)** eGFP mRNA expression with 33% C14-PEI at mass ratio in A549 cells; **D)** GPC analysis of 33% C14-PEI before purification.

4.7 Acknowledgements

The author Siyu Chen acknowledges the financial support from the China Scholarship Council (CSC). Simone Carneiro thanks the financial support from the Alexander von Humboldt Foundation and the Center of Nanoscience (CeNS) Munich. This research was also supported by ERC-2014-StG-637830 to Olivia Merkel. Thanks to Prof. Roland Beckmann and Dr. Otto Berninghausen for the technical support with Cryo-EM.

5. Chapter II

Anionic Polymer Coating for Enhanced Delivery of Cas9 mRNA and sgRNA Nanoplexes

Siyu Chen,[1] Simone Pinto Carneiro,[1] and Olivia Monika Merkel[1]

[1]Ludwig-Maximilians-University, Department of Pharmacy, Pharmaceutical Technology and Biopharmaceutics, Butenandtstraße 5-13, Munich, 81377, Germany

The following sections are adapted from the submitted manuscript.

5.1 Abstract

Polymeric carriers have long been recognized as one of the most effective and promising systems for nucleic acid delivery. In this study, we utilized an anionic di-block co-polymer, PEG-PLE, to enhance the performance of C14-PEI nanoplexes for delivering Cas9 mRNA and sgRNA targeting *KRAS* G12S mutations in lung cancer cells. Our results demonstrated that PEG-PLE, when combined with C14-PEI at a weight-to-weight ratio of 0.2, produced nanoplexes with a size of approximately 140 nm, a polydispersity index (PDI) of 0.08, and a zeta potential of around -1 mV. The PEG-PLE/C14-PEI nanoplexes at this ratio were observed to be both non-cytotoxic and effective in encapsulating Cas9 mRNA and sgRNA. Confocal microscopy imaging revealed efficient endosomal escape and intracellular distribution of the RNAs. Uptake pathway inhibition studies indicated that the internalization of PEG-PLE/C14-PEI primarily involves scavenger receptors and clathrin-mediated endocytosis. Compared to C14-PEI formulations, PEG-PLE/C14-PEI demonstrated a significant increase in luciferase mRNA expression and gene editing efficiency, as confirmed by T7EI and ddPCR, in A549 cells. Sanger sequencing identified insertions and/or deletions around the PAM sequence, with a total of 69% indels observed. Post-transfection, the KRAS-ERK pathway was downregulated,

resulting in significant increases in cell apoptosis and inhibition of cell migration. Taken together, this study reveals a new and promising formulation for CRISPR delivery as a potential lung cancer treatment.

5.2 Introduction

Clustered Regularly Interspaced Short Palindromic Repeats (CRISPRs) are sequences found in prokaryotic bacteria and archaea that function as part of an adaptive immune system. In 2012, Jennifer A. Doudna and Emmanuelle Charpentier introduced the CRISPR-Cas9 system as a groundbreaking tool for genome editing, marking a significant advancement in molecular biology[11]. Their pioneering work earned them the Nobel Prize in Chemistry in 2020. Among the various CRISPR-Cas systems, Cas9 stands out as the most widely used and extensively studied. The mechanism by which CRISPR-Cas9 targets and edits DNA is closely tied to its structure. The system relies on the Cas9 protein, a 160-kilodalton endonuclease with a bi-lobed architecture, composed of the REC and NUC lobes[24]. Cas9 forms a ribonucleoprotein complex with CRISPR RNA (crRNA) and trans-activating crRNA (tracrRNA), or a chimeric single-guide RNA (sgRNA), which guides it to the target double-stranded DNA (dsDNA)[23]. The sgRNA or crRNA-tracrRNA complex directs the Cas9 protein to cleave any DNA sequence that contains a 20-nucleotide complementary target sequence in the vicinity of the protospacer adjacent motif (PAM) sequence. This two-component system can be easily used in applied science by designing the sgRNA to target virtually any DNA sequence in the genome, enabling precise site-specific double-strand breaks (DSBs). Once the DSB is introduced by Cas9, the cell can repair the breakthrough of two primary pathways: nonhomologous end joining (NHEJ) or homology-directed repair (HDR). NHEJ often results in small insertions or deletions (indels) at the cleavage site, while HDR allows for precise genome modification using a homologous repair template. Due to its efficiency, versatility, and relatively low cost, CRISPR-Cas9 has become a powerful and customizable tool for genome editing, offering advantages such as rapid onset, transient expression, and minimal off-target effects[215].

CRISPR-Cas9 delivery methods typically include plasmid DNA[4],

mRNA/sgRNA[5], and protein/sgRNA ribonucleoprotein complexes (RNPs)[6]. Over the past two decades, mRNA delivery technology has seen significant advancements. Most notably, the rapid development and widespread use of mRNA vaccines have played a crucial role in combating the COVID-19 pandemic[71]. The success of nucleoside-modified mRNA-LNP vaccines developed by Moderna and Pfizer/BioNTech against SARS-CoV-2 marked a pivotal moment, establishing mRNA therapeutics as a viable approach in modern medicine. While mRNA vaccines have demonstrated the potential of mRNA delivery in nucleic acid therapy, the therapeutic applications of mRNA extend far beyond vaccines for infectious diseases. mRNA-based CRISPR-Cas9 therapeutics offer several distinct advantages[7,8]. One key benefit is the ability to achieve transient expression, providing controlled and time-limited therapeutic effects[72]. This feature reduces the risk of off-target effects, enabling more precise and safer delivery. Additionally, mRNA-based systems avoid the risk of genomic integration, thereby preserving the integrity of the host genome[56]. Combined with their lower immunogenicity compared to viral vectors, these factors underscore the safety and growing interest in mRNA-based CRISPR-Cas9 delivery. Despite these advantages, effective delivery of mRNA *in vivo* and *in vitro* remains a significant challenge, limiting the full potential of CRISPR-mediated gene editing[56]. Various strategies are being explored to address this challenge, including viral delivery[216], cell-penetrating peptides (CPPs)[47], gold nanoparticles (AuNPs)[217], lipid nanoparticles (LNPs)[101], and polymeric carriers[100]. Among these, polymer-based delivery systems, though often overlooked in favor of lipid nanoparticles, offer unique benefits. They allow for precise tuning of chemical properties to enhance mRNA protection, favorable pharmacokinetics, and targeted delivery[89]. One of the most commonly used cationic polymers for nucleic acid delivery is polyethylenimine (PEI) [218]. PEI is known for its high loading capacity, efficient cellular internalization, strong endosomal disruption, and low cost[89]. However, its strong cationic nature also poses challenges, including toxicity, which can lead to necrosis, apoptosis, and inflammation[219]. In the context of mRNA delivery, PEI tends to have relatively low transfection efficiency because its strong binding to RNA can impair mRNA release from the complex[220]. Therefore, optimizing PEI-

based vehicles is essential for achieving safe and efficient mRNA delivery.

In our earlier study (Chapter I), we developed a lipid-modified polyethylenimine (C14-PEI) nanoplex system to co-deliver Cas9 mRNA and sgRNA, achieving promising gene editing results in A549 lung cancer cells. However, this system exhibited a big size and a highly positive zeta potential, which may limit its effectiveness *in vivo*. To enhance the biophysical and chemical properties of nanoparticles for *in vivo* applications, non-cationic polymers are often employed as core or shell stabilizers for mRNA and for positively charged segments[218]. These polymers contribute to surface adsorption or charge shielding, improving the nanoparticles' performance. Among these, poly(ethylene glycol) (PEG) is widely recognized for its role in drug delivery[221]. PEG is highly hydrophilic and electrostatically neutral, and when present on the surface of nanoparticles, it provides colloidal stability through steric repulsion, which increases with the length of the PEG chains[222,223]. Modifying PEI-based nanoparticles with PEG terminal groups has shown promise in targeting lung tissues, though this modification reduces stability against heparin compared to unmodified PEI polyplexes[224]. Additionally, negatively charged macromolecules can serve as protective shells, shielding the positively charged nanoparticles and prolonging their circulation time in the bloodstream[225-227]. For instance, anionic polysaccharides can either covalently bond with cationic materials or incorporate directly into nucleic acid complexes via electrostatic interactions, effectively masking the cationic regions of the delivery carriers[221]. These findings underscore the significant role that PEG chains with anionic groups play in the performance of polyplexes. They also highlight the need for further research to fully understand how non-cationic block co-polymers influence mRNA delivery in CRISPR-Cas9 gene editing applications.

In this study, we utilized methoxy-poly(ethylene glycol)-block-poly(l-glutamic acid sodium salt) (PEG-b-PLE) as an auxiliary component in the C14-PEI delivery system to target mutated *KRAS* with Cas9 mRNA and sgRNA. We systematically characterized and compared the C14-PEI and PEG-PLE/C14-PEI nanoparticles in terms of size, zeta potential, cytotoxicity, and encapsulation efficiency. The duration and degradation of the Cas9 mRNA and

sgRNA were monitored using colocalization techniques under confocal laser microscopy. We also investigated the cellular uptake pathways and endosomal entrapment, followed by an assessment of luciferase mRNA expression and gene editing efficiency in A549 lung cancer cells. To evaluate the therapeutic relevance, we performed western blot analysis, wound healing assays, and cell apoptosis tests.

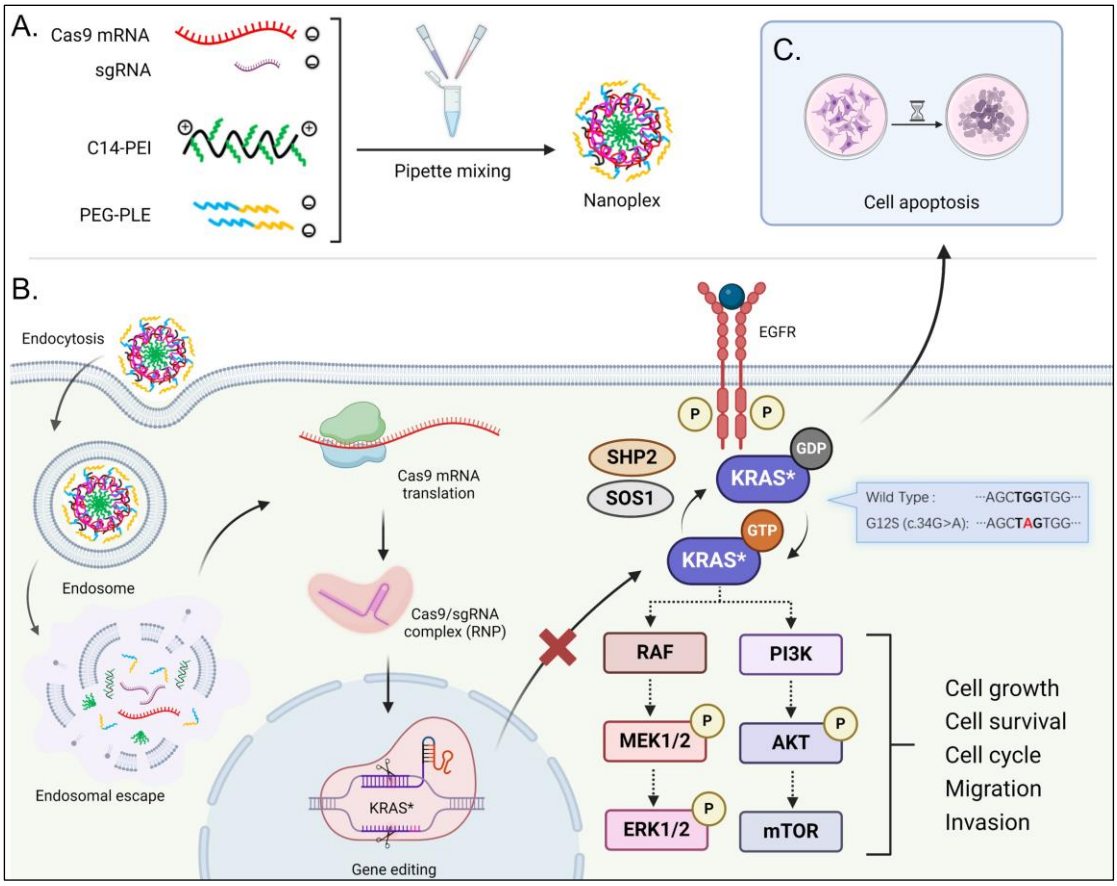

Schematic 1. The strategy of PEG-PLE/C14-PEI for co-delivery of Cas9 mRNA and sgRNA targeting KRAS G12S. A. PEG-PLE/C14-PEI nanoplexes were prepared by pipette mixing through electrostatic interactions; B. Cas9 mRNA and sgRNA are released from nanoplexes and form CRISPR RNPs after mRNA translation to mediate gene editing in cell nuclear, leading to the downregulation of downstream signals; **C.** The deletion of *KRAS* G12S results in lung cancer cell apoptosis.

5.3 Materials & Methods

5.3.1 Materials

Methoxy-poly(ethylene glycol) (5,000 Da)-block-poly(l-glutamic acid sodium salt) (7,500 Da) (PEG-b-PLE) was obtained from Alamanda Polymers (Huntsville, AL, US). 1,2-epoxytetradecane, Branched PEI 600 Da, 4-(2-hydroxyethyl)-1-piperazineethanesul-fonic acid (HEPES), Dulbecco's Phosphate Buffered Saline (PBS), 0.05% trypsin-EDTA, Tris-buffered saline, Tween 20, RPMI-1640, fetal bovine serum (FBS), Penicillin-Streptomycin solution, 6-diamidino-2-phenylindole dihydrochloride (DAPI), skim milk, heparin, pyrene, paraformaldehyde (PFA), agarose powder, and Cell Counting Kit-8 were purchased from Sigma-Aldrich (Darmstadt, Germany). SYBR™ Gold Stain, SYBR Safe DNA Gel Stain, Lipofectamine™ 2000, LysoTracker™ Green DND-26, Annexin V-AF488, GeneArt™ Genomic Cleavage Detection Kit, Phusion Hot Start II High-Fidelity PCR Mastermix, ExoSAP-IT™ Express PCR Product Cleanup Reagent, Pierce™ BCA Protein Assay kit, Novex™ WedgeWell™ 8-16% Tris-Glycin gel, Pierce™ Protease Inhibitor Tablets, RIPA buffer, SuperSignal™ West Femto Maximum Sensitivity Substrat were bought from Thermo Fisher Scientific (Planegg, Germany). ddPCR NHEJ Gene Edit Assay (primers and probes), ddPCR Supermix for Probes (no dUTP), cartridges, gaskets, droplet generation oil, and droplet reader oil were purchased from Bio-Rad, US. RNeasy Mini Kit (QIAGEN, US), pCp-AF488 (Jena Bioscience, Germany), Oligo Clean & Concentrator Columns (Zymo, Germany), Luciferase mRNA (RiboPro, Niederland), CleanCap® Cas9 mRNA (5moU) (Trilink Biotechnologies, US), cOmplete™ EDTA-free Protease Inhibitor Cocktail (Roche, Germany), Rotiphorese®NF 10x TBE Buffer (Carl Roth, Germany), propidium iodide (PI) (BD Biosciences, US), DNeasy Blood & Tissue Kit (Qiagen, US), and Amersham™ Protran® Western blotting nitrocellulose membranes (Cytiva technologies, Germany) were obtained from the suppliers indicated. Methanol, ethanol, and acetone were provided by Ludwig-Maximilians-University Munich. The primary antibodies for p44/42 MAPK (Erk1/2) and Phospho-p44/42 MAPK (T202/Y204) were from Cell Signaling

Technology (Danvers, MA, US). KRAS polyclonal antibody, Histone-H3 polyclonal antibody, and HRP-conjugated affinipure goat anti-rabbit IgG (H+L) secondary antibody are from Proteintech (Planegg, Germany). Cy5-mRNA was synthesized and labeled in the laboratory. sgRNA (*KRAS* G12S: 5'-CUUGUGGUAGUUGGAGCUAG-3') was synthesized by Sigma-Aldrich. Primers for PCR (F: TTTGAGAGCCTTTAGCCGC, R: TCTACCCTCTCACGAAACTC) and primers for Sanger sequencing (F: TCTTAAGCGTCGATGGAG, R: ACAGAGAGTGAACATCATGG) were synthesized by Sigma-Aldrich (Darmstadt, Germany).

5.3.2 C14-PEI Synthesis

C14-PEI was synthesized by reacting 1,2-epoxytetradecane with branched PEI 600 Dalton through a ring cleavage reaction as in the previous description (Chapter I Section 4.3.3). Briefly, 1,2-epoxytetradecane and bPEI 600 Da were heated at 95°C in absolute ethanol for 72 h while stirring. The product was then dialyzed with a 1000 Da cutoff in absolute ethanol, followed by ethanol removal using high-pressure nitrogen air.

5.3.3 Nanoparticle Preparation

C14-PEI nanoparticles were prepared as the previous description (Chapter I Section 4.3.5). Specifically, 500 ng of luciferase mRNA or Cas9 mRNA with sgRNA at a molar ratio of 1:10 was added into 100 μL of 10 mM HEPES buffer, pH 7.4, and C14-PEI solution with an eightfold weight excess in comparison to total RNA (w/w 8) were added and mixed with RNA by pipetting and vortexing in HEPES buffer. The mixture was then incubated at room temperature for 1 hour. For PEG-PLE/C14-PEI nanoparticles, a predetermined amount of PEG-PLE was added to the RNA solution in the first step, which was then mixed with C14-PEI in HEPES buffer. The morphology of the polyplexes was examined using cryo-electron microscopy (Cryo-EM).

5.3.4 Nanoparticle Characterization

The size, polydispersity indices (PDI), and zeta (ζ) potential of nanoparticles were characterized using a Zetasizer Ultra (Malvern, UK). The nanoparticle suspension was added to a disposable micro-cuvette, and the hydrodynamic diameter and PDI were measured three times per sample using dynamic light scattering (DLS) at a 173° backscatter angle. Subsequently, the same suspension was transferred to a folded capillary cell for each sample to determine the zeta potential in triplicate using laser Doppler anemometry (LDA), with each run consisting of up to 100 scans. Results are presented as mean ± standard deviation (SD, n=3).

Nanoparticle Tracking Analysis (NTA) combines light scattering and Brownian motion to determine the size distribution of nanoplexes in liquid suspension. By tracking individual particles' mean squared displacement, the NTA software calculates their hydrodynamic diameter using the Stokes-Einstein equation.[228] Using the NanoSight Pro system (Malvern Instruments, Amesbury, UK), subtle changes in particle population characteristics are detected, with real-time visual validation. For measurement, nanoplexes were vortexed and diluted in particle-free HEPES buffer to achieve a concentration within the recommended range ($1x10^6$–$1x10^9$ particles/mL). Videos were captured using the NanoSight NTA software version 3.4 in script control mode (3 videos, each 60 s) at 25°C, with a syringe pump speed of 20. Each video consisted of 1500 frames, and camera levels were adjusted according to the scatter properties of the first measurement. Video analysis settings were fine-tuned by increasing the screen gain and adjusting the detection threshold for optimal single-particle tracking, while other parameters were set to default or automated.

5.3.5 SYBR Gold Assay

To evaluate the mRNA encapsulation capacity of PEG-PLE/C14-PEI nanoparticles, SYBR Gold assays were conducted. SYBR Gold is a cyanine dye that binds to nucleic acids and exhibits fluorescence upon excitation. Briefly, nanoparticles were prepared as described earlier at weight-to-weight (w/w)

ratio of 8 and with the addition of PEG-PLE to C14-PEI at weight-to-weight (w/w) ratios of 0, 0.1, 0.2, 0.3, 0.4, and 0.5. Subsequently, 100 μL of each polyplex solution was added to black FluoroNunc 96-well plates (Fisher Scientific, Germany). A 4x SYBR Gold aqueous solution (30 μL per well) was then added to each well and incubated for 10 min in the dark. The fluorescence intensity was measured using a fluorescence plate reader (TECAN, Switzerland) with excitation at 485/20 nm and emission at 535/20 nm. The fluorescence intensity of free mRNA (polymer to RNA w/w = 0) was used as a control and set as 100% fluorescence.

5.3.6 Agarose Gel Electrophoresis

Agarose gel electrophoresis was used to confirm the co-encapsulation of Cas9 mRNA and sgRNA and to perform the T7 endonuclease I (T7EI) assay. For each run, a 1% agarose gel, containing SYBR Safe dye at a 1:100,000 dilution, was prepared in Tris Borate EDTA (TBE) buffer. The nanoparticle samples, free RNA, and products from the T7EI assay were mixed with 6x DNA loading dye and then loaded onto the gel. Electrophoresis was carried out at 150 V for 40 min, and the gel was visualized using the ChemiDoc imaging system (Bio-Rad, US).

5.3.7 Cell Culture

A549 cells were cultured in complete RPMI-1640 medium supplemented with 10% heat-inactivated fetal bovine serum (FBS) and 1% penicillin-streptomycin. All cells were subcultured, maintained, and grown in an incubator at 37°C in humidified air with 5% CO_2.

5.3.8 Cytotoxicity Test

The cytotoxicity of nanoparticles was assessed using a CCK-8 assay in A549 cells. Specifically, 10,000 cells per well were seeded 24 h prior in a transparent 96-well plate (Fisher Scientific, Hampton, NH, USA). PEG-PLE/C14-PEI nanoparticles were freshly prepared at polymer w/w 0.5 and w/w 0.2. C14-PEI

nanoplexes were used as a control. After removing the old medium, the fresh medium containing nanoparticles with different concentrations (1x, 5x, 10x, 20x, 40x, and 80x fold increase of PEG-PLE/C14-PEI w/w 0.2) was added to each well and incubated for 24 h at 37°C and 5% CO_2. Subsequently, the medium was aspirated, and a fresh medium containing CCK-8 solution (10 µL CCK-8 in 100 µL RPMI-1640 media) was added to each well. After incubating for 4 h, a water-soluble orange formazan product formed in the medium, and absorbance was measured at 450 nm using a Tecan plate reader. The experiment was conducted in triplicate, and the results are presented as mean values (n=3), normalized to the percentage of viable cells relative to untreated cells (100% viability).

5.3.9 Uptake Pathway

To investigate the route of nanoparticle uptake, experiments with different types of specific uptake inhibitors were performed[194]. A549 cells (100,000 per well) seeded 24 h prior to the experiment were incubated with nystatin (20 µg/mL), dextran sulfate (100 µg/mL), chlorpromazine (5 µg/mL), or methyl-beta-cyclodextrin (1 mg/mL) for 1 h followed by incubation with C14-PEI or PEG-PLE/C14-PEI nanoparticles containing Cy5-labeled mRNA for 2 h. Incubation at 4°C for energy inhibition was set as a control. Positive control cells without inhibitor treatment were transfected with polyplexes, and untreated cells served as a blank control. After 2 h of transfection, the cells were washed with PBS and detached using 0.05% trypsin-EDTA. The detached cells were then collected in 1.5 mL Eppendorf tubes and centrifuged at 300 g for 5 min. After centrifugation, the supernatant was aspirated, and the cells were washed again with PBS, followed by a second centrifugation step. The resulting cell pellet was resuspended in fresh PBS, and the fluorescence intensity was measured using an Attune NxT flow cytometer (Thermo Fisher, Planegg, Germany) with excitation at 651 nm and emission at 670 nm. The experiments were performed in triplicate. Results are shown as a percentage of median fluorescence intensity normalized to not inhibited positive control samples (100%).

5.3.10 Endosomal Entrapment

To visualize the endosomal entrapment of nanoplexes, A549 cells were imaged using confocal laser scanning microscopy (CLSM, Leica SP8 inverted; software: LAS X, Leica Microsystems GmbH, Wetzlar, Germany) following transfection with fluorescently labeled mRNA. A total of 10,000 A549 cells were seeded into ibiTreat µ-Slide 8-well plates (ibidi, Gräfelfing, Germany) and transfected with PEG-PLE/C14-PEI (w/w 0.5) containing Cy5-mRNA. Lipofectamine 2000, PEI nanoparticles, and free Cy5-mRNA were used as controls. After incubation at 37°C with 5% CO_2 for 4, 8, or 24 h, the cells were stained with LysoTracker Green DND-26 in pre-warmed cell culture medium for 1 hour. Following medium removal, cells were washed and fixed with 4% paraformaldehyde (PFA) for 15 min in the dark and then washed again with PBS. DAPI was added to the appropriate wells at a final concentration of 1 µg/mL in PBS and incubated for 20 min at room temperature in the dark. After washing, the cells were maintained in PBS at 4°C for subsequent analysis by CLSM. For imaging, excitation was achieved using a diode laser at 405 nm, an argon laser at 488 nm, and a helium-neon laser at 650 nm. Emission was recorded in the blue channel (420–480 nm) for DAPI, the green channel (500–550 nm) for LysoTracker Green, and the red channel (650–720 nm) for Cy5-mRNA fluorescence.

5.3.11 Co-localization of mRNA and sgRNA

To assess the duration and degradation of Cas9 mRNA and sgRNA within cells using PEG-PLE/C14-PEI nanoparticles, we employed co-localization techniques with CLSM. Cas9 mRNA and sgRNA were labeled with Cy5 and AF488, respectively, for visualization. Cas9 mRNA was synthesized through *in vitro* transcription (IVT) using a mixture of nucleoside triphosphosphates (NTPs) containing Cy5-UTP (Jena Bioscience, Germany). The linearized DNA templates, NTP mixture, Cy5-UTP, and T7 polymerase were combined according to the HiScribe® T7 ARCA mRNA Kit with tailing (NEB, US) protocol. The reaction was incubated overnight at 37°C, and the RNA products were

purified using the RNeasy Mini Kit (Qiagen, Hilden, Germany) and verified by agarose gel electrophoresis. For sgRNA labeling, pCp-AF488 (Jena Bioscience, Germany) was added at the 3' end. The reaction mixture included sgRNA, pCp-AF488, ATP, T4 RNA Ligase, Reaction Buffer, RNAse inhibitor, 10% DMSO, and 15% PEG8000, which was incubated for 18 h at 16°C. The AF488-labeled sgRNA was purified from the reaction mix using Oligo Clean & Concentrator Columns (Zymo, Germany) and analyzed by UV/VIS spectroscopy (A260 nm: total RNA population; A494 nm: AF488-labeled RNA). A549 cells were transfected with PEG-PLE/C14-PEI nanoparticles containing Cy5-labeled Cas9 mRNA and AF488-labeled sgRNA. At various time points (1h, 4h, 8h, 24h, 36h, and 48h), cells were fixed with 4% paraformaldehyde (PFA) and nuclei were stained with DAPI. Images were captured using CLSM and analyzed with ImageJ to determine the duration and degradation of the mRNA and sgRNA.

5.3.12 Luciferase mRNA Expression

To evaluate the translational efficiency of mRNA delivered by PEG-PLE/C14-PEI, we quantified the expression of the luciferase protein reporter mRNA (Fluc mRNA) using a plate reader (TECAN, Männedorf, Switzerland). A549 cells were seeded at a density of 10,000 cells per well in 96-well plates containing 200 µL of growth medium. Following incubation in a cell culture incubator (37 °C, 5% CO_2) for 24 h, the cells were transfected with PEG-PLE/C14-PEI nanoparticles encapsulating Fluc mRNA at w/w 0, w/w 0.1, w/w 0.2, w/w 0.3, w/w 0.4, w/w 0.5. PEI served as a control treatment. After 24 h of transfection, cells were washed with PBS and lysed by lysis buffer followed by incubation at room temperature for 30 mins. Of each sample, 35 µL lysate was added to a white 96-well plate, and the samples were activated by 0.25 mM luciferin substrate with an autosampler (TECAN, Männedorf, Switzerland). Subsequently, the samples were measured for the relative light unit (RLU) of luminescence with the plate reader. Results are presented as mean ± standard deviation (SD, n=3).

5.3.13 T7 Endonuclease I (T7EI) Assay

The T7EI assay was conducted according to the manufacturer's protocol using the GeneArt™ Genomic Cleavage Detection Kit. A549 cells were initially seeded in 6-well plates at a density of 100,000 cells per well in 1.5 mL of medium 24 h before the experiment. Following a media change, cells were transfected with PEG-PLE/C14-PEI nanoparticles containing Cas9 mRNA and sgRNA. Lipofectamine 2000, PEI, and C14-PEI were included as controls. Transfected cells were then incubated at 37°C with 5% CO_2 for 48 h. Subsequently, cells were washed with PBS, harvested using 0.05% trypsin-EDTA, and collected by centrifugation into 1.5 mL Eppendorf tubes. The cell pellets were lysed using lysis buffer, and the resulting lysates were utilized for polymerase chain reaction (PCR) amplification of sequences containing *KRAS* alleles. Following PCR amplification, the PCR products underwent re-annealing and treatment with the detection enzyme as per the kit's instructions. The positive control sample provided in the kit was included for validation. Agarose gel electrophoresis was performed to visualize the cleavage products, and images were captured using the ChemiDoc imaging system as described in section 5.3.6. Data analysis was conducted using Image Lab Software.

5.3.14 Droplet Digital PCR

A549 cells were transfected in 6-well plates using PEG-PLE/C14-PEI nanoparticles with Cas9 mRNA and sgRNA for 48 h, with Lipofectamine 2000, PEI, and C14-PEI used as controls. Genomic DNA was extracted from both untreated and treated A549 cells using the DNeasy Blood & Tissue Kit (Qiagen), and the DNA concentration was quantified using a Nanodrop spectrophotometer. Primers and probes were custom-designed and obtained from Bio-Rad (Feldkirchen, Germany). The reaction mixtures for droplet digital PCR (ddPCR) contained 2x ddPCR Supermix for Probes (no dUTP), with final concentrations of 900 nM for each primer and 250 nM for each FAM- or HEX-labeled probe. A total of 100 ng of template DNA was added to achieve a final reaction volume of 20 µL. Standard Bio-Rad reagents and consumables,

including cartridges, gaskets, droplet generation oil, and droplet reader oil, were used. After droplet generation, droplets were carefully transferred to a 96-well PCR plate and sealed using the PX1 PCR Plate Sealer (Bio-Rad). The PCR conditions were as follows: initial denaturation at 95°C for 10 min, followed by 40 cycles of denaturation at 94°C for 30 s, annealing/extension at 55°C for 3 min, and a final extension step at 98°C for 10 min, followed by a hold at 4°C. The ramp rate was set at 2°C/s. Droplets were read using the QX200 Droplet Reader (Bio-Rad), and each reaction included a no-template control. Data analysis was performed using QuantaSoft Software[185].

5.3.15 Sanger Sequencing

Genomic DNA was extracted from A549 cells 48 h post-transfection with PEG-PLE/C14-PEI nanoparticles using the DNeasy Blood & Tissue Kit. To visualize the gene sequence after gene editing, PCR was performed using a pair of primers designed to target regions before and after the cleavage site, yielding a PCR product of approximately 500 base pairs. The Phusion Hot Start II High-Fidelity PCR Mastermix was utilized for PCR amplification. The cycling conditions were as follows: initial denaturation at 98°C for 30 s, followed by 35 cycles of denaturation at 98°C for 10 s, annealing at 61.5°C for 30 s, extension at 72°C for 30 s, and a final extension at 72°C for 10 min. PCR products were verified by electrophoresis on 1% agarose gels. Following gel verification, PCR products were purified using the ExoSAP-IT™ Express PCR Product Cleanup Reagent. The purified PCR products were subsequently used for Sanger sequencing to determine the sequence changes resulting from the gene editing process. The results were analyzed by the ICE CRISPR analysis tool[186].

5.3.16 Western Blot

To assess the ability of PEG-PLE/C14-PEI nanoparticles to inhibit downstream signals in the KRAS pathway, A549 cells were seeded in 6-well plates and allowed to grow for 24 h to reach a density of $1x10^5$ cells per well. The cells were then treated with PEG-PLE/C14-PEI nanoparticles and incubated at 37°C with 5% CO_2 in a humidified incubator for 48 h. Following treatment, cells were

washed with ice-cold PBS and lysed in RIPA buffer containing phosphatase inhibitors and protease inhibitors. The protein content in the lysates was quantified using the Pierce™ BCA Protein Assay kit (Thermo Fisher), and equal amounts of protein were loaded onto SDS-PAGE (Novex™ WedgeWell™ 8-16% Tris-Glycin gel). Separated proteins were then transferred onto nitrocellulose membranes, which were subsequently blocked with 5% skim milk in TBST (Tris-buffered saline with 1% Tween 20) for 1 hour at room temperature. Membranes were then incubated overnight at 4°C with primary antibodies targeting specific proteins of interest in the KRAS pathway. After primary antibody incubation, membranes were washed three times with 1% TBST and then incubated with horseradish peroxidase (HRP)-conjugated secondary antibodies at room temperature for 1 h. Protein bands were visualized using chemiluminescence substrates and imaged immediately using the ChemiDoc imaging system (BioRad). Between antibody stainings, membranes were treated with stripping buffer for 30 min to remove bound antibodies, followed by washing with TBST and re-blocking with 5% skim milk in TBST solution. This systematic approach allowed for the quantification of protein expression levels involved in the KRAS pathway inhibition following treatment with C14-PEI nanoplexes, providing insights into their therapeutic potential[187].

5.3.17 Wound Healing Assay

The µ-Dish with culture-insert 2 well (ibidi) was utilized for conducting a wound healing assay[188]. Initially, 10,000 A549 cells suspended in 70 µL of RPMI-1640 media were added to each well and allowed to incubate at 37°C with 5% CO_2 for a minimum of 24 h to achieve a confluent cell layer. Following incubation, the insert was carefully removed using sterile tweezers, and the cell layer was washed twice with PBS to eliminate any cell debris and non-adherent cells. Subsequently, the µ-Dish was filled with 2 mL of fresh complete medium containing either PEG-PLE/C14-PEI nanoparticles or Lipofectamine 2000, as per experimental requirements. The cells were maintained in the incubator at 37°C with 5% CO_2 throughout the experiment, and images were captured at 0, 4, 8, and 24 h using an EVOS microscope (Thermo Fisher, Germany). The area of the wound gap was quantified and analyzed using ImageJ software,

providing insights into the migration and healing dynamics of the A549 cell monolayer in response to the treatments administered.

5.3.18 Cell Apoptosis

Annexin V and propidium iodide (PI) staining allowed for the quantification of apoptotic and necrotic cells, providing insights into the cellular response toward PEG-PLE/C14-PEI nanoparticle transfection[189]. A total of $1x10^5$ cells per well were initially seeded onto a 6-well plate in RPMI-1640 complete medium and transfected with PEG-PLE/C14-PEI nanoparticles. Following a 48-hour incubation at 37°C with 5% CO_2, the cells were washed twice with cold PBS and resuspended in Annexin V Binding Buffer at a concentration of $1x10^6$ cells/mL. Subsequently, 100 µL of the cell suspension was mixed with 10 µL of Annexin V-AF488 (Thermo Fisher) and 1 µL of PI (BD Biosciences), and the mixture was incubated for 15 min at room temperature in the dark. After incubation, 400 µL of Annexin V Binding buffer was added to each tube to halt the reaction. Fluorescence signals from Annexin V-AF488 and PI staining were measured using the Attune NxT flow cytometry (Thermo Fisher, Germany), and the data were analyzed using FlowJo software.

5.3.19 Statistics

Unless otherwise specified, all results are presented as the mean value ± standard deviation (SD) based on triplicate experiments (n=3). Statistical analyses were performed using GraphPad Prism software (GraphPad Software, USA).

5.4 Results and Discussions

5.4.1 Nanoparticle Preparation

In our previous report (Chapter I), we developed a C14-PEI nanoplex system for delivering Cas9 mRNA and sgRNA, which showed promising gene editing

in A549 cells despite its large size and high positive zeta potential. Literature suggests that coating with anionic polymers can shield positive charges and enhance the properties of nanoparticles, making PEG-PLE a potential candidate for this purpose[221,225,227]. We prepared C14-PEI nanoplexes with mRNA at a w/w ratio of 8 in 10 mM HEPES buffer at pH 7.4 and coated these nanoplexes with PEG-PLE at various mass ratios relative to C14-PEI.

The hydrodynamic diameter, PDI, and ζ potential of the nanoparticles were measured using DLS and LDA, respectively. As shown in Figure 1A, without PEG-PLE coating, the C14-PEI nanoplexes with mRNA at a w/w ratio of 8 had a size of approximately 400 nm and a PDI of 0.3. In contrast, PEG-PLE/C14-PEI nanoparticles exhibited sizes ranging from 100 to 200 nm for PEG-PLE to C14-PEI ratios of 0.1 to 0.5, with an average PDI of 0.1. Even with a minimal amount of PEG-PLE at a polymer w/w ratio of 0.1, the nanoparticles maintained a compact size and effective charge shielding. Theoretically, at a mass ratio of 2.6, PEG-PLE is expected to neutralize the positive charges of C14-PEI. However, a neutral charge was experimentally found around PEG-PLE/C14-PEI w/w 0.1, while nanoparticles at w/w 2 exhibited strong negative zeta potentials, indicating an excess of anions in the system (Figure 1B). This can be attributed to the random polymer modification process, which may lead to errors in the N/P calculation.

C14-PEI nanoplexes had a zeta potential of approximately 40 mV. Increasing PEG-PLE content reduced the zeta potential, reaching near-neutral values (0 mV) at a polymer w/w ratio of 1.5 and transitioning to negative values at polymer w/w ratios of 2 and above. As the ratio increased, the zeta potential became more negative, ranging from -1.0 to -14 mV (Figure 1B). Nanoparticles with zeta potentials between +10 mV and -10 mV are approximately neutral and often considered ideal, as this range provides sufficient electrostatic repulsion to prevent agglomeration, maintain stability, and reduce interactions with negatively charged cell membranes, thus reducing potential cytotoxicity and immune responses[191,229]. Based on these properties, PEG-PLE/C14-PEI nanoparticles with polymer w/w ratios of 0.2 and 0.5 were selected for further experiments.

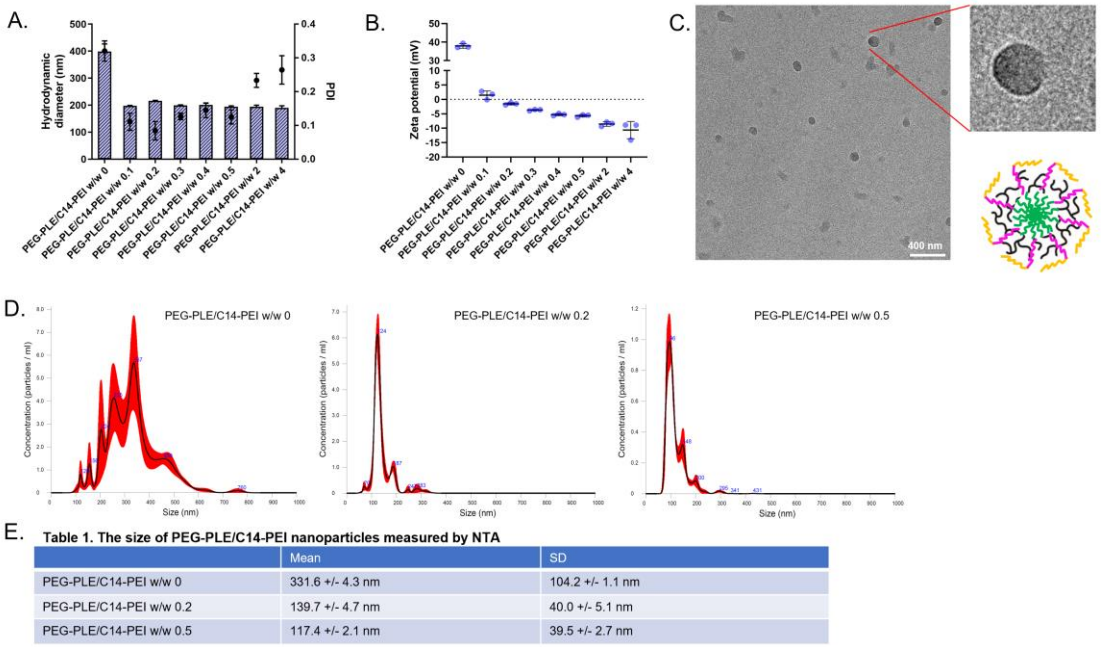

E. **Table 1. The size of PEG-PLE/C14-PEI nanoparticles measured by NTA**

	Mean	SD
PEG-PLE/C14-PEI w/w 0	331.6 +/- 4.3 nm	104.2 +/- 1.1 nm
PEG-PLE/C14-PEI w/w 0.2	139.7 +/- 4.7 nm	40.0 +/- 5.1 nm
PEG-PLE/C14-PEI w/w 0.5	117.4 +/- 2.1 nm	39.5 +/- 2.7 nm

Figure 1. Characterization of PEG-PLE/C14-PEI. A) hydrodynamic diameters (bars) and polydispersity indices (PDI, dots) of nanoplexes (n=3); **B)** zeta potentials of nanoplexes (n=3); **C)** Cryo-EM image of PEG-PLE/C14-PEI with the according particle scheme; **D)** size distributions of PEG-PLE/C14-PEI measured by NTA; **E)** NTA results.

To further verify the size of PEG-PLE/C14-PEI nanoparticles, we employed Nanoparticle Tracking Analysis (NTA) using a Malvern NanoSight Pro system. As shown in Figures 1D and 1E, the C14-PEI nanoparticles had an average size of 331.6 ± 4.3 nm with a standard deviation (SD) of 104.2 ± 1.1 nm. In comparison, PEG-PLE/C14-PEI nanoparticles with w/w ratios of 0.2 and 0.5 measured 139.7 ± 4.7 nm (SD: 40.0 ± 5.1 nm) and 117.4 ± 2.1 nm (SD: 39.5 ± 2.7 nm), respectively, indicating that the presence of PEG-PLE resulted in smaller and more uniformly sized nanoparticles. The sizes obtained from NTA were smaller than those measured by DLS. This discrepancy arises from the different methodologies employed by the two techniques. NTA tracks the trajectories of individual particles under a microscope, correlating their movement to size. In contrast, DLS measures the intensity fluctuations of scattered light, which reflects particle diffusion[230]. Larger particles can dominate the scattered light signal in DLS, potentially dominating over smaller particles and leading to less accurate size determination[231,232]. This explains the broader size range and lower reproducibility observed with DLS for the C14-PEI formulation.

Cryo-electron microscopy (Cryo-EM) was used to confirm the micelle structure of C14-PEI and to examine the morphology of PEG-PLE/C14-PEI nanoparticles. As shown in Figure 1C, PEG-PLE/C14-PEI nanoplexes displayed a spherical shape with a more compact surface compared with C14-PEI nanoplexes (Figure SA.). A distinct shadow on the surface indicates the presence of PEG-PLE coating.

5.4.2 Cytotoxicity

Cationic carriers facilitate the delivery of nucleic acids by interacting with cell membranes through electrostatic forces. However, an excess of cationic materials can disrupt the dynamic cell membrane and cause significant cytotoxicity[219,233]. By neutralizing the cationic charges, negatively charged polymers can offer improved biocompatibility compared to traditional cationic delivery systems.[221] To evaluate cytotoxicity, we used the CCK-8 assay, which measures the intracellular reduction of tetrazolium salt (WST-8) to produce an orange water-soluble formazan dye. This reaction, facilitated by the electron carrier 1-Methoxy PMS, produces a dye whose absorbance correlates linearly with the number of metabolically active cells, providing a direct measure of cytotoxicity. We assessed PEG-PLE/C14-PEI nanoplexes at polymer w/w ratios of 0.2 and 0.5 across various concentrations (1x, 5x, 10x, 20x, and 40x increase based on the w/w 0.2 ratio) and compared them with C14-PEI complexes and a lysis buffer control. As shown in Figure 2A, compared with PEI-C14 which illustrated 82% valid cells, PEG-PLE/C14-PEI nanoplexes showed less toxicity at w/w 0.2 and w/w 0.5 (98% and 101% valid cells respectively). This indicates that nanoplex biosafety and biocompatibility are improved with the shield for positive charges. However, at higher concentrations, cell viability decreased significantly. Cytotoxicity began to increase noticeably at a 5-fold concentration, resulting in 75% cell death. At a 40-fold increase, cell death approached 98%, comparable to the lysis buffer positive control.

5.4.3 Encapsulation

Encapsulation efficiency is crucial for evaluating mRNA delivery systems due

to mRNA's inherent instability and susceptibility to degradation by nucleases[57]. To assess encapsulation, we used SYBR Gold, a fluorescent dye that binds to free nucleic acids and fluoresces upon excitation at 495 nm[194]. This method leverages the interaction between cationic polymers and the negatively charged phosphate groups of mRNAs, which promotes mRNA encapsulation within nanoparticles through charge complexation. As a result, the fluorescence intensity of SYBR Gold decreases, allowing for the quantification of free mRNA in nanoparticle suspensions. Figure 2B shows the results using C14-PEI as a control, with free mRNA set at 100%. The percentage of free mRNA increased as the amount of PEG-PLE increased. At PEG-PLE to C14-PEI mass ratios below w/w 0.3, mRNA encapsulation exceeded 90%. Specifically, at ratios of w/w 0.1 and w/w 0.2, the encapsulation efficiencies were 99% and 98%, respectively, comparable to the C14-PEI group. However, at a mass ratio of w/w 0.4, mRNA release began, with only 12% encapsulated. At w/w 0.5, the free mRNA increased to approximately 90%, indicating poor mRNA condensation. This reduced efficiency can be attributed to the competition with the negatively charged poly(l-glutamic acid) (PGA), which competes with mRNA for binding the positively charged PEI. Literature suggests that the stability of nanoplexes can be compromised by competing anions[196]. While the positive charge of polymers facilitates mRNA encapsulation through electrostatic interactions, strong polymer-mRNA binding can also impede mRNA release[197]. In this study, the nanoparticle formulations with intermediate negative-to-positive polymer w/w ratio demonstrated a balanced interaction between polymers and mRNA, allowing sufficient encapsulation and mRNA release in the presence of competing molecules at the same time.

Additionally, co-encapsulation of Cas9 mRNA and sgRNA was evaluated using electrophoretic mobility shift assays (EMSA). In this assay, negatively charged free RNA migrates through the agarose gel, while encapsulated RNA remains in the wells due to the larger size of the nanoparticles relative to the gel mesh size. Figure 2C illustrates that free Cas9 mRNA and sgRNA are present as bands at 4500 nt and 100 nt, respectively (lanes 2 and 3). Lane 4 shows the bands of a mixture of free Cas9 mRNA and sgRNA. In contrast, lane 5, containing PEG-PLE/C14-PEI at polymer w/w 0.2, displays no bands on the gel

but a bright signal around the wells, indicating encapsulation of both Cas9 mRNA and sgRNA within nanoparticles. Conversely, lane 6 shows two RNA bands for PEG-PLE/C14-PEI at polymer w/w 0.5, suggesting that neither Cas9 mRNA nor sgRNA was encapsulated, consistent with the results from the SYBR Gold assay.

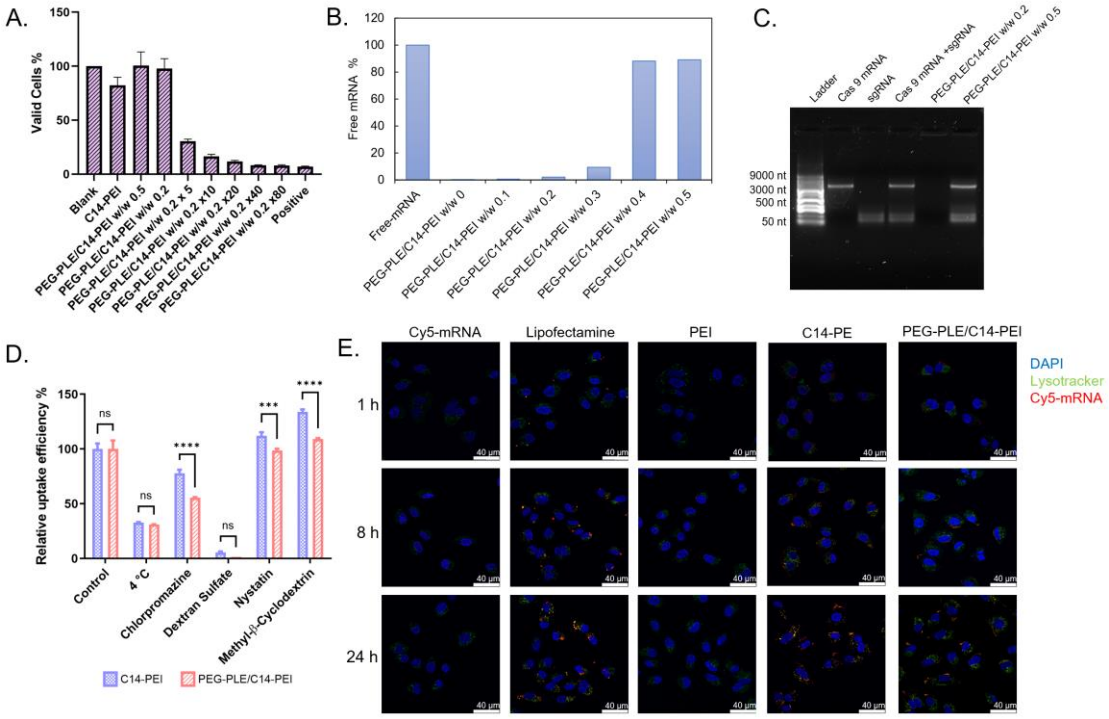

Figure 2. The assessment of RNA delivery with PEG-PEL/C14-PEI. A) the cytotoxicity tests of PEG-PLE/C14-PEI by CCK-8, results are showed with viable cells after 24h transfection in A549 cells (n=3). **B)** SYBR Gold assay to assess the encapsulation, results are shown as percent of free mRNA (n=3); **C)** Agarose gel shows the co-encapsulation of Cas9 mRNA and sgRNA with different formulations; **D)** the inhibition of cellular uptake pathways with C14-PEI and PEG-PLE/C14-PEI (***P≤0.0002, ****P≤0.0001); **E)** endosomal entrapment of different formulations imaged via CLSM.

5.4.4 Uptake pathway

The route of cellular uptake plays a crucial role in determining the intracellular processing and transfection efficiency of delivery systems. For instance, it has been established that lipoplexes are predominantly internalized via clathrin-mediated endocytosis, whereas polyplexes utilize both clathrin-mediated and caveolae-mediated endocytosis.[234,235] However, the caveolae-dependent route

appears to lead to more successful transfection,[234] as polyplexes and their payloads often undergo lysosomal degradation following clathrin-mediated entry. Furthermore, the internalization of nanoparticles is generally considered to be an energy-dependent endocytosis mechanism.[236,237] To elucidate the uptake pathway of PEG-PLE/C14-PEI nanoparticles, we performed a cellular uptake experiment comparing PEG-PLE/C14-PEI with C14-PEI nanoplexes. Cells were incubated with various chemical uptake inhibitors, including nystatin, dextran sulfate, chlorpromazine, and methyl-β-cyclodextrin, along with a low-temperature (4 °C) inhibition group, prior to transfection. The samples were then processed and analyzed using flow cytometry. Each inhibitor targets different pathways: nystatin inhibits caveolae and lipid raft-mediated endocytosis by depleting cholesterol from the cell membrane;[238] dextran sulfate inhibits scavenger receptor-mediated endocytosis;[237] chlorpromazine disrupts clathrin-coated pit formation by causing clathrin to translocate from the plasma membrane to intracellular vesicles;[239] and methyl-β-cyclodextrin inhibits cholesterol-dependent endocytosis by depleting membrane cholesterol[240]. The cellular uptake data, expressed as a percentage of mean fluorescence intensity (MFI) relative to uninhibited samples, provided insight into the primary uptake pathways of these nanoparticles.

The low-temperature group and dextran sulfate treatments significantly inhibited nanoplex uptake, reducing cellular uptake by approximately 70% and 90%, respectively, for both C14-PEI and PEG-PLE/C14-PEI formulations (Figure 2D). This indicates that both formulations predominantly rely on energy-dependent endocytosis and scavenger receptor-mediated pathways. Notably, there was no significant difference in uptake between the two formulations under these conditions, suggesting that energy-dependent endocytosis and scavenger receptor-mediated internalization are equally important for both nanoparticle types. Given the strong inhibitory effects of dextran sulfate, it is likely that polyplexes with higher lipid content, such as PEG-PLE/C14-PEI, share similarities with lipoplexes regarding their uptake route. Indeed, lipid nanoparticles are often internalized via scavenger receptor-mediated uptake.[241,242] The remaining uptake after treatment with nystatin, chlorpromazine, and methyl-β-cyclodextrin was 112.09%, 77.89%, and 133.97%

for C14-PEI, and 98.74%, 55.65%, and 109.20% for PEG-PLE/C14-PEI, respectively, compared to uninhibited conditions (Figure 2D). These results suggest that neither formulation primarily relies on caveolae-mediated or cholesterol-dependent endocytosis. Instead, they are only partially dependent on clathrin-mediated endocytosis. Recent studies have shown that while lipoplexes are taken up via clathrin-mediated endocytosis, PEI polyplexes lose transfection efficiency if caveolae-mediated endocytosis is blocked[234]. Furthermore, amphiphilic polyplexes have been found to depend on both clathrin-mediated endocytosis and fusogenic uptake mechanisms. These findings collectively suggest that PEG-PLE/C14-PEI nanoparticles utilize a complex uptake mechanism, with a potential preference for pathways that avoid lysosomal degradation, thereby enhancing transfection efficiency.[194]

5.4.5 Endosomal Entrapment

Through our cellular uptake experiments, we confirmed that the internalization of nanoparticles via the endocytic pathway is consistent with previous reports[199]. During this process, nanoparticles are typically trapped within endosomes and eventually degraded by lysosomal enzymes. To ensure effective biological effects, it is essential for these nanoparticles to escape from lysosomes and deliver their therapeutic payloads to the cytosol[94]. To visualize endosomal entrapment and the subsequent escape of nanoparticles within cells, we transfected A549 cells with Cy-5 labeled mRNA. We used LysoTracker Green DND-26, a fluorescent dye that specifically stains acidic compartments such as lysosomes, and DAPI to stain the cell nuclei. Confocal laser scanning microscopy (CLSM) was employed to co-locate the mRNA with the lysosomes, allowing for detailed imaging of the intracellular distribution and release dynamics of the nanoparticles. The study compared the C14-PEI and PEG-PLE/C14-PEI formulations, with PEI and Lipofectamine 2000 serving as controls. In the microscopy images (Figure 2E), the blue areas represent cell nuclei stained with DAPI, red dots indicate the presence of Cy-5 labeled mRNA, green regions correspond to lysosomes stained by LysoTracker, while yellow dots signify mRNA that is co-localized within lysosomes. In the control groups of free mRNA and PEI-transfected cells, there were no red dots and only a few

green dots, indicating that the mRNA did not successfully transfer into the cytoplasm. In contrast, the Lipofectamine 2000 group exhibited a punctate distribution of Cy-5 labeled mRNA (red) as early as 1 hour after transfection, along with the formation of acidic lysosomes (green dots). The signal intensity increased over time, with maximum mRNA uptake observed at 24 h.

For the C14-PEI and PEG-PLE/C14-PEI formulations, red dots were clearly visible on the cell membrane surfaces within 1 hour, indicating the initiation of internalization. After 8 h, numerous acidic lysosomes had formed, and significant co-localization (yellow dots) with the mRNA presented. Maximum uptake was observed after 24 h for both formulations. While yellow dots persisted after 24 h, signifying partial entrapment within endosomes, a substantial portion of the mRNA managed to escape and disperse into the cytoplasm. Notably, compared to C14-PEI, the PEG-PLE/C14-PEI formulation displayed more red dots and fewer yellow dots after 24 h, suggesting a higher efficiency in endosomal escape. One commonly proposed mechanism for the endosomal escape of polyplexes is the "proton sponge effect".[243] According to this hypothesis, once inside the acidifying environment of endosomes or lysosomes, materials containing amine groups can sequester endosomal protons, thereby slowing the pH drop. As a result, cells pump additional protons into the endosomes to reach the target pH, leading to an influx of counterions and an increase in osmotic pressure within the endosomes. This heightened pressure can cause the endosomal membrane to rupture, facilitating the escape of the delivery system into the cytoplasm. However, emerging evidence suggests that the process of polyplex-mediated endosomal escape is more complex than just the proton sponge effect. For instance, it has been shown that introducing PEG to create long-circulating nanoparticles can inhibit endosomal escape.[243] Moreover, studies have highlighted that the fusion of hydrophobic nanoparticles with lysosomal or endosomal membranes occurs through a combination of hydrophobic interactions, pH-triggered responses, and membrane destabilization, enabling the release of cargo into the cytoplasm.[93,94] Hydrophobic or amphiphilic nanoparticles often interact more readily with these membranes, facilitating fusion by promoting closer contact between the hydrophobic parts of the particles and the membrane lipids.[244] This

interaction, driven by direct electrostatic forces with negatively charged membrane components or the insertion of hydrophobic domains, can destabilize the membrane, allowing cargo or nanoparticles to escape. Additionally, certain nanoparticles remain stable at neutral pH but become more hydrophobic or undergo charge alterations in acidic conditions, further promoting membrane fusion and escape.[95] Additionally, a report by Galliani et al. demonstrated that drugs delivered via anionic poly(lactic-co-glycolic) acid (PLGA) nanoparticles exhibited a lower degree of co-localization with lysosomes after 2 h of incubation, which was attributed to a burst release mechanism.[245] These findings highlight the need for further research to fully understand the mechanisms behind endosomal escape and improve the design of nanoparticle-based delivery systems.[92]

5.4.6 Co-localization of Cas9 mRNA and sgRNA

Co-delivering Cas9 mRNA and sgRNA presents a significant challenge, primarily due to the risk of sgRNA degradation before it can effectively pair with the Cas9 protein. To ensure sufficient sgRNA is available for the formation of RNPs, strategies such as increasing sgRNA quantity and enhancing its stability through modification have been employed.[100,246] To better understand the intracellular distribution, kinetics, and behavior of Cas9 mRNA and sgRNA, we developed a fluorescence labeling-based method for tracking these molecules using confocal microscopy. Cas9 mRNA was synthesized via *in vitro* transcription using Cy5-UTP, while sgRNA sourced from Sigma-Aldrich, was labeled with pCp-AF488 (Jena Bioscience, Germany). These labeled RNAs were co-delivered to A549 cells using PEG-PLE/C14-PEI at polymer weight ratios (w/w) of 0.2 and 0.5, with C14-PEI and Lipofectamine 2000 serving as comparison controls. Fluorescence images were captured at various time points: 1, 4, 8, 24, 32, 48, and 72 h, allowing us to estimate the relative duration and degradation of the RNAs by measuring fluorescence intensity.

As illustrated in Figure 3A, C14-PEI, Lipofectamine 2000, and PEG-PLE/C14-PEI demonstrated distinct behaviors and distribution patterns over 72 h. Both C14-PEI and Lipofectamine 2000 showed high levels of co-localization of Cas9

mRNA and sgRNA, with Lipofectamine 2000, in particular, forming larger, more enriched complexes. This is likely due to Lipofectamine 2000's mechanism of action, where nucleic acids are encapsulated in lipoplexes, facilitating their uptake via clathrin-mediated endocytosis and resulting in enriched vesicular distribution. In contrast, C14-PEI quickly released the RNAs, leading to a more homogeneous distribution within cytoplasmic compartments. However, as Figure 3B shows, this formulation provided less protection for the RNAs, resulting in faster degradation and a shorter intracellular lifespan. Interestingly, the PEG-PLE/C14-PEI formulation exhibited a delayed yet more efficient RNA distribution. In Figure 3B, the signal accumulation of PEG-PLE/C14-PEI formulation kept a high level after 24 h, with Cas9 mRNA and sgRNA displaying distinct distribution patterns and lower co-localization in Figure 3C. Cy5-labeled Cas9 mRNA initially concentrated on the cell surface before gradually dispersing into the cytoplasm, while AF488-labeled sgRNA quickly localized to the cytoplasm and subsequently migrated into the nucleus over time (Figure 3A). This distribution aligns with the expected mechanism, where Cas9 mRNA is translated into Cas9 protein in the cytoplasm, which then interacts with sgRNA within the nucleus[23].

In summary, the PEG-PLE/C14-PEI formulation not only facilitated a more efficient distribution of Cas9 mRNA and sgRNA but also extended their intracellular persistence. This prolonged presence resulted in higher expression levels and greater gene-editing efficiency compared to C14-PEI.

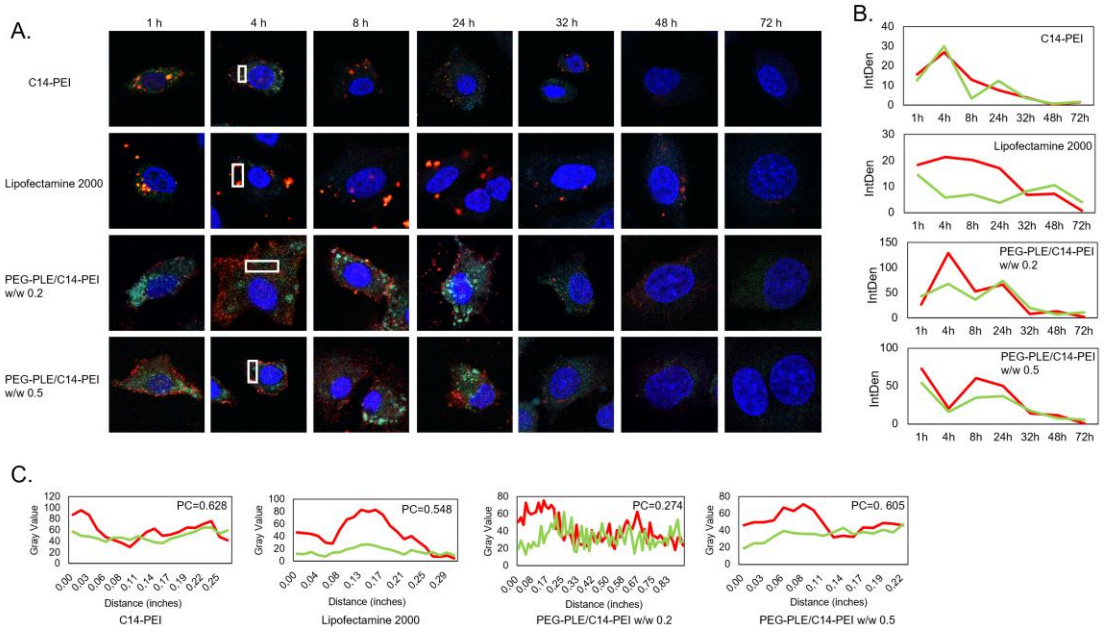

Figure 3. Co-localization of Cas9 mRNA and sgRNA. A) The images of different formulations in 72h post transfection, captured by CLSM; **B)** integrated density of Cy5-mRNA and AF88-sgRNA related to Figure A in 72h, density was assessed by ImageJ; **C)** plot profile of ROIs of Figure A at 4h post transfection, co-localization is analyzed by Pearson's correlation coefficient (PC).

5.4.7 Luciferase mRNA expression

To evaluate the mRNA expression efficiency of the PEG-PLE/C14-PEI formulation, luciferase mRNA (Fluc mRNA) was transfected into A549 cells at various mass ratios of PEG-PLE to C14-PEI: 0, 0.1, 0.2, 0.3, 0.4, and 0.5. For comparison, PEI and C14-PEI formulations were used as controls. Following transfection, relative luminescence units (RLU) were measured with a plate reader (TECAN). As shown in Figure 4A, all PEG-PLE/C14-PEI groups successfully induced luciferase expression. Notably, the inclusion of PEG-PLE in the C14-PEI nanoparticles significantly enhanced luciferase expression levels. The highest RLU was observed in the 0.3 w/w PEG-PLE group, representing a 385-fold increase compared to the blank control. Interestingly, mRNA expression did not increase linearly with the amount of PEG-PLE. At higher PEG-PLE ratios, the luciferase signals decreased, with the 0.5 w/w group showing around a 300-fold increase in RLU. The enhanced mRNA expression observed with the PEG-PLE/C14-PEI formulation is likely due to improved endosomal escape, as evidenced by the expression profile across

different PEG-PLE ratios, which aligns with encapsulation test results. In conclusion, the PEG-PLE/C14-PEI formulations demonstrated more efficient endosomal escape and higher mRNA expression compared to the C14-PEI formulation.

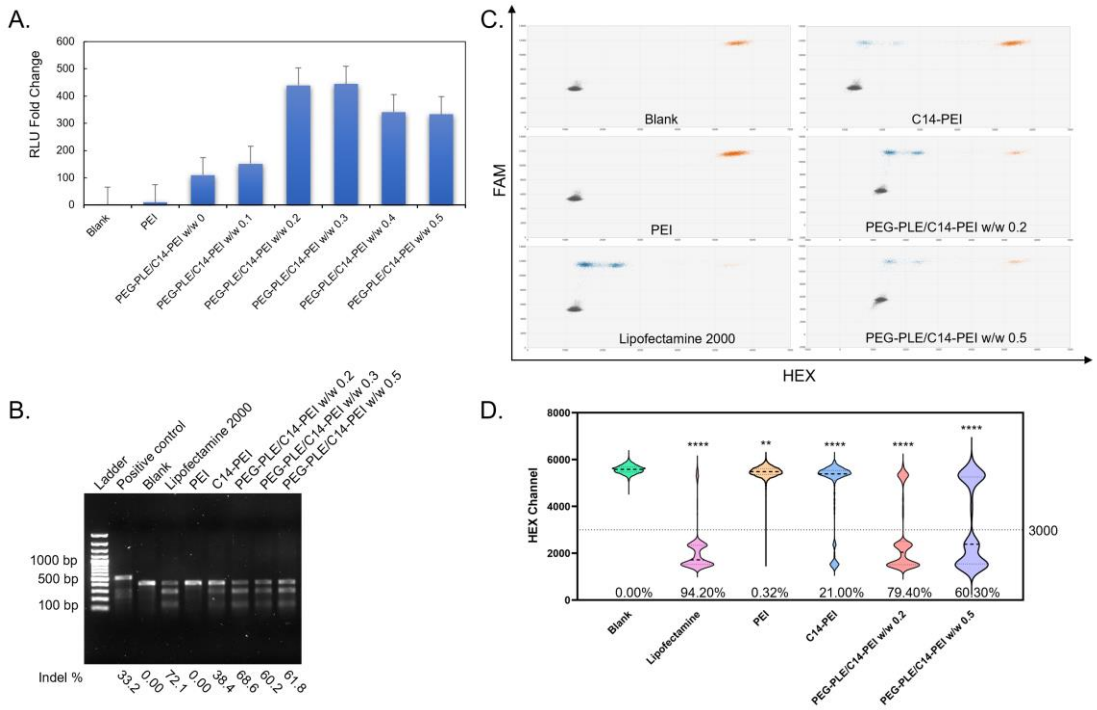

Figure 4. Fluc mRNA expression and gene editing efficiency. A) RLU fold change after PEG-PLE/C14-PEI transfection 24h, normalized by the blank; **B)** T7EI cleavage tests in agarose gel; edited efficiency is labeled below the image; **C)** Droplet distribution of ddPCR, X-axis is HEX channel, Y-axis is FAM channel, Gray dots designate the FAM-negative/HEX-negative group, orange dots represent the FAM-positive/HEX-positive group, blue dots are the FAM-positive/HEX-negative group; **D)** Violin plots of HEX channel (excludes FAM negative droplets) of ddPCR (**P≤0.0021, ****P≤0.0001); intensity at 3000 is set as threshold, and edited efficiency is labeled below the plots.

5.4.8 T7EI assay

To further assess the capability of the PEG-PLE/C14-PEI formulation to co-deliver Cas9 mRNA and sgRNA and facilitate gene editing, we transfected A549 cells, a cell line known to harbor *KRAS* G12S mutations,[202] with Cas9 mRNA and sgRNA specifically targeting the *KRAS* G12S allele. The gene editing efficiency was then evaluated using PEG-PLE/C14-PEI nanoparticles. As described previously, non-homologous end joining (NHEJ) is the primary

mechanism for CRISPR-Cas9-mediated gene knockout, often resulting in insertions and/or deletions (indels) in the DNA strand.[206] T7 Endonuclease I, a structure-selective enzyme, recognizes these indel sites on the DNA sequence and cleaves them into two fragments.[205] The resulting digestion products can be visualized and analyzed through agarose gel electrophoresis. C14-PEI and PEG-PLE/C14-PEI formulations at w/w of 0.2 and 0.5 were transfected into A549 cells for 48 h. PEI and Lipofectamine 2000 were used as controls. As shown in the gel imaging (Figure 4B), samples treated with C14-PEI and PEG-PLE/C14-PEI nanoparticles demonstrated efficient gene editing after 48 h. The blank control, which received no treatment, showed only a single band corresponding to the target sequence, indicating no editing. The PEI control exhibited a similar result, confirming the absence of gene editing, likely due to the inability of mRNA to enter the cells, as corroborated by CLSM. In contrast, the Lipofectamine 2000-treated sample displayed both the original band and two cleaved bands, indicating a successful gene editing event with an indel percentage of 72.1%. This highlights the necessity of an appropriate delivery system for effective gene editing. Similarly, C14-PEI and PEG-PLE/C14-PEI at w/w ratios of 0.2 and 0.5 achieved average indel rates of 38.4%, 68.6%, and 60.2%, respectively. Notably, the PEG-PLE/C14-PEI formulation demonstrated higher gene editing efficiency than the C14-PEI group, consistent with its superior endosomal escape and increased luciferase expression observed in earlier experiments.

5.4.9 Droplet Digital PCR

The T7 Endonuclease I (T7EI) assay, while useful for detecting indels, is semi-quantitative, has limited sensitivity, and is prone to false positives. It also suffers from high background signals when sequence polymorphisms are present.[205] To overcome these limitations, we employed droplet digital PCR (ddPCR) to more accurately assess the deletion of *KRAS* G12S alleles in A549 cells. In ddPCR, two specific probes within a single amplicon are used to detect NHEJ-mediated events.[185,204] The first probe, labeled with FAM, serves as a reference and is located away from the mutagenesis site, counting all genomic copies of the target. The second probe, labeled with HEX, is positioned at the site of

nuclease-induced cuts or nicks in the DNA. If NHEJ occurs, the HEX probe loses its binding site, resulting in the loss of the HEX signal, leaving only the FAM signal from the reference probe. To perform the ddPCR assay, genomic DNA was isolated from transfected cells 48 h post-transfection. The DNA was then subjected to droplet generation, PCR amplification, and fluorescence analysis.

As shown in Figure 4C, droplets that were positive for both FAM and HEX (orange group) represent unedited DNA copies, while droplets positive for FAM but negative for HEX (blue group) represent edited DNA copies. Consistent with the T7EI assay results, no edited events were detected in the blank and PEI control groups. However, in the Lipofectamine 2000 group, 3017 positive droplets were observed, compared to 573 in the C14-PEI group, and 1768 and 617 edited events in the PEG-PLE/C14-PEI groups with w/w ratios of 0.2 and 0.5, respectively. Subsequently, we calculated the percentage of edited gene copies among the total events. As shown in Figure 4D, the gene editing efficiency of Lipofectamine 2000 reached 94.2%, while C14-PEI achieved 21%. Notably, the PEG-PLE/C14-PEI formulation outperformed C14-PEI, with editing efficiencies of 79.4% and 60.3% in the w/w 0.2 and w/w 0.5 groups, respectively.

5.4.10 Sanger Sequencing

To further validate the gene editing efficacy of the PEG-PLE/C14-PEI formulation, we performed Sanger sequencing on the PCR products from PEG-PLE/C14-PEI treated A549 cells. The sequencing data was analyzed using the ICE CRISPR analysis tool,[186] confirming that the *KRAS* G12S allele had been successfully edited by the PEG-PLE/C14-PEI system (Figures 5A and 5D). Indels were detected around the protospacer adjacent motif (PAM) sequence (TGG) in the DNA backbone, indicating successful gene editing. The *KRAS* G12S editing efficiency showed a strong correlation (R^2 = 0.98) based on sequence alignment (Figure 5B). Overall, the analysis revealed that 69% of the sequences contained indels of varying sizes, while 29% exhibited base alterations. Among the detected indels, a 1 bp insertion was the most common, accounting for 37% of the total, which is consistent with findings by Gao and

colleagues[202]. This was followed by a -10 bp deletion (15%) and other indels (17%), aligning with the expected outcomes of NHEJ-mediated knockouts. The presence of these deletions can induce frameshift mutations within the *KRAS* gene, potentially leading to the functional inactivation of the mutant *KRAS* protein. The indels detected near the PAM sequence confirm the precision and efficiency of the PEG-PLE/C14-PEI delivery system in targeting *KRAS* G12S alleles, highlighting its potential for effective gene editing.

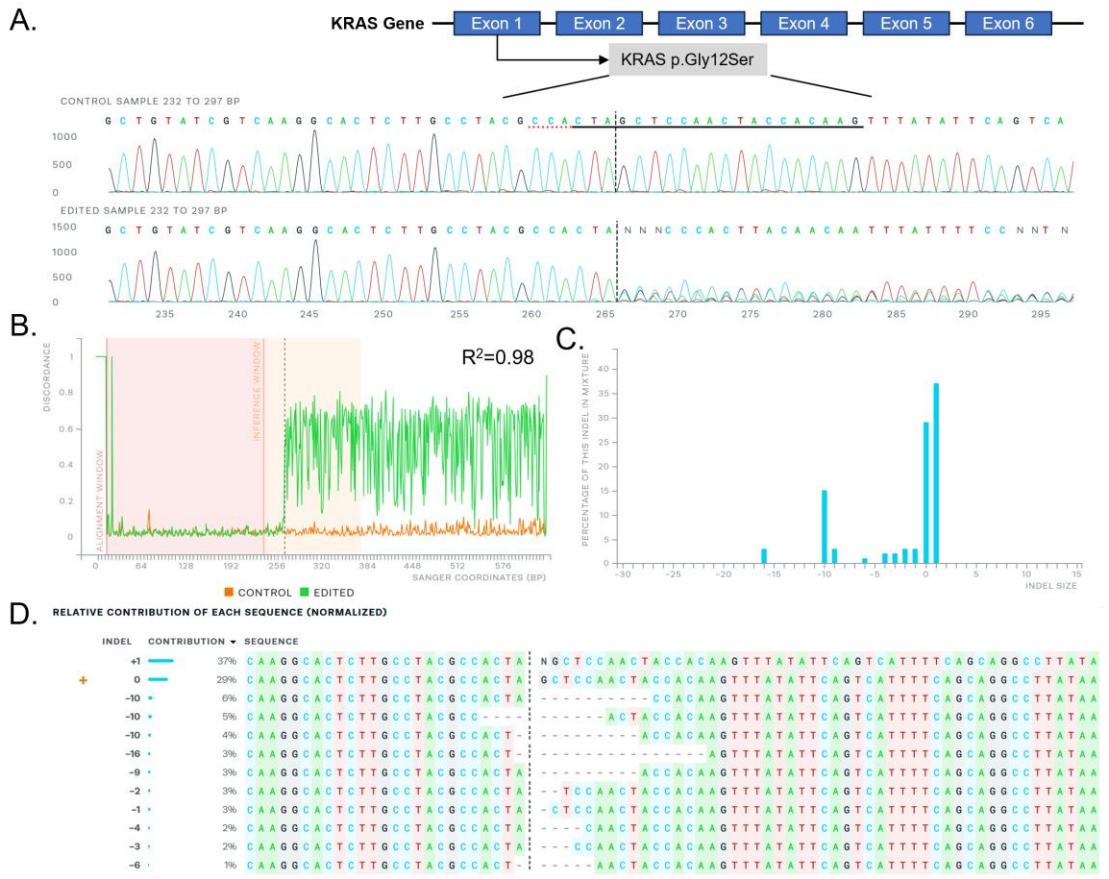

Figure 5. Sanger sequencing after PEG-PLE/C14-PEI w/w 0.2 treatment in A549 cells analyzed by the ICE CRISPR analysis tool. A) *KRAS* exon map (up), and edited sequence (reverse strand, down) illustrate; **B）** alignment of Sanger sequencing; **C）** distribution of indel sizes; **D）** contribution of each sequence after gene editing.

5.4.11 Western Blot

KRAS plays a crucial role in activating downstream effector molecules, including those in the MAPK and AKT-mTOR signaling pathways, which are essential for cell proliferation and survival.[208] Therefore, assessing the protein

levels in these downstream pathways after gene editing is critical. We performed a Western blot analysis to evaluate the expression of downstream proteins following the knockout of the *KRAS* G12S allele. Given that mutant *KRAS* leads to the continuous activation of downstream signaling, particularly resulting in the phosphorylation of ERK, we focused on analyzing both total ERK and phosphorylated ERK (pERK) levels. Lipofectamine 2000 and PEI were used as controls for comparison. In the experiment, 100,000 A549 cells were seeded in a 6-well plate 24 h before transfection with PEG-PLE/C14-PEI. After 48 h, total protein was extracted from the cells and analyzed by Western blotting. As shown in Figure 6A, the total ERK levels remained consistent across all groups, indicating that the overall expression of ERK was not affected by the treatments. However, a significant downregulation of pERK was observed in the groups treated with Lipofectamine 2000 and PEG-PLE/C14-PEI, suggesting effective inhibition of downstream signaling following *KRAS* G12S knockout. In contrast, the C14-PEI formulation did not mediate a similar downregulation of pERK, possibly due to functional compensation by the cells, where protein translation does not always correlate directly with gene editing efficiency[211]. This could explain why the C14-PEI formulation was less effective in downregulating pERK despite successful gene editing.

5.4.12 Cell Migration

Activating mutations in *KRAS* lead to impaired GTP hydrolysis or enhanced nucleotide exchange, resulting in continuous downstream signaling that drives sustained cell proliferation. This signaling is closely related to the migration and invasion of cancer cells[207,208]. Therefore, knocking out mutant *KRAS* is expected to inhibit cancer cell migration. To evaluate the impact of *KRAS* gene editing on cell migration, we conducted a wound healing assay using a cell culture dish with a 2-well insert from ibidi (Germany). A549 cells were seeded into the insert chambers 24 h before transfection. The insert was removed once the cells reached 100% confluence. Following nanoparticle transfection, cell migration was assessed by measuring the gap area between the two cell groups from time 0 h to 24 h using ImageJ. As shown in Figures 6B and 6C, cells in the treated groups exhibited slower migration compared to the blank

control group. At 8 h, the blank group had covered approximately 50% of the wound area, while the PEG-PLE/C14-PEI w/w 0.2 group covered around 35%, and the PEG-PLE/C14-PEI w/w 0.5 group covered nearly 30%. By 24 h, the wound was completely closed in the blank group, whereas the PEG-PLE/C14-PEI w/w 0.2 and w/w 0.5 groups showed 83% and 94% wound coverage, respectively. The C14-PEI group, consistent with Western blot findings, displayed less impact on cell migration compared to the PEG-PLE/C14-PEI formulations, further demonstrating the superior efficacy of the PEG-PLE/C14-PEI system in inhibiting cell migration.

5.4.13 Cell Apoptosis

Cell apoptosis is a crucial indicator for evaluating the effectiveness of *KRAS* mutation excision following CRISPR-Cas9 treatment, as KRAS is integral to cell proliferation. To investigate whether *KRAS* mutant deletion induces apoptosis in cancer cells, we assessed the percentage of apoptotic cells using flow cytometry with an Annexin V-AF488/propidium iodide (PI) double-staining assay.[189] The assay was conducted on A549 cells treated with PEG-PLE/C14-PEI formulations at w/w ratios of 0.2 and 0.5, with C14-PEI, Lipofectamine 2000, and PEI used as controls. The representative flow cytometry data are shown in Figure 6D. After 48 h post-transfection, the Lipofectamine 2000 group exhibited the highest percentage of apoptotic cells at 33.00%. The C14-PEI group showed a slightly lower apoptosis rate at around 28.00%. In contrast, the PEI group demonstrated only 11.95% apoptosis, indicating minimal gene editing effects. The PEG-PLE/C14-PEI groups showed 31.8% and 26.4% apoptotic cells for the w/w 0.2 and w/w 0.5 formulations, respectively. These results reflect a significant increase in apoptosis compared to the blank and PEI groups. Notably, the PEG-PLE/C14-PEI w/w 0.2 formulation achieved apoptosis levels comparable to Lipofectamine 2000, demonstrating its effectiveness in inducing cell apoptosis through *KRAS* mutant excision.

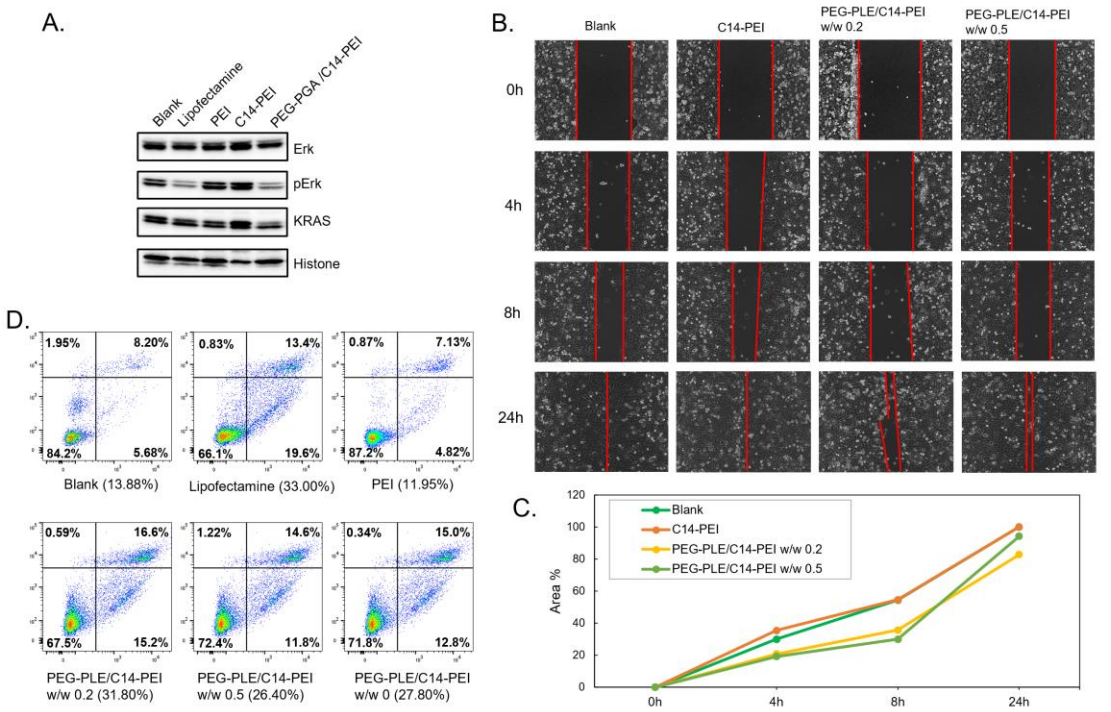

Figure 6. Cell capability assessment after the transfection of PEG-PLE/C14-PEI nanoplexes. A) Western blot after 48h transfection in A549 cells; **B）** images of A549 cells in the wound healing assay 48h after transfection; **C） the** percentage of covered area in wound healing assay; **D）** cell apoptosis after 48h transfection in A549 cells, X-axis shows the intensity of Annexin V-AF488, and Y-axis shows the intensity of PI.

5.5 Conclusion

In our previous report (Chapter I), we demonstrated that C14-PEI nanoplexes effectively delivered Cas9 mRNA and sgRNA into A549 cells, despite their large size and highly positive zeta potential, which might trigger immune responses and reduce *in vivo* efficiency. In this study, we explored the use of methoxy-poly(ethylene glycol)-block-poly(l-glutamic acid sodium salt) (PEG-b-PLE) to address these issues by shielding the positive charges of C14-PEI formulations, aiming to enhance the nanoparticles' properties and delivery efficiency. We prepared PEG-PLE/C14-PEI nanoparticles by blending PEG-PLE into the RNA solution, varying the w/w ratios of PEG-PLE to C14-PEI from 0 to 4. Characterization through DLS and LDA revealed that PEG-PLE significantly reduced the nanoparticle size from approximately 330 nm to around 140 nm, as confirmed by NTA. The zeta potential also decreased from nearly 40 mV to

a slight negative charge range of -1.0 mV to -14 mV. Among the formulations, PEG-PLE/C14-PEI at a polymer w/w ratio of 0.2 exhibited optimal properties, including low toxicity, high encapsulation efficiency, and effective mRNA delivery. Confocal microscopy imaging showed that PEG-PLE/C14-PEI efficiently escaped from endosomes and distributed Cas9 mRNA and sgRNA within cells. Uptake pathway inhibition tests indicated that PEG-PLE/C14-PEI internalization primarily relies on scavenger receptors and clathrin-mediated endocytosis. Notably, the PEG-PLE/C14-PEI w/w 0.2 formulation achieved the highest gene editing efficiency for *KRAS* G12S deletion in A549 cells, with 68.6% indels detected by T7EI and 79.4% edited signals observed by ddPCR. Sanger sequencing confirmed *KRAS* G12S deletion with 69% of indels and 29% of base alterations. Following *KRAS* G12S deletion, Western blot analysis showed reduced levels of phosphorylated ERK, and approximately 32% of apoptotic cells were observed in PEG-PLE/C14-PEI w/w 0.2-treated cells. Additionally, cell migration was significantly decreased after treatment with the PEG-PLE/C14-PEI formulation. These findings demonstrate that PEG-PLE, as a negatively charged polymer, effectively enhances polycationic nanoplex properties, increases mRNA expression, and improves gene editing efficiency by providing surface adsorption and charge shielding. Future studies will determine *in vivo* gene editing in lung cancer.

5.6 Supplementary Information

A.

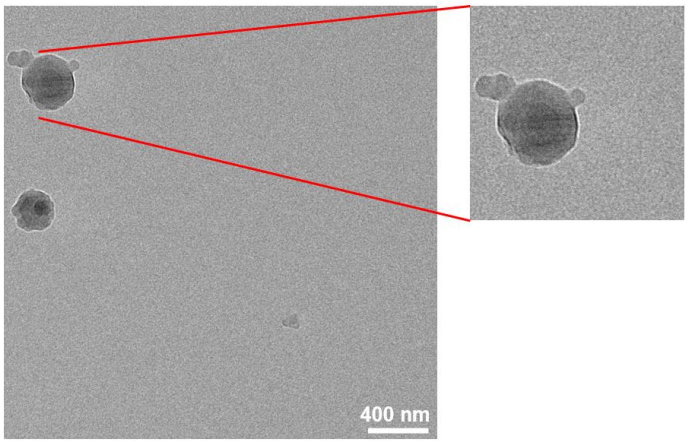

Figure S. A. Cryo-EM image of C14-PEI nanoparticles.

5.7 Acknowledgements

The author Siyu Chen acknowledges the financial support from the China Scholarship Council. Simone Carneiro thanks the financial support from the Alexander von Humboldt Foundation and the Center of Nanoscience (CeNS) Munich. This research was also supported by ERC-2014-StG-637830 to Olivia Merkel. Thanks to Prof. Roland Beckmann and Dr. Otto Berninghausen for the technical support with Cryo-EM.

6. Chapter III

Engineered-Affibody Conjugates Contribute to The Specific Targeting and Cellular Retention of Polyplexes in Erbb3 Overexpressed Lung Cancer Cells

Siyu Chen[1], Aditi Mehta[1], Sahana Sheshachala[2], Simone P. Carneiro[1], Olivia M. Merkel[1]

[1]Ludwig-Maximilians-University, Department of Pharmacy, Pharmaceutical Technology and Biopharmaceutics, Butenandtstraße 5-13, Munich, 81377, Germany

[2] NanoTemper Technologies GmbH, Steinerstraße 11, Munich, 81379, Germany.

The manuscript is in preparation.

6.1 Abstract

Ligand-modified nanoparticles have shown the ability to specifically bind to tumor cells, improving retention in tumors after initial accumulation driven by the enhanced permeability and retention effect. These particles are typically engineered to bind to receptors overexpressed in cancer cells compared to healthy cells, such as the Erbb3 receptor in lung cancer. In this study, we confirmed the overexpression of Erbb3 in various *KRAS* mutant lung cancer cell lines. An engineered affibody, well-established in previous research, was selected to target Erbb3 as a proof of concept. The affibody was conjugated to PEI or C14-PEI using SPDP as a linker, for forming different polyplex formulations, namely mRNA complexes with PEI-affibody, C14-PEI/PEI-affibody, and C14-PEI/C14-PEI-affibody. These formulations were prepared at various weight/weight ratios and characterized in terms of particle size, polydispersity index (PDI), and zeta potential. We also evaluated cellular uptake

and eGFP mRNA expression to understand how the different formulations and conjugates influenced ligand-modified polyplex properties and delivery behavior. Our results demonstrated that affibody conjugates can specifically target Erbb3 and promote polyplex accumulation in *KRAS*-mutated lung cancer cells. We further analyzed the impact of conjugation methods and affibody density on polyplex design and performance. Finally, a spectral shift technique was used to assess the affinity of the affibody, affibody conjugates, and their polyplexes towards Erbb3, allowing us to estimate dissociation constants (Kd) and evaluate performance across different formulations. In conclusion, this study highlights the advantages of using specific targeting ligands. By optimizing formulation components, conjugation methods, and ligand density, various targeting ligands can be attached to polyplexes, enhancing cell-specific targeting, internalization, and retention. These findings provide valuable insights and a foundation for future targeted therapies and polyplex design.

6.2 Introduction

Lung cancer is a malignant tumor that originates in the lung. According to the Global Cancer Statistics 2022, it remains the most commonly diagnosed cancer and the leading cause of cancer-related deaths.[1] The disease typically arises from genetic damage to the DNA of airway cells, often linked to cigarette smoking or inhalation of harmful chemicals.[247] Lung cancer is also influenced by geography, ethnicity, gender, and socioeconomic factors. As a heterogeneous disease, it encompasses different subtypes, each requiring tailored treatments.[248] In addition to traditional methods such as surgery, radiotherapy, and chemotherapy, targeted therapies and immunotherapies have been introduced in clinical settings.[249] However, survival rates remain low, especially in metastatic cases, with challenges such as drug resistance and systemic toxicity still persisting.

Nanomedicine, a rapidly growing field, offers promising solutions to these biological challenges. Numerous nanoparticle-based therapies have been studied to treat cancer,[250] neurodegenerative diseases,[251] and infections.[252] Nanoparticles (NPs), due to their unique properties, present new opportunities

for targeted lung cancer therapy.[253] As drug carriers, NPs enhance targeting accuracy, and drug stability, and increase drug accumulation in tumor tissues, leading to improved anti-tumor effects.[254] Various forms of NPs have been explored, including lipid nanoparticles (LNPs),[255] polyplexes,[183] gold NPs,[217] endosomal vesicles,[256] and peptide NPs.[47] The success of mRNA vaccines for COVID-19 has further propelled the field of mRNA therapeutics, establishing it as a viable treatment option in modern medicine.[71] In our previous study (Chapter I), we reported on a cationic polymer, C14-PEI, which demonstrated low toxicity and effective mRNA delivery to lung cancer cells.

Recent studies have shown that targeted nanoparticles can specifically bind to tumor cells, enhancing their retention within tumors following initial accumulation due to the enhanced permeability and retention (EPR) effect.[257] The EPR effect refers to a universal pathophysiological phenomenon and mechanism in which macromolecular compounds such as albumin and other ligand-conjugated drugs beyond certain sizes (typically liposomes, nanoparticles, and macromolecular drugs) can progressively accumulate in the tumor vascularized area and thus achieve targeting delivery and retention of anticancer compounds into solid tumor tissue.[258] Due to the lack of effective lymphatic drainage in tumor tissue, the synergistic effect of multiple growth factors and inflammatory factors (such as vascular endothelial growth factor, VEGF) leads to abnormal transport of macromolecular drugs in tumor tissue, thus causing the EPR effect.[259] The efficiency of the EPR effect can be enhanced by modifying the surface of NPs to optimize their size and surface charge. In particular, improving the NPs' affinity for tumor cells can lead to better targeting and accumulation within the tumor microenvironment, resulting in more effective therapeutic delivery. Designing NPs to target specific receptors may enhance retention in the tumor region and reduce off-target effects, a strategy that shows significant potential for future clinical applications. While well-known receptors such as *EGFR* have been extensively studied,[260] novel overexpressed receptors provide attractive targets for new nanotherapeutics. For instance, Gabold et al. recently used transferrin-modified chitosan nanoparticles for nose-to-brain delivery, demonstrating increased cellular uptake and faster passage through epithelial layers in glioblastoma models.[261]

One receptor gaining attention in cancer research is receptor tyrosine-protein kinase Erbb3, also known as HER3 (human epidermal growth factor receptor 3), which plays a key role in tumor progression and resistance to treatment.[262] Erbb3, a member of the type I RTK ERBB receptor family, shares a common structure with other ERBB receptors. It consists of an extracellular binding domain (ECD), an intracellular tyrosine kinase domain, and a C-terminal tail. The ECD is divided into four domains: domains I and III have β-helical structures that contain ligand-binding sites, while domains II and IV consist of seven small disulfide-containing modules forming a β-hairpin loop, facilitating interaction between domains II and IV.[263] Although the tyrosine kinase domain of Erbb3 is inactive, it forms active heterodimers with other members of the ErbB family. One of the most potent tumorigenic heterodimers is the HER2/HER3 pair, which activates key signaling pathways such as PI-3K/Akt and MAPK/MEK4.[262,264] Increased expression of Erbb3 is linked to various cancers,[265-269] including lung cancer, where its expression is notably higher in stage IA1 lung adenocarcinoma, particularly in cases without *EGFR* mutations.[267] Studies have shown that elevated Erbb3 levels are also associated with poor chemotherapy outcomes in both lung and breast cancers.[264] A promising therapeutic approach involves an engineered affibody targeting Erbb3, as reported by Schardt and colleagues.[270] This affibody specifically binds to Erbb3 without triggering downstream signaling, making it a valuable ligand for conjugation with polyplexes in targeting lung cancer cells.

This study utilized PEI and C14-PEI to explore affibody conjugation, polyplex preparation, and *in vitro* evaluation and further discussed the interaction between self-assembled nanoparticles decorated with an engineered affibody and overexpressed Erbb3 in *KRAS* mutant lung cancer cells. After the confirmation of the overexpression of Erbb3 in *KRAS*-mutant lung cancer cells, we employed the engineered affibody as a proof-of-concept targeting ligand due to its well-characterized ability to bind the Erbb3 receptor and then prepared polyplexes depending on the formulation, conjugation strategy, and affibody density. Following the characterization and assessment of particle size, PDI, zeta potential, cellular uptake, and gene expression, the spectral shift test was performed to explore the affinity and receptor binding behavior of affibody,

polymer conjugates, and polyplexes.

6.3 Materials & Methods

6.3.1 Materials

4-(2-hydroxyethyl)-1-piperazineethanesul-fonic acid (HEPES), Dulbecco's Phosphate Buffered Saline (PBS), 0.05% trypsin-EDTA, RPMI-1640, fetal bovine serum (FBS), bovine serum albumin (BSA), 1,2-epoxytetradecane, branched PEI 600 Da, Tris-buffered saline, Tween 20, Penicillin-Streptomycin solution, FluorSave Reagent, Lysogeny broth (LB), ampicillin, 6-diamidino-2-phenylindole dihydrochloride (DAPI), Brilliant Blue, sodium dihydrogenphosphat, isopropyl β-d-1-thiogalactopyranoside (IPTG), 2,4, 6-trinitrobenzene sulfonic acid (TNBS), sodium azide, paraformaldehyde (PFA), sodium chloride, imidazole, lysozyme, Benzonase® Nuclease were purchased from Sigma-Aldrich (Darmstadt, Germany). Dulbecco's Modified Eagle Medium (DMEM), Lipofectamine™ 2000, Pierce™ BCA Protein Assay kit, trypan blue, Novex™ WedgeWell™ 8-16% Tris-Glycin gel, Rhodamine-Phalloidin, AF488-conjugated goat anti-rabbit IgG (H+L) secondary antibody, HisPur™ Ni-NTA Spin Purification Kit, FITC Labeling Kit, Pierce Universal Nuclease, dithiothreitol (DTT), Succinimidyl 3-(2-pyridyldithio) propionate (SPDP), and PEG12-SPDP were bought from Thermo Fisher Scientific (Planegg, Germany). PEI 5kDa (Lupasol G100, BASF, Germany), eGFP mRNA (RiboPro, Netherlands), PE-labeled anti-Erbb3 antibody (Biolegend, USA), PE Mouse IgG2a $_{K}$ Isotype Control (Biolegend, USA), primary antibodies for Erbb3 (Cell Signaling Technology, MA, USA), Her3 (Erbb3, Sino biological, China), protein Labeling Kit RED-NHS 2_{nd} Generation (NanoTemper Technologies GmbH, Munich, Germany), and Vivaspin 6 centrifugal concentrator (Sartorius, Germany) were

purchased from the suppliers indicated. Cy5-mRNA, AF405-mRNA, Cy5-Her3, engineered trivalent affibody against Erbb3, and FITC-affibody were prepared and labeled in the laboratory. Methanol, ethanol, acetic acid, and acetone were provided by Ludwig-Maximilians-University Munich.

6.3.2 Cell Culture

A549, Hop-62, H358, and H358M cells were cultured in RPMI-1640 medium, while 16HBE14o- cells were grown in DMEM. Both media were supplemented with 10% heat-inactivated FBS and 1% penicillin-streptomycin. The cells were subcultured and maintained in a humidified incubator at 37°C with 5% CO_2.

6.3.3 Erbb3 Receptor Expression

UCSC Xena was used to cross-analyze clinical data from The Cancer Genome Atlas Program (TCGA) and The Genotype-Tissue Expression (GTEx) project to confirm Erbb3 expression in lung cancer patients.[271] To assess Erbb3 surface accessibility and density, flow cytometry (FACS) and immunofluorescence tests were performed on healthy lung cells (16HBE14o-, WT *KRAS*) and lung cancer cells (A549, *KRAS* G12S; Hop62, *KRAS* G12C).

For the FACS analysis, cells were cultured 24 h prior to staining. After washing with PBS and detaching with 0.05% trypsin-EDTA, cells were resuspended to approximately 1 x 10^6 cells/mL in cold PBS with 3% BSA and 1% sodium aside. Each sample was incubated with either PE-labeled anti-Erbb3 antibody or PE Mouse IgG2a κ Isotype Control (Biolegend, USA) at 4°C in the dark for 30 minutes. Cells were washed three times by centrifugation at 500 xg for 5 min, then resuspended in cold PBS with 3% BSA and 1% sodium aside for FACS analysis.

For immunofluorescence with confocal imaging, cells were seeded on coverslips in a 24-well plate and incubated for 24 h. After washing with PBS, cells were fixed with 4% PFA for 15 minutes and permeabilized with PBS

containing 0.3% Tween-20 for 10 min. Blocking was done with 5% BSA in TBST for 1 h. Primary anti-Erbb3 antibody (Cell signaling, USA) was incubated with the cells at 4°C overnight, followed by incubation with an AF488-conjugated secondary antibody (Thermo Fisher, USA) for 1 hour at room temperature in the dark. After staining F-actin with Rhodamine-Phalloidin (Thermo Fisher, USA) and the nucleus with DAPI (Sigma-Aldrich, Germany), the coverslips were mounted on slides using FluorSave Reagent (Sigma-Aldrich, Germany). Confocal images were captured using the blue channel (350/470 nm) for DAPI, the green channel (490/517 nm) for AF488, and the red-orange channel (540/565 nm) for Rhodamine-Phalloidin on a confocal microscopy (Leica SP8 inverted, software: LAS X, Leica Microsystems GmbH, Germany).

6.3.4 Affibody Expression

The E. coli BL21 strain containing Affibody-His-tag plasmids was cultured from glycerol stock in 5 mL of LB with 100 µg/mL ampicillin at 37°C, shaking at 110 rpm, until the culture became turbid. This bacterial culture was then transferred to 200 mL of LB media with 100 µg/mL ampicillin and incubated overnight at 37°C, shaking at 220 rpm, until the optical density (OD600) reached 0.4-0.8. Protein expression was induced by adding IPTG to a final concentration of 1 µM, followed by incubation at 30°C while shaking at 220 rpm for 4 hours. The bacterial cell pellet was then collected by centrifugation at 4000 xg for 30 min. Affibody extraction was carried out using the HisPur™ Ni-NTA Spin Purification Kit (Thermo Fisher, USA) according to the manufacturer's instructions with an adjustment. Generally, the bacterial pellet was resuspended in 1.4 mL of lysis buffer (50 mM NaH_2PO_4, 300 mM NaCl, 10 mM imidazole, pH 8.0) and treated with lysozyme (Sigma-Aldrich, Germany), Benzonase® Nuclease (Sigma-Aldrich, Germany), and Pierce Universal Nuclease (ThermoFisher, USA) to lyse the bacterial cells and remove nucleic acids, followed by 30 min of incubation on ice. The lysate was then applied to equilibrated HisPur™ Ni-NTA columns and allowed to bind to the resin at 4°C for 30 min. After three washes with wash buffer (50 mM NaH_2PO_4, 300 mM NaCl, 20 mM imidazole, pH 8.0), the affibody was eluted using elution buffer (50 mM NaH_2PO_4, 300 mM NaCl, 500 mM

imidazole, pH 8.0) and stored at -80°C in the presence of 5 mM DTT.

6.3.5 Affibody Quantification and Qualification

The concentration of the purified affibody was determined using a bicinchoninic acid (BCA) assay, and its purity and integrity were assessed via sodium dodecyl sulfate-polyacrylamide gel electrophoresis (SDS-PAGE). The Pierce™ BCA Protein Assay Kit (Thermo Fisher, USA) was performed according to the manufacturer's instructions. A BSA standard curve was prepared by diluting BSA in water across six concentrations, ranging from 2 mg/mL to 0.0625 mg/mL. The BCA working reagent was obtained by mixing 50 parts of reagent A with 1 part of reagent B. For the assay, 20 µL of each BSA dilution or sample was combined with 200 µL of BCA working reagent in a 96-well plate and incubated at 37°C for 30 minutes, protected from light. Absorbance at 562 nm was measured using a Tecan plate reader, with the blank standard absorbance subtracted from all other values. For SDS-PAGE, equal amounts of protein were loaded onto an 8-16% Tris-Glycine gel (Novex™ WedgeWell™), and electrophoresis was run at 100 V for 1 h in the running buffer. The gel was stained with Brilliant Blue (Sigma-Aldrich, Germany) for 1 h at room temperature, followed by destaining with water and destaining buffer (10% acetic acid, 50% methanol, and 40% H_2O). Protein bands were visualized immediately using a ChemiDoc imaging system (BioRad, USA).

6.3.6 Affibody Binding Analysis

To assess the Erbb3-specific binding of the affibody, it was labeled with fluorescein isothiocyanate (FITC) using the FITC Labeling Kit (Thermo Fisher, USA). The purified affibody was incubated with FITC solution overnight at 4°C, protected from light. After incubation, the labeled affibody was recovered using a Vivaspin 6 centrifugal concentrator (Sartorius, Germany) with a molecular weight cut-off (MWCO) of 10 kDa. The FITC-labeled affibody was then incubated with cells, as described in Section 2.3, to evaluate its binding affinity to Erbb3 via FACS.

6.3.7 Affibody Conjugation

PEI-affibody conjugates were prepared using an SPDP linker, followed by purification via ultrafiltration and ÄKTA chromatography as previously reported.[272] Briefly, SPDP was added to 1 mL of 1 mg/mL 5 kDa PEI, stirred and incubated overnight at room temperature. Simultaneously, the affibody was treated with SPDP and then was reduced by DTT under nitrogen gas after purification to introduce a sulfhydryl group. After purification, pyridyldithiol-activated PEI and sulfhydryl-activated affibodies were mixed and stirred at 4°C overnight. The final conjugates were purified using ultrafiltration and ÄKTA chromatography, and the concentration of PEI was determined spectrophotometrically at 405 nm using a TNBS assay. For C14-PEI-affibody conjugates, a similar process was followed to couple affibody with PEI, but PEG12-SPDP was used as the linker. Following conjugation, 1,2-epoxytetradecane was added to the solution for a ring-opening reaction as described in Chapter I.

6.3.8 Polyplex Preparation and Characterization

Polyplexes were prepared by combining PEI or PEI-affibody conjugate with RNA through electrostatic interactions. Specifically, 500 ng of eGFP mRNA and a predetermined amount of polymer or conjugate, based on the desired N/P ratios (nitrogen to phosphate ratio), were dissolved in high-purity water and mixed by pipetting and vortexing in 100 µL of 10 mM HEPES buffer, pH 7.4. The mixture was incubated at room temperature for 1 hour. For blended C14-PEI/PEI-affibody and C14-PEI/C14-PEI-affibody polyplexes, a similar method was used, with C14-PEI and affibody conjugates being pre-mixed before addition to the HEPES buffer.

Polyplex characterization was performed using a Zetasizer Ultra (Malvern, UK). To measure the hydrodynamic diameter, polydispersity index (PDI), and zeta potential, 100 µL of each polyplex sample in 10 mM HEPES buffer, pH 7.4, was placed in a disposable micro-cuvette (Malvern, UK). The hydrodynamic

diameter and PDI were determined by measuring at a 173° backscatter angle with 15 runs per sample, and measurements were repeated three times. For zeta potential measurements, the polyplexes were diluted with 700 µL of HEPES buffer and transferred to a folded capillary cell (Malvern, UK). Three measurements were taken for each sample using the same device.

6.3.9 Polyplex Transfection

To evaluate the delivery efficiency of mRNA by polyplexes, we assessed the cellular uptake of fluorescently labeled mRNA (AF405-mRNA or Cy5-mRNA) and the expression of the enhanced green fluorescent protein (eGFP) reporter gene using flow cytometry. Hop62 cells were used for tests with PEI-affibody polyplexes, while A549, Hop62, and H358 cells were used for C14-PEI/PEI-affibody and C14-PEI/C14-PEI-affibody polyplexes. Cells were seeded at a density of 30,000 cells per well in 24-well plates containing 500 µL of growth medium. After 24 h of incubation at 37°C with 5% CO_2, the cells were transfected with formulations encapsulating eGFP-mRNA or fluorescent-labeled mRNA. Following another 24 h of transfection, cells were washed with PBS and detached using 0.05% trypsin-EDTA. The detached cells were collected in 1.5 mL Eppendorf tubes, centrifuged at 500 g for 5 min, and the supernatant was removed. Cells were washed with PBS and centrifuged again. The final cell pellet was resuspended in fresh PBS, and fluorescence intensity was measured using the Attune NxT flow cytometer (Thermo Fisher, Germany).

6.3.10 Spectral Shift Test

Her3 (Erbb3, Sino biological, China) was labeled with protein Labeling Kit RED-NHS 2_{nd} Generation (NanoTemper Technologies GmbH, Germany). In particular, 20 µM of HER3 was incubated with 3x molar excess of RED-NHS 2_{nd} Generation dye. After 1 h of incubation in the dark, the labeled protein was purified using B-column of the labeling kit. Protein concentration (971 nM) and degree of labeling (0.45) were determined using Nanodrop. The labeling kit is specifically designed for RED detectors in Monolith X.

Ligand samples were prepared using a 16-point serial dilution in HEPES buffer (pH 7.4) with 10 µL in each PCR tube. 10 µL of the target (RED-NHS labeled HER3) were added to each ligand sample. 10 µL of the complex were loaded into premium coated capillaries (NanoTemper Technologies GmbH, Germany), and into the Monolith X. All Binding affinity measurements were conducted using the Monolith X instrument (NanoTemper Technologies GmbH, Germany), which is equipped with dual-emission detection optics. RED-NHS 2nd Generation, a fluorescent reporter with an emission peak of around 660 nm, was used. Fluorescence was recorded at 650 nm and 670 nm simultaneously for 5 seconds for each ratiometric reading. The data was processed using MO. Control software (NanoTemper Technologies GmbH, Germany), and the results were used to calculate the equilibrium dissociation constant (Kd).

6.3.11 Statistics

All results are given as mean value ± standard deviation (SD) of triplicate experiments (n=3) unless stated otherwise. Statistical significance was investigated using one-way ANOVA or two-way ANOVA. All statistical analyses were performed using GraphPad Prism software (GraphPad Software, USA).

6.4 Results

6.4.1 Erbb3 Over-Expressed in KRAS Mutated Lung Cancer Cells

TCGA and GTEx databases were used to confirm Erbb3 expression in lung cancer patients (Figure 1A). The data set includes 830 lung adenocarcinoma (LUAD) samples, with 483 tumor tissues and 347 normal tissues. The expression of Erbb3 was presented as Log2 TPM (transcripts per million) + 1. Statistical analysis revealed that Erbb3 is significantly upregulated in tumor tissues compared to normal tissues.

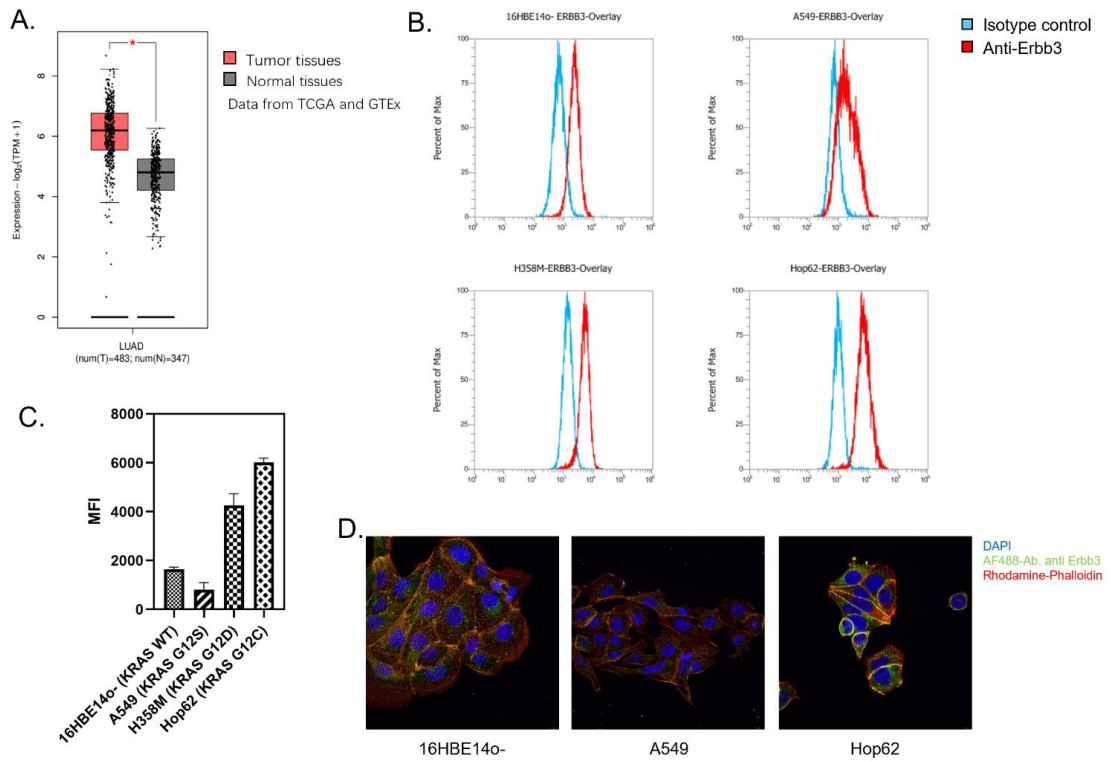

Figure 1. The expression of Erbb3 in lung cancer. A) Expression of Erbb3 in lung adenocarcinoma patients; **B)** Levels of Erbb3 receptors in lung cells measured by FACS; **C)** MFI of FACS measurement in lung cells; **D)** Erbb3 expression in lung cells assessed by confocal microscopy.

Although previous studies have demonstrated Erbb3 overexpression in lung cancer cells, variables such as handling, passage number, and cell line source can influence cellular characteristics.[273,274] Therefore, Erbb3 expression was examined and compared between healthy lung epithelial cells (16HBE14o-) and lung cancer cell lines (A549, H358M and Hop62) using flow cytometry and confocal microscopy. Cells were incubated with labeled Erbb3 antibodies, and median fluorescence intensity (MFI) was measured through flow cytometry, followed by confocal microscopy imaging. For flow cytometry (FACS), 16HBE14o- (*KRAS* WT), A549 (*KRAS* G12S), Hop62 (*KRAS* G12C), and H358M (*KRAS* G12D) cells were used. Cells were co-incubated with PE-conjugated anti-Erbb3 antibodies for 30 min prior to measurements, and isotype antibodies served as negative controls. The data demonstrated that Hop62 and H358M cells exhibited significant Erbb3 overexpression compared to 16HBE14o-, with a 3.67- and 2.39-fold increase, respectively (Figure 1C). In contrast, A549 cells did not show a higher MFI than 16HBE14o-, although a

shift in the positive signal was observed, consistent with previous studies (Figure 1B and 1C).[273,275]

These findings were corroborated by the confocal microscopy images (Figure 1D). The images show blue-stained nuclei (DAPI), red-stained F-actin (Rhodamine-Phalloidin), and green dots representing Erbb3 receptors labeled with AF488-conjugated antibodies. In 16HBE14o- cells (*KRAS* WT), Erbb3 was distributed evenly on the cell surface and within the cytoplasm after internalization. However, in A549 cells, only a few green dots were detected, indicating lower Erbb3 expression. In Hop62 cells, a higher number of Erbb3 signals were observed, particularly on the cell surface. As a result, Hop62 cells were selected for subsequent transfection experiments, with A549 cells used as controls.

6.4.2 Extraction of Engineered-Affibody

Schardt and colleagues engineered a trivalent affibody [270] utilizing the Z05413 affibody[276] as the HER3 binding domain, connected with a flexible, protease-resistant peptide spacer[277] as a linker. In our previous study, we successfully constructed a plasmid encoding the affibody with His-tags in our lab and transformed it into *E. coli* BL21 strains. To isolate the affibody, bacteria were cultured in LB medium at 37 °C until the OD600 reached 0.4-0.8. Protein expression was induced for 4 h, and the purification was carried out using a HisPur™ Ni-NTA Spin Purification Kit. The purified affibody products were verified by SDS-PAGE (Figure 2). In the lysate and flowthrough (lanes 2 and 3), total bacterial proteins were detected. After washing (lanes 4-6), affibody products were clearly present in the elutes (lanes 7 and 8). The main protein bands were observed between 35-55 kDa, which is higher than the expected molecular weight of 30.5 kDa. This discrepancy is consistent with observations by Schardt et al., attributing the higher apparent molecular weight to electrophoretic interference from the affibody's helix-loop-helix motifs.[270]

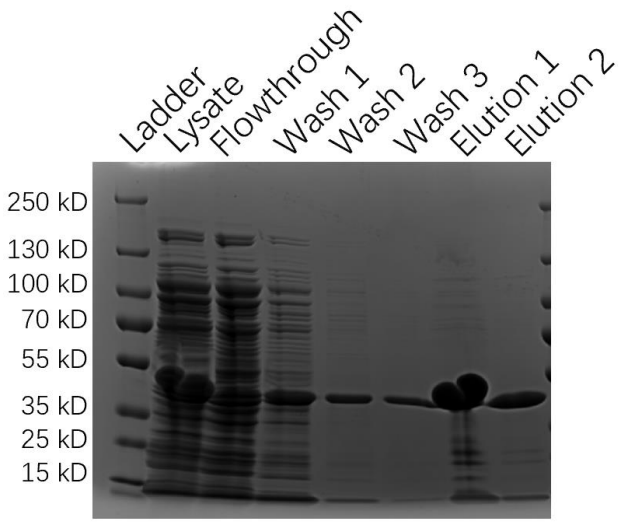

Figure 2. SDS-PAGE showing the products from the affibody extraction.

6.4.3 Prediction of The Affibody's Structure

To understand the properties of the affibody, we predicted its crystal structure with AlphaFold3.[278] As shown in the ribbon diagram (Figure 3A), the structure reveals a protein chain with a defined tertiary structure, featuring three distinct domains arranged side by side from the N-terminus to C-terminus. These domains appear as compact, likely globular regions, typical of binding domains, with surface features such as grooves or pockets that might interact with ligands or other proteins. The two regions between the binding domains, which are less structured or more elongated, represent the linkers. These linkers likely provide flexibility, allowing movement between the binding domains.

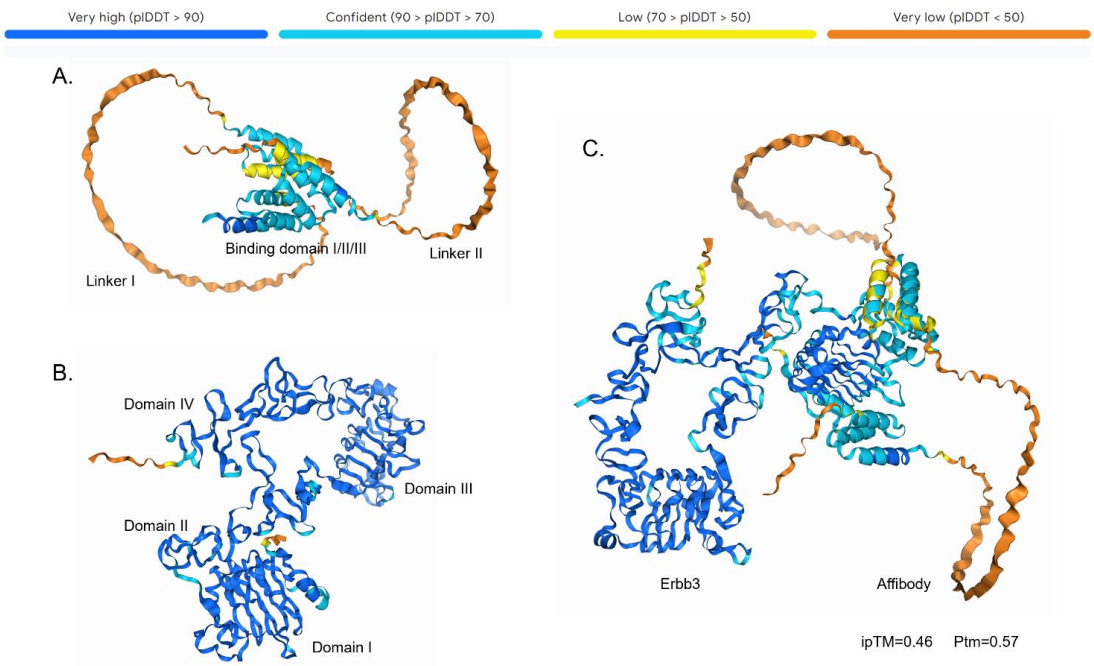

Figure 3. Prediction of affibody structure and its binding with Erbb3 using AlphaFold3. **A)** Predicted structure of the affibody; **B)** Predicted structure of Erbb3; **C)** The predicted binding interaction between affibody and Erbb3.

Then AlphaFold3 was used to predict the interaction between affibody and Erbb3. The structure of Erbb3, consisting of four domains, is shown in Figure 3B, which aligns with the previous report from Cho and Leahy[263]. Figure 3C shows the binding interaction between the affibody and Erbb3. The binding site is clearly visible, with the affibody's binding domains contacting domain I of Erbb3. This interaction region is likely crucial for the biological function of the complex, possibly involving key residues from both proteins. The binding appears to be complementary, with the surfaces of both proteins fitting together, suggesting a specific interaction driven by the shape and charge compatibility of the binding surfaces. The proteins are oriented in a way that likely reflects their natural binding conformation. While the linkers might allow some flexibility, the overall orientation is stable, suggesting a strong interaction.

6.4.4 Affinity Between Affibody and Erbb3

Based on the AlphaFold3 prediction, a strong interaction between the affibody and Erbb3 was expected. To experimentally verify this interaction, the affibody was labeled with FITC and co-incubated with Hop62 cells at 37°C for 24 h.

Following incubation, FACS was used to measure fluorescence intensity (Figure 4A). Trypan blue was applied to quench the fluorescence from any extracellular dye on the cell surface. Compared to the PBS-treated control group, the affibody-treated group exhibited a continuous increase in MFI over time, reaching a peak value of approximately 10,000 after 24 hours. These results demonstrate that the affibody can interact with cell membranes and be internalized through receptor-mediated endocytosis.

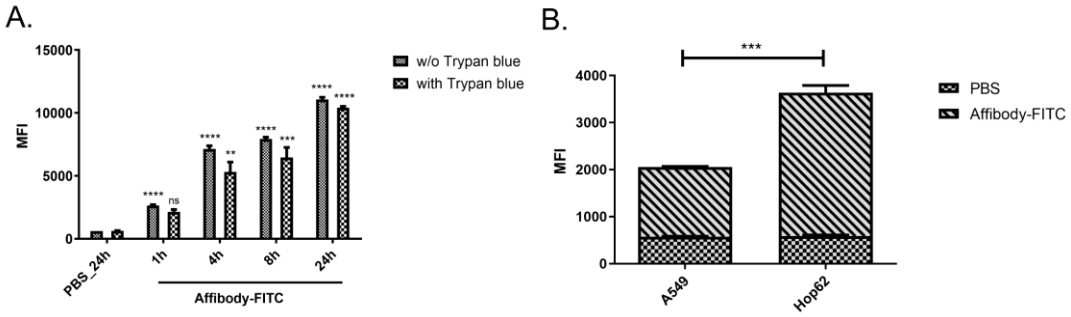

Figure 4. Erbb3 mediates affibody cellular uptake. A) FITC labeled affibody uptake in Hop62 cells after 24h (n=3, **P≤0.0021, ***P≤0.0002, ****P≤0.0001); **B)** Comparison of specific binding of affibody in A549 and Hop62 cells 24 h after treatment with the labeled affibody (n=3, t-test, ***P≤0.0001).

A549 and Hop62 are both lung cancer cell lines, but A549 cells express much lower levels of Erbb3 than Hop62 cells. To further confirm the specificity of the affibody for Erbb3, FITC-labeled affibody was incubated with both cell lines. As shown in Figure 4B, both A549 and Hop62 cells displayed similar fluorescence levels in the PBS-treated control group. However, after 24 h of affibody treatment, Hop62 cells exhibited significantly higher uptake of the labeled affibody compared to A549 cells. This result supports the conclusion that the affibody specifically recognizes and binds to Erbb3 receptors on Hop62 cells.

6.4.5 PEI-Affibody Conjugation

Various strategies for modifying polyplexes with targeting ligands have been described in the literature. The ligand can be attached either before or after polyplex formation. In our recent study, human transferrin was conjugated to chitosan nanoparticles using a strain-promoted azide-alkyne cycloaddition

reaction, enabling functional group attachment of transferrin to chitosan. This allowed for rapid, covalent surface conjugation under mild reaction conditions after nanoparticle formation.[261] Besides, another study used polyethylenimine (PEI) conjugated with 2,3-Dimethyl-maleic anhydride (DMMAn)-modified melittin (Mel) to create a pH-responsive Mel-PEI conjugate, which was then used to prepare polyplexes.[279] PEI is a well-established non-viral gene delivery vector due to its high positive charge density and excellent buffering capacity, facilitating endosomal escape of nucleic acids.[280] However, to reduce cytotoxicity, low molecular weight PEI (LMW-PEI) was chosen in this project to couple the Erbb3-specific affibody for mRNA encapsulation and delivery.

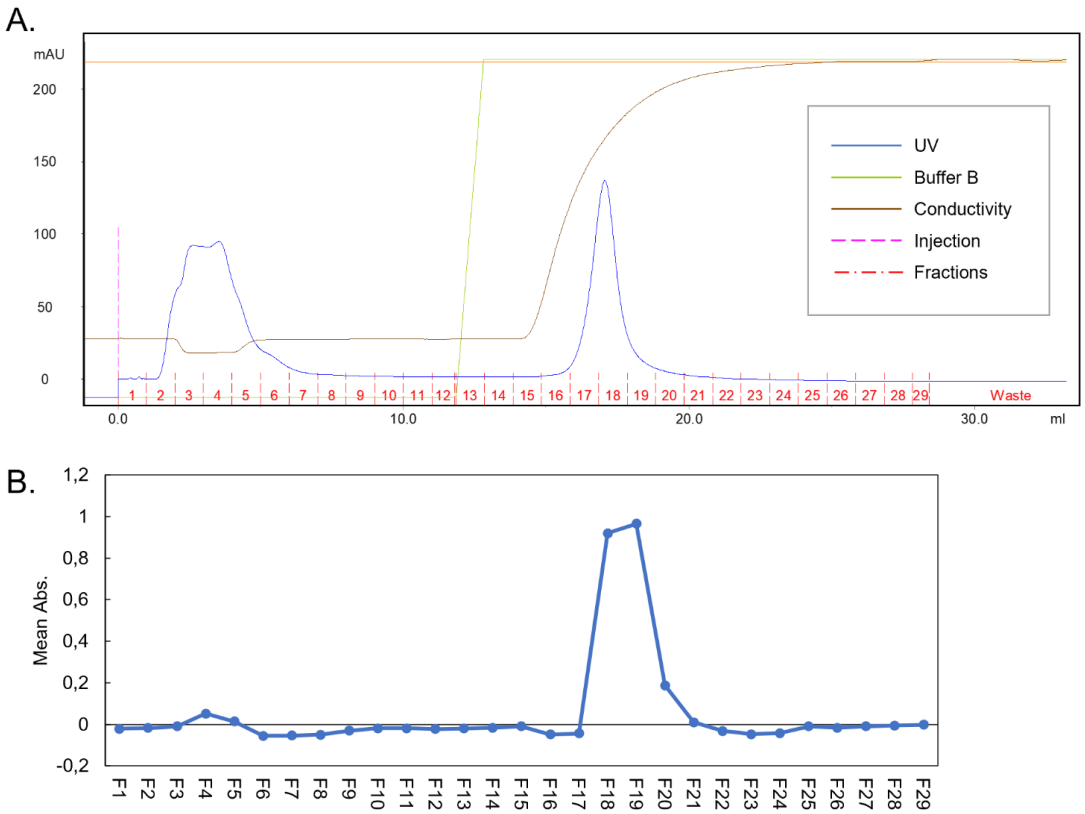

Figure 5. Purification and confirmation of PEI-affibody conjugates. A) ÄKTA profile showing the purification of PEI-affibody conjugates; **B)** TNBS profile of primary amines in fractions from the ÄKTA flowthrough.

PEI-affibody conjugates were synthesized using an SPDP linker and purified using ultrafiltration and an ÄKTA cation exchange chromatography system.[272] The molar ratio of affibody to PEI was approximately 1.5:1. SPDP is a short-chain crosslinker that links amines and sulfhydryls through N-hydroxysuccinimide (NHS)-ester and pyridyldithiol reactive groups, forming

cleavable disulfide bonds with cysteine residues. First, the primary amines in PEI reacted with the NHS-ester of SPDP in phosphate buffer (pH 7-8), and a similar reaction occurred between the affibody's amino acids and the NHS-ester of SPDP. DTT was then used to expose sulfhydryl groups on the SPDP-modified affibody. Finally, the pyridyldithiol-activated PEI was reacted with the sulfhydryl-activated affibody at pH 7-8 to form the conjugate. The final PEI-affibody conjugates were purified using an ultrafiltration system to remove free PEI and excess SPDP. Because PEI is a strongly cationic polymer, the conjugates were further purified using an ÄKTA system equipped with a HiTrap SP HP cation exchange column. As shown in Figure 5A, during low-salt buffer washing, free affibodies passed through the resin, while the PEI-affibody conjugates bound to the resin and were eluted under high conductivity conditions.

To confirm the presence of conjugates, a TNBS assay was performed to detect PEI's primary amine groups in the ÄKTA flow-through fractions. TNBS forms a highly chromogenic derivative with primary amines, measurable at 405 nm.[279] Figure 5B shows little to no absorbance in fractions F1-F17, with strong absorbance peaks in fractions 18-20, which corresponded to the elution of PEI-affibody conjugates in the ÄKTA chromatography. These results confirm that free affibodies were washed away in earlier fractions (F2-F6), while the PEI-affibody conjugates were successfully eluted in fractions F18-F20. Given that free PEI was removed during ultrafiltration, the amine signals detected in the TNBS assay were attributed to the PEI-affibody conjugates.

6.4.6 PEI-affibody Polyplexes Preparation

The hydrodynamic diameter, PDI, and zeta potential of the prepared polyplexes were determined using dynamic light scattering (DLS) and laser Doppler anemometry (LDA), respectively. As shown in Figure 6A, PEI-affibody polyplexes exhibited agglomeration, with sizes exceeding 1000 nm in 10 mM HEPES buffer (pH 7.4) for all tested N/P ratios except for N/P 1. The PDI values ranged from 0.2 to 0.7, indicating a broad particle size distribution. In contrast,

PEI polyplexes without affibody exhibited significantly smaller particle sizes, averaging 150 nm, with a mean PDI of 0.25, indicating lower polydispersity. One possible explanation for the agglomeration observed in PEI-affibody polyplexes is the affibody's isoelectric point (PI) of 5.1. When pH is at 7.4, affibody is partially deprotonated, resulting in negative charges, which in turn interact with the highly positive charge of PEI, resulting in particle aggregation. Particularly, with the N/P ratio increases, the effect becomes more pronounced.

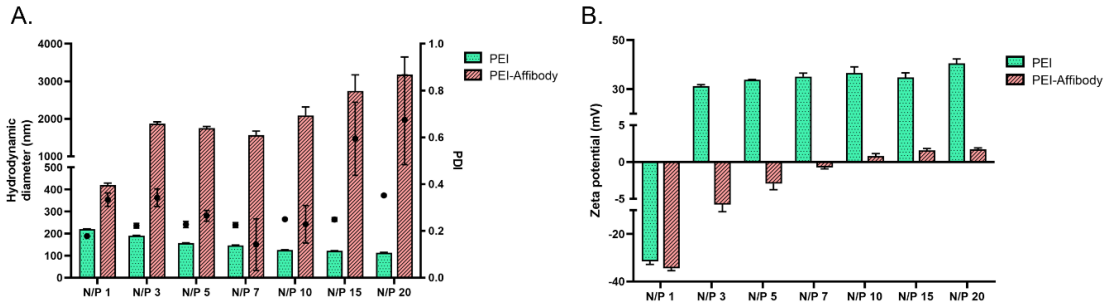

Figure 6. Characterization of PEI-affibody polyplexes. A) Hydrodynamic diameter (bars) and PDI (dots) of polyplexes (n=3); **B)** Zeta potential of polyplexes (n=3).

In terms of zeta potential, PEI polyplexes exhibited strongly positive zeta potentials beyond 30 mV, except N/P 1 (Figure 6B). The zeta potential of PEI-affibody polyplexes, however, varied with increasing N/P ratios. At lower N/P ratios (N/P 1 to N/P 7), PEI-affibody polyplexes displayed clearly negative zeta potentials, with the potential approaching neutrality at N/P 9. Slightly positive zeta potentials were observed starting at N/P 10, which is not sufficient, however, for introducing charge-mediated colloidal stability. This trend supports the particle size observations, where PEI-affibody polyplexes aggregated considerably, which can be well explained by the lack of net surface charge. While PEI polyplexes do not contain any charge-neutralizing affibody and are colloidally stabilized by positive charges, the conjugate polyplexes seem neutral on their surface due to the negatively charged affibody. Since most cellular membranes are negatively charged, positively charged polyplexes are generally more favorable for cellular uptake due to strong electrostatic interactions.[191]

6.4.7 mRNA Delivery with PEI-Affibody Polyplexes

To evaluate the cellular uptake of PEI-affibody polyplexes, mRNA was labeled with AF405. It has been previously demonstrated that cellular uptake is highly dependent on surface ligand density.[281] Thus, the uptake of PEI-affibody polyplexes in Hop62 cells was analyzed using FACS. PEI-affibody polyplexes at N/P ratios of 3, 5, 7, and 10 were tested, with PEI polyplexes prepared at corresponding N/P ratios for comparison. As shown in Figure 7A, following 24 h of transfection, PEI-affibody polyplexes at N/P ratios of 3, 5, and 7 did not exhibit a significant increase in cellular uptake compared to the PEI-only formulation. However, at N/P 10, the cellular uptake of PEI-affibody polyplexes was nearly twice that of the PEI formulation. Interestingly, the cellular uptake of PEI-affibody polyplexes remained consistent across the N/P ratios tested, suggesting that within this range, changes in the N/P ratio did not significantly affect uptake efficiency (Figure 7C). This observation is consistent with findings from previous studies, which have demonstrated that antibody-conjugated particles enhance cellular uptake through receptor-mediated endocytosis, improve cell penetration, and increase retention in target cell populations.[282] Considering the charge and size differences of the two types of polyplexes, the differences at low N/P ratios can easily be explained: small PEI polyplexes with highly positive zeta potential typically enter cells by adsorptive endocytosis, while large, charge-neutral affibody-modified polyplexes only exert significant receptor-mediated endocytosis at high N/P ratios, where unmodified PEI tends to be cytotoxic.

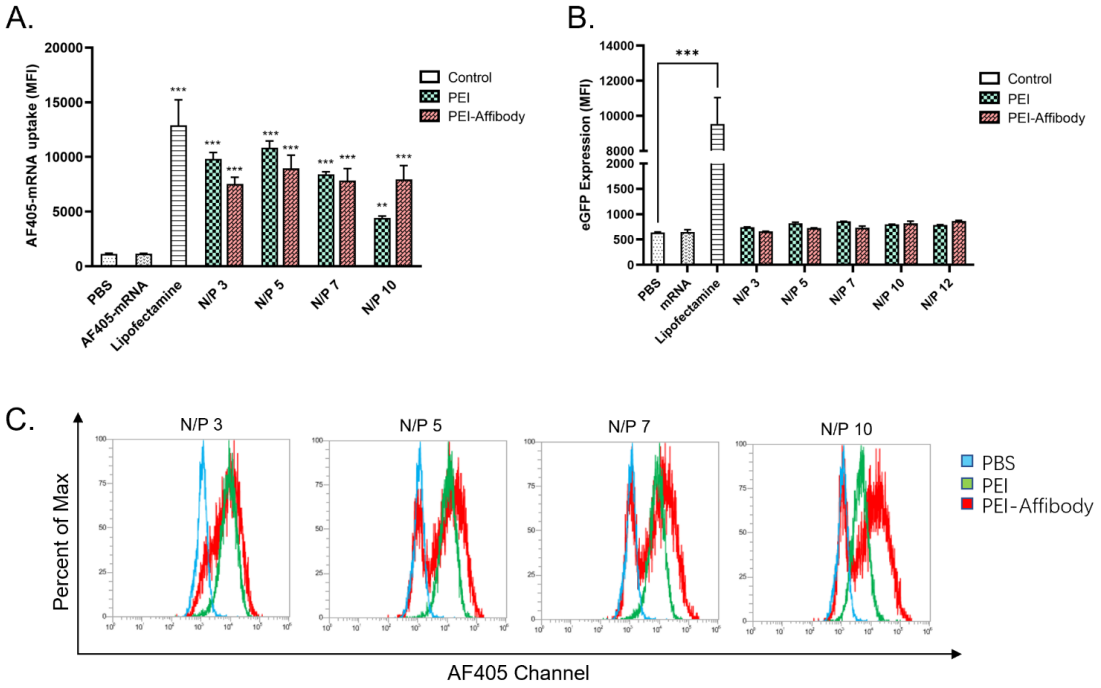

Figure 7. Delivery of PEI-affibody polyplexes in Hop62 cells. A) Uptake of PEI-affibody polyplexes measured by FACS (n=3, **P≤0.002, ***P≤0.001); **B)** eGFP expression of PEI-affibody polyplexes measured by FACS (n=2 or 3, ***P≤0.001); **C)** AF405 signal shift from FACS from uptake measurements.

Subsequently, the expression of eGFP mRNA was assessed following transfection with PEI-affibody polyplexes (Figure 7B). Both PEI-affibody and PEI polyplexes, containing eGFP mRNA, were prepared at N/P ratios of 3, 5, 7, 10, and 12 and transfected into Hop62 cells. eGFP mRNA expression was measured by FACS 48 h post-transfection. While the MFI showed a slight increase with higher N/P ratios, neither the PEI-affibody nor the PEI polyplex groups exhibited significant eGFP expression compared to the controls. PEI is one of the most widely used polymers for nucleic acid delivery and has been successfully employed for the delivery of various types of cargo, such as plasmids[283] and siRNA.[284] However, for mRNA delivery, PEI has not shown satisfactory efficiency. This is likely due to the nature of mRNA molecules, which consist of thousands of nucleotides and tend to form secondary structures in their single-stranded form.[57] These secondary structures result in strong interactions with the excessive positive charges of PEI, hindering the effective release of mRNA.[218] Although there is evidence that the size of the polyplexes can be optimized by adjusting the buffer, for example, achieving polyplexes

around 150 nm in 0.2 M carbonate buffer, this did not lead to improved mRNA expression (Figure S2).

6.4.8 C14-PEI-Affibody Conjugation

While the affibody was successfully shown to specifically target Erbb3-overexpressing lung cancer cells (Hop62 with *KRAS* G12S), effects of conjugates were less clear. Considering the limitations of mRNA delivery with PEI, in our previous study (Chapter I), a lipid-modified polyethylenimine (C14-PEI) polyplex system was developed for efficient delivery and expression of mRNA in A549 lung cancer cells. To further explore the potential of affibody-coupled polyplexes, we prepared conjugates of affibody and C14-PEI. The key difference between C14-PEI and PEI conjugation lies in the fact that the primary amine groups in C14-PEI are occupied by C14 alkyl chains, which may reduce the efficiency of affibody modification. To generate C14-PEI-affibody conjugates, PEI was first conjugated with affibodies using PEG12-SPDP as a linker, followed by coupling with C14 via a ring-opening reaction, as described previously (Chapter I). Following preparation, the conjugates were purified using ultra-filtration and ÄKTA to remove any unbound compounds and free affibodies (Figure S1). PEG12-SPDP, in addition to providing NHS ester and pyridyldithiol reactive groups like SPDP, contains a 12-unit polyethylene glycol (PEG) spacer, offering a linker arm extending up to 54.1 angstroms. The inclusion of PEG enhances solubility, increases linker length, and provides colloidal stability and biocompatibility to the particles. Additionally, PEGylation helps extend circulation time *in vivo* and reduces unwanted immune responses.[222,223]

6.4.9 C14-PEI-Affibody Polyplexes Preparation

The density of proteins on nanoparticles significantly influences polyplex properties. Overcrowding of antibodies on the nanoparticle surface can create steric hindrance, reducing the ability of individual antibodies to bind effectively to their targets.[281] Additionally, excessive antibodies may alter the surface charge or stability of the nanoparticles, potentially affecting their performance

in biological systems.[285] To optimize polyplex properties, a blending strategy was employed, wherein C14-PEI and C14-PEI-affibody were mixed in different proportions, with PEI-affibody used as a comparison.[279] As described in Section 2.8, polyplexes were prepared by adding 0%, 10%, and 30% C14-PEI-affibody or PEI-affibody conjugates to HEPES buffer containing C14-PEI. The polymer solution was vortexed and then incubated with the mRNA solution, allowing for self-assembly. As shown in Figure 8, blending affibody conjugates led to increased particle size and reduced zeta potential across all formulations. This trend was particularly pronounced in the PEI-affibody blends. In the absence of affibody conjugates, C14-PEI polyplexes exhibited a size of approximately 300 nm and a zeta potential of around 40 mV, consistent with previous findings (Chapter I). However, as the affibody proportion increased, notable changes were observed, which again can be explained by the negative charge of the affibody at pH 7.4. For instance, at 30% affibody-conjugation, the C14-PEI/PEI-affibody polyplexes reached a size of 3000 nm with a zeta potential of 6 mV, while C14-PEI/C14-PEI-affibody polyplexes displayed a size of 2000 nm and a zeta potential of approximately 20 mV. Furthermore, higher standard deviations of the PDI indicated greater size dispersity in these polyplexes. Previous studies have demonstrated that surface modifications, particularly involving protein characteristics and positioning, significantly influence particle size and charge. Additionally, high ionic strengths and elevated protein content can contribute to particle aggregation, potentially reducing the stability and applicability of the polyplexes in certain settings.[279,285] In the case of blending C14-PEI with the C14-PEI-affibody, a formulation with acceptable properties was obtained when only 10% protein-modified C14-PEI was used. Their particle size of around 370 nm and zeta potential of nearly 21 mV reflect that with a decreased amount of negatively charged affibody, the zeta potential is less affected, leading to acceptable colloidal stability.

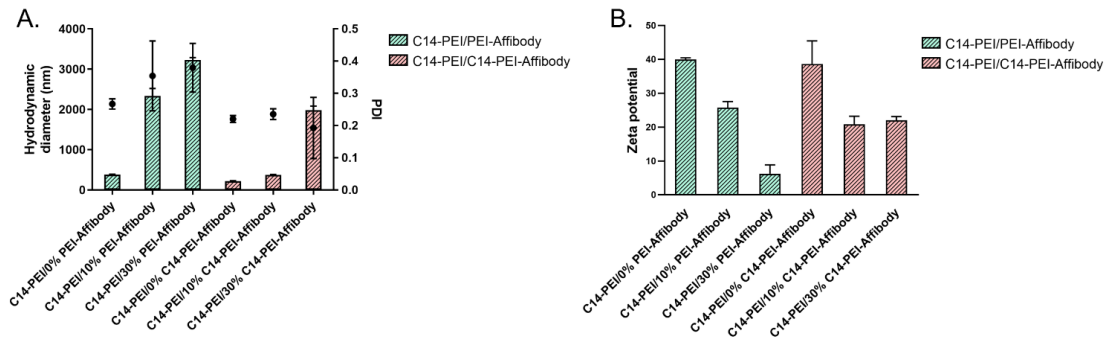

Figure 8. Characterization of C14-PEI/PEI-affibody and C14-PEI/C14-PEI-affibody polyplexes. A) hydrodynamic diameter (bars) and PDI (dots) of polyplexes (n=3); **B)** zeta potential of polyplexes (n=3).

6.4.10 mRNA Delivery with C14-PEI-Affibody Polyplexes

Polyplexes were prepared by blending 0%, 10%, and 30% C14-PEI-affibody or PEI-affibody conjugates with C14-PEI. These polyplexes were then transfected with Cy5-labeled eGFP mRNA into A549, Hop62, and H358 cells to assess cellular internalization and expression (Figures 9A and 9B). After 24 h, PEI-affibody conjugated polyplexes demonstrated a modest increase in cellular uptake with higher affibody content in A549 cells. However, this increase appeared to be more a result of differences in particle characteristics such as size and zeta potential rather than receptor-mediated internalization, as A549 cells have low Erbb3 receptor expression. Conversely, C14-PEI-affibody conjugates resulted in decreased uptake, which correlated with the density of C14-PEI-affibody. Furthermore, all formulations across the three cell lines showed generally reduced eGFP mRNA expression in the presence of affibody conjugates.

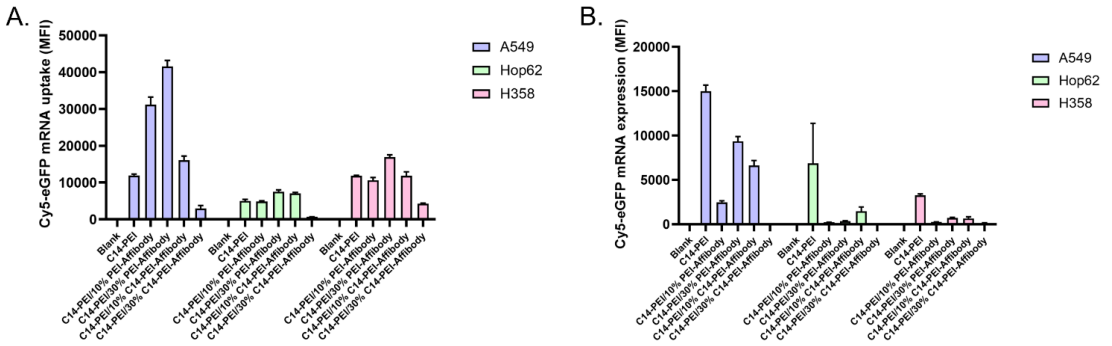

Figure 9. Delivery of C14-PEI/PEI-affiobdy and C14-PEI/C14-PEI-affibody polyplexes in

A549, Hop62, and H358 cells. A) Uptake of polyplexes measured by FACS (n=3); **B)** eGFP expression of polyplexes measured by FACS (n=3).

We confirmed that the expressed affibody can specifically bind to Erbb3, which fits the literature reports (Figures 2B and 2C),[270] and observed a trend in which PEI-affibody conjugates may increase retention in targeted cell populations (Figures 7A and 7C). Nonetheless, the performance of affibody-conjugated polyplexes varied with different formulations and conjugates. This variability may be due to several factors. First, as previously noted, an excess of antibodies can alter particle size, PDI, and zeta potential, impacting their behavior in biological systems.[285] Therefore, parameters need optimization for each blend ratio as they can vary significantly (Figures 8A and 8B). Second, the position, density, and flexibility of antibodies on nanoparticles can significantly influence targeting efficiency.[281] The reaction between thiol and primary amine moieties from cysteine and lysine residues can lead to random antibody orientation, resulting in inefficient ligand packing and reduced antigen-binding activity.[286] Thus, the conjugation method and choice of linkers are critical. Studies have shown that "click chemistry" offers high stereospecificity and yield with minimal by-products under mild conditions.[255,287] Additionally, the route of cellular uptake can be affected by the type of targeting agent. While scavenger receptor-mediated endocytosis is common for nanoparticle uptake, some targeting ligands may facilitate receptor-specific uptake.[257] Our recent research highlighted that monovalent ligands often cannot compete with multivalent ones.[288] However, other studies suggest that for certain antibody-mediated endocytosis processes, such as transferrin clathrin-mediated internalization, size may be more crucial than multivalency due to the limited size of natural clathrin-coated pits.[289,290] In the reported experiments, the surface charge seems to affect cellular uptake most importantly. However, to exclude the possibility of impaired affibody recognition by the receptor post-coupling, affinity tests were performed.

6.4.11 Affinity Test by Spectral Shift

Spectral shift technology was used to investigate the affinity of affibody and its

conjugates with RED-NHS labeled HER3.[291] This fluorescence-based biophysical technique quantifies molecular interaction strength by detecting wavelength shifts in the emission spectrum of a fluorophore (RED-NHS 2nd Generation dye) When a target molecule binds to a ligand, the chemical environment around the fluorophore changes, causing a shift in the emission wavelength The measurement is reported as a ratio of fluorescence emissions at two wavelengths (670 and 650 nm), and the binding affinity is expressed as the equilibrium Kd, which is inversely related to affinity. A lower Kd indicates stronger molecular interaction. In this test, PEI-affibody conjugates, C14-PEI-affibody conjugates, C14-PEI/ PEI-affibody polyplexes, and C14-PEI/ C14-PEI-affibody polyplexes were involved. Free affibody and C14-PEI served as positive and negative controls, respectively. As shown in Figure 10A, free affibody exhibited significant binding signals with increasing concentrations, yielding a Kd value of 56.1 ± 328.8 pM. In contrast, at the same range of concentrations, C14-PEI didn't show any affinity with Erbb3 (Figure 10E), until a very high concentration demonstrated unspecific binding (data not shown). Both PEI-affibody and C14-PEI-affibody conjugates showed similar binding profiles (Figures 10B and 10C), with measurable Kd values at 3.49 ± 1.39 nM and 17.7 ± 7.4 nM, respectively, demonstrating that affibody conjugates retain function but with reduced affinity compared to free affibody. However, the C14-PEI/PEI-affibody polyplex formulations showed no binding to Erbb3 (Figure 10D), consistent with the FACS results for cellular uptake and expression. These findings further confirm the potential of affibody-conjugated polymers for targeting Erbb3 and prove our previous hypothesis that the targeting and binding abilities mediated by affibody were reduced or shielded because of the affibody orientation and position in polyplexes preparation.

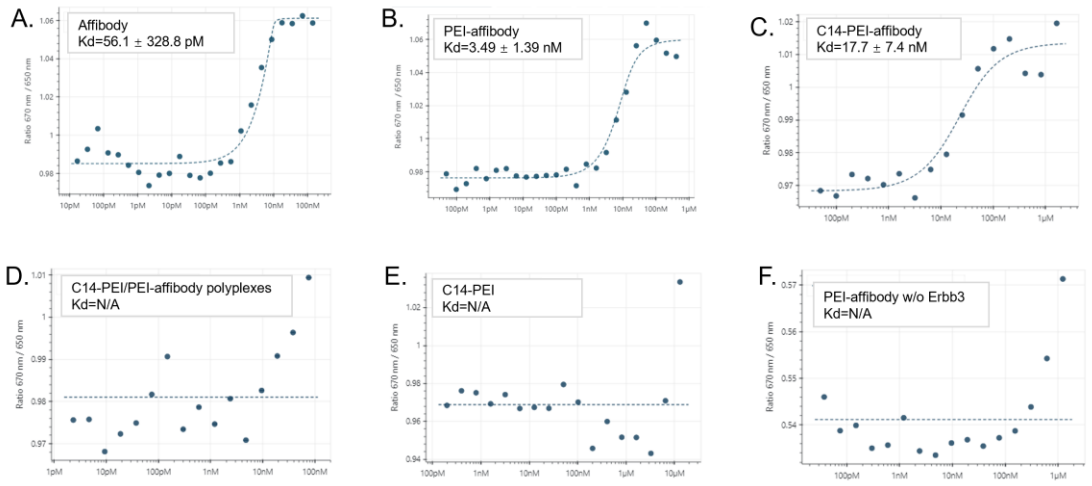

Figure 10. Spectral shift dose-response curves for affibody (A.), PEI-affibody conjugates (B.), C14-PEI-affibody conjugates (C.), C14-PEI/PEI-affibody polyplexes (D.), and only C14-PEI (E.) against RED-Erbb3. PEI-affibody conjugates with RED dye (w/o Erbb3) were used as a control (F.).

These findings validate the potential of affibody-conjugated polymers for targeting Erbb3 and support our hypothesis that the targeting and binding efficacy of affibody are compromised due to its orientation and positioning in the polyplexes. This underscores the need for careful design of targeted nanoparticles, considering the formulation, characteristics, ligands, and conjugation methods. Optimizing these parameters is likely to enhance the behavior of targeted polyplexes. Despite these challenges, our results demonstrate that engineered affibody-conjugated polyplexes at high N/P ratios improve uptake in targeted cells. This work highlights the importance of understanding polyplex formulation and conjugation methods to design and engineer effective targeted polyplexes for cell-specific mRNA therapeutics.

6.5 Conclusion

mRNA-based polyplexes offer several advantages, including transient expression with controlled, time-limited therapeutic effects, avoidance of genomic integration that preserves the integrity of the host genome, and reduced immunogenicity compared to viral vectors.[8,56,72] These benefits highlight the safety and increasing interest in mRNA-based polyplex delivery. Antibody conjugation in the engineering of polyplexes offers the dual benefit of prolonging cell surface binding, thereby enhancing polyplex uptake, while also

ensuring selective binding to target cells. This approach provides a safe, biocompatible, and targeted method for delivering mRNA to specific cells and tissues.[292] In this study, we used an engineered affibody as a proof-of-concept targeting ligand due to its well-documented characteristics and the ability to target the Erbb3 receptor, which is relevant for lung cancer delivery. After confirming Erbb3 overexpression in *KRAS* mutant lung cancer cells and the binding between affibody and Erbb3, we employed NHS-ester and pyridyldithiol reactive groups from chemical linkers to conjugate affibody with PEI and C14-PEI. We successfully prepared polyplexes with various formulations. Our study provides insights into the targeting capabilities of affibody-conjugated polyplexes. We observed that particle size, PDI, charge, uptake, and expression were influenced by changes in polyplex formulation, conjugation strategy, and affibody density. We demonstrated that by adjusting the formulation and affibody amount, we were able to modify binding behaviors. However, further research is needed to optimize nanoparticle characteristics and delivery efficiency by refining formulation and conjugation methods. Additionally, evaluating the most effective transport pathways for targeted polyplex delivery is essential. In conclusion, our findings validate the strategy of affibody conjugation with polyplexes, laying the groundwork for future studies and providing a promising platform for understanding ligand conjugation in the targeted delivery of mRNA.

6.6 Supplementary Information

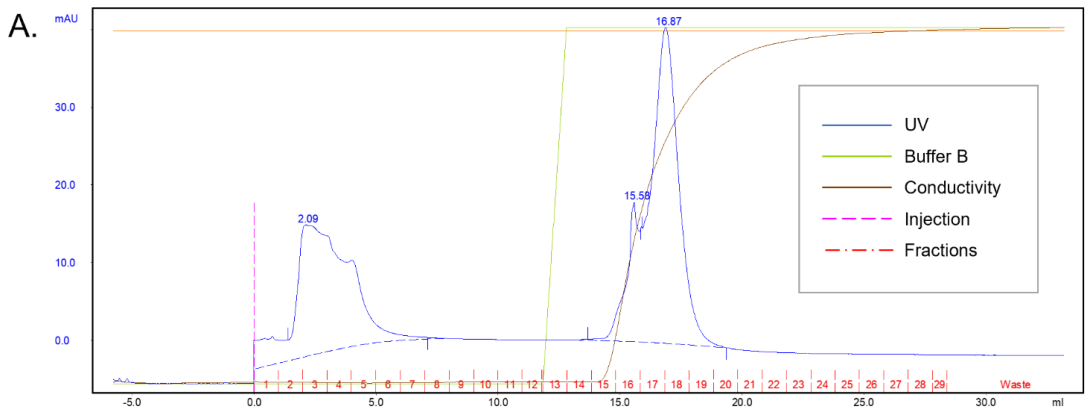

Figure S1. ÄKTA profile of C14-PEI-affibody conjugation.

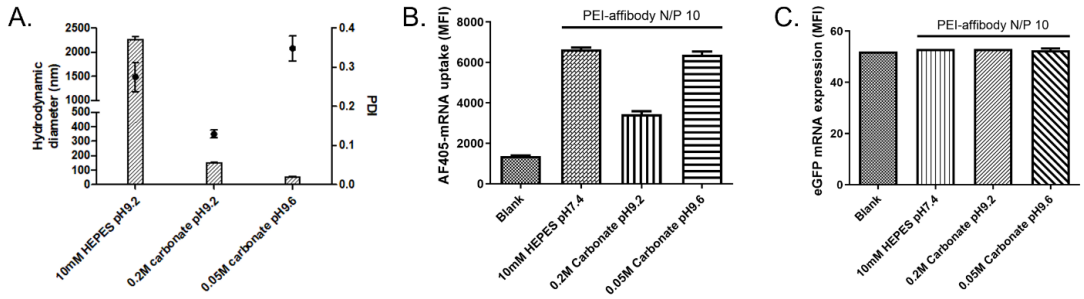

Figure S2. PEI-affibody polyplexes in different buffers (10 mM HEPES pH 7.4, 0.2 M carbonate pH 9.2, and 0.05 M carbonate pH 9.6). A) Hydrodynamic diameter (bars) and PDI (dots) of PEI-affibody polyplexes at N/P 10 (n=3); **B)** Uptake of PEI-affibody polyplexes at N/P 10 (n=2); **C)** eGFP expression of PEI-affibody polyplexes at N/P 10 (n=2).

6.7 Acknowledgements

The authors thank Prof. Georgios Stathopoulos for providing the Hop62 and H358M cells. Siyu Chen acknowledges the financial support from the China Scholarship Council (CSC). Simone Carneiro thanks the financial support from the Alexander von Humboldt Foundation and the Center of Nanoscience (CeNS) Munich. This research was partially funded by ERC-2014-StG-637830 to Olivia Merkel and by the BMBF within the framework of the Cluster4Future program (Cluster for Nucleic Acid Therapeutics Munich, CNATM) (Project ID: 03ZU1201AA).

7. Summary and Outlook

The studies in this thesis describe the successful synthesis of a lipid-modified PEI-based polymer, C14-PEI, and the development of a novel formulation for the co-delivery of Cas9 mRNA and sgRNA targeting *KRAS* mutations in lung cancer. Chapter I demonstrates the synthesis of C14-PEI from 1,2-epoxytetradecane and branched PEI 600 Da via a ring-opening reaction. The polymer demonstrated effective mRNA condensation through electrostatic interactions across all tested conditions, with optimal performance at w/w 8 and pH 7.4. Nanoparticles exhibited a hydrodynamic diameter of approximately 300 nm and a zeta potential of 40 mV. C14-PEI nanoplexes efficiently co-delivered Cas9 mRNA and sgRNA, achieving 62.67% indel efficacy in *KRAS*-mutant lung cancer cells. This was confirmed by agarose gel analysis, ddPCR, and Sanger sequencing. Knockout of the *KRAS* G12S mutation in A549 cells led to reduced phosphorylated-AKT and phosphorylated-ERK levels, impairing cell migration and increasing apoptosis.

Despite these promising results, the size and zeta potential of C14-PEI micelleplexes may induce immune responses and reduce *in vivo* efficiency. Chapter II therefore focused on optimizing this formulation using the anionic polymer PEG-PLE. The resulting polyplexes displayed enhanced characteristics, including reduced nanoparticle size (from 330 nm to 140 nm) and more neutral zeta potential (from +40 mV to -14 mV). Among the formulations, PEG-PLE/C14-PEI at a w/w ratio of 0.2 demonstrated optimal properties with low toxicity, high encapsulation efficiency, and effective mRNA delivery. Confocal microscopy confirmed efficient endosomal escape and intracellular distribution of Cas9 mRNA and sgRNA. Uptake pathway studies indicated that PEG-PLE/C14-PEI is internalized primarily through scavenger receptors and clathrin-mediated endocytosis. This formulation also achieved the highest gene editing efficiency reflected in *KRAS* G12S deletion among all tested samples, resulting in significant cancer cell apoptosis and migration inhibition in A549 cells.

Chapter III explored engineered affibody-conjugated polyplexes for targeted delivery in Erbb3-overexpressing lung cancer cells. The properties and delivery behaviors of the affibody-conjugated polyplexes were influenced by formulation and conjugation strategies. We chose the engineered affibody as a proof-of-concept targeting ligand due to its well-characterized ability to bind the Erbb3 receptor, which is upregulated in *KRAS*-mutant lung cancer cells. Polymer-affibody conjugates were prepared using NHS-ester and pyridyldithiol reactive groups from chemical linkers. Polyplexes were then formulated, and we observed that particle size, PDI, charge, cellular uptake, and gene expression varied depending on the formulation, conjugation strategy, and affibody density. Our results showed that affibody conjugates at high conjugate excess may target Erbb3 to increase retention within targeted cell populations. By adjusting the formulation and affibody amount, we were able to modify binding behaviors.

Overall, these findings highlight the potential of the C14-PEI formulation in advancing CRISPR-Cas9 therapies for targeted genetic interventions, particularly for *KRAS* mutations in cancer treatment. The studies reported here address key challenges in mRNA delivery and offer valuable insights into ligand-conjugated nanoparticles for targeted applications. Future work will focus on further optimization of nanoparticle characteristics, delivery efficiency, and biosafety, with particular emphasis on refining conjugation strategies and evaluating *in vivo* potential for clinical translation.

8. List of Abbreviations

5moU	5-methoxyuridine
AAVs	Adeno-associated viruses
AD	Alzheimer's disease
AF405	Alexa fluor 405
AF488	Alexa fluor 488
AuNP	Gold nanoparticle
BSA	Bovine serum albumin
C14-PEI	1,2-epoxytetradecane modified polyethylenimine
CAR-T	Chimeric antigen receptor T cells
CCK-8	Cell counting kit-8
CLSM	Confocal laser scanning microscopy
CMC	Critical micelle concentration
CPP	Cell-penetrating peptide
CRISPR	Clustered regularly interspaced short palindromic repeats
crRNA	CRISPR RNA
Cryo-EM	Cryo-electron microscopy
DAPI	6-diamidino-2-phenylindole dihydrochloride
ddPCR	Droplet Digital PCR
DLS	Dynamic light scattering
DMEM	Dulbecco's modified eagle medium
DSB	Double-strand break
dsDNA	Double-stranded DNA
DTT	Dithiothreitol
ECD	Extracellular binding domain
EDTA	Ethylenediaminetetraacetic acid
eGFP	Enhanced green fluorescent protein
EGFR	Epidermal growth factor receptor
eIFs	Eukaryotic translation initiation factors
EMSA	Electrophoretic mobility shift assays
EPR	Enhanced permeability and retention
Erbb3	Receptor tyrosine-protein kinase 3

EVs	Extracellular vesicles
FACS	Flow cytometry
FBS	Fetal bovine serum
FITC	Fluorescein isothiocyanate
Fluc mRNA	Luciferase protein reporter mRNA
GPC	Gel permeation chromatography
GTEx project	The Genotype-Tissue Expression project
HD	Huntington's disease
HDR	Homology-directed repair
HEPES	4-(2-hydroxyethyl)-1-piperazineethanesul-fonic acid
HER3	Human epidermal growth factor receptor 3
HIV	Human immunodeficiency viruses
HRP	Horseradish peroxidase
Indels	Insertions or deletions
IPTG	Isopropyl β-d-1-thiogalactopyranoside
IVT	*In vitro* transcription
Kd	Equilibrium dissociation constant
kDa	Kilo Dalton
KRAS	Kirsten rat sarcoma 2 viral oncogene homolog
LB	Lysogeny broth
LDA	Laser Doppler anemometry
LMW-PEI	Low molecular weight polyethylenimine
lncRNA	Long noncoding RNA
LNP	Lipid nanoparticle
LUAD	Lung adenocarcinoma
m1ψ	N1-methylpseudouridine
m7G	7-methylguanosine
MFI	Median fluorescence intensity
mRNA	Messenger RNA
N/P ratios	Nitrogen to phosphate ratio
ncRNA	Noncoding RNA
ND	Neurodegenerative diseases
NHEJ	Non-homologous end joining
NHS-ester	N-hydroxysuccinimide

NMR	Nuclear magnetic resonance spectroscopy
NPs	Nanoparticles
NSCLC	Non-small cell lung cancer
nt	Nucleotide
NTA	Nanoparticle tracking analysis
NTPs	Nucleoside triphosphosphates
ORF	Open reading frame
OTEs	Off-target effects
PABP	Poly(A)-binding protein
PAM	Protospacer adjacent motif
PBAE	Poly(β-amino ester)
PBS	Phosphate buffered saline
PCR	Polymerase chain reaction
PD	Parkinson's disease
PDI	Polydispersity indices
PEG	Polyethylene glycol
PEG-b-PLE	Methoxy-poly(ethylene glycol)-block-poly(l-glutamic acid sodium salt)
PEI	Polyethylenimine
PFA	Paraformaldehyde
PGA	Poly(l-glutamic acid)
PI	Propidium iodide
PIC	Preinitiation complex
PLGA	Poly(lactic-co-glycolic) acid
RNP	Ribonucleoprotein complex
SCD	Sickle cell disease
SD	Standard deviation
SDS-PAGE	Sodium dodecyl sulfate-polyacrylamide gel electrophoresis
sgRNA	Single-guide RNA
SPDP	Succinimidyl 3-(2-pyridyldithio) propionate
T7EI	T7 endonuclease I
TBST	Tris-buffered saline with 1% Tween 20
TCGA	The cancer genome atlas program
TNBS	Trinitrobenzene sulfonic acid

TPM	Transcripts per million
tracrRNA	Trans-activating crRNA
UTR	Untranslated region
w/w	Weight-to-weight ratios
WB	Western blot
WT	Wild type
ζ potential	Zeta potential
ψ	Pseudouridine

9. References

1 Bray, F. *et al.* Global cancer statistics 2022: GLOBOCAN estimates of incidence and mortality worldwide for 36 cancers in 185 countries. *CA Cancer J Clin* **74**, 229-263, doi:10.3322/caac.21834 (2024).

2 Hirsch, F. R. *et al.* Lung cancer: current therapies and new targeted treatments. *Lancet* **389**, 299-311, doi:10.1016/S0140-6736(16)30958-8 (2017).

3 Boettcher, M. & McManus, M. T. Choosing the Right Tool for the Job: RNAi, TALEN, or CRISPR. *Mol Cell* **58**, 575-585, doi:10.1016/j.molcel.2015.04.028 (2015).

4 Cong, L. *et al.* Multiplex genome engineering using CRISPR/Cas systems. *Science* **339**, 819-823, doi:10.1126/science.1231143 (2013).

5 Germer, J. *et al.* Lipo-Xenopeptide Polyplexes for CRISPR/Cas9 based Gene editing at ultra-low dose. *J Control Release* **370**, 239-255, doi:10.1016/j.jconrel.2024.04.037 (2024).

6 Lin, Y. *et al.* Chemical Evolution of Amphiphilic Xenopeptides for Potentiated Cas9 Ribonucleoprotein Delivery. *J Am Chem Soc* **145**, 15171-15179, doi:10.1021/jacs.3c01902 (2023).

7 Liu, C., Zhang, L., Liu, H. & Cheng, K. Delivery strategies of the CRISPR-Cas9 gene-editing system for therapeutic applications. *J Control Release* **266**, 17-26, doi:10.1016/j.jconrel.2017.09.012 (2017).

8 Kowalski, P. S., Rudra, A., Miao, L. & Anderson, D. G. Delivering the Messenger: Advances in Technologies for Therapeutic mRNA Delivery. *Mol Ther* **27**, 710-728, doi:10.1016/j.ymthe.2019.02.012 (2019).

9 Ishino, Y., Shinagawa, H., Makino, K., Amemura, M. & Nakata, A. Nucleotide sequence of the iap gene, responsible for alkaline phosphatase isozyme conversion in Escherichia coli, and identification of the gene product. *J Bacteriol* **169**, 5429-5433, doi:10.1128/jb.169.12.5429-5433.1987 (1987).

10 Mojica, F. J., Juez, G. & Rodriguez-Valera, F. Transcription at different salinities of Haloferax mediterranei sequences adjacent to partially modified PstI sites. *Mol Microbiol* **9**, 613-621, doi:10.1111/j.1365-2958.1993.tb01721.x (1993).

11 Jinek, M. *et al.* A programmable dual-RNA-guided DNA endonuclease in adaptive bacterial immunity. *Science* **337**, 816-821, doi:10.1126/science.1225829 (2012).

12 Mashiko, D. *et al.* Generation of mutant mice by pronuclear injection of circular plasmid expressing Cas9 and single guided RNA. *Sci Rep* **3**, 3355, doi:10.1038/srep03355 (2013).

13 Gratz, S. J. *et al.* Genome engineering of Drosophila with the CRISPR RNA-guided Cas9 nuclease. *Genetics* **194**, 1029-1035, doi:10.1534/genetics.113.152710 (2013).

14 Hwang, W. Y. *et al.* Efficient genome editing in zebrafish using a CRISPR-Cas system. *Nat Biotechnol* **31**, 227-229, doi:10.1038/nbt.2501 (2013).

15 Shan, Q. *et al.* Targeted genome modification of crop plants using a CRISPR-Cas system. *Nat Biotechnol* **31**, 686-688, doi:10.1038/nbt.2650 (2013).

16 Cho, S. W., Kim, S., Kim, J. M. & Kim, J. S. Targeted genome engineering in human cells with the Cas9 RNA-guided endonuclease. *Nat Biotechnol* **31**, 230-232, doi:10.1038/nbt.2507 (2013).

17 Feng, Z. *et al.* Efficient genome editing in plants using a CRISPR/Cas system. *Cell Res* **23**, 1229-1232, doi:10.1038/cr.2013.114 (2013).

18 Makarova, K. S. & Koonin, E. V. Annotation and Classification of CRISPR-Cas Systems. *Methods in molecular biology* **1311**, 47-75, doi:10.1007/978-1-4939-2687-9_4 (2015).

19 Makarova, K. S. *et al.* Evolutionary classification of CRISPR-Cas systems: a burst of class 2 and derived variants. *Nat Rev Microbiol* **18**, 67-83, doi:10.1038/s41579-019-0299-x (2020).

20 Shmakov, S. *et al.* Discovery and Functional Characterization of Diverse Class 2 CRISPR-Cas Systems. *Molecular cell* **60**, 385-397, doi:10.1016/j.molcel.2015.10.008 (2015).

21 Ishino, Y., Krupovic, M. & Forterre, P. History of CRISPR-Cas from Encounter with a Mysterious Repeated Sequence to Genome Editing Technology. *J Bacteriol* **200**, doi:10.1128/JB.00580-17 (2018).

22 Bhatia, S., Pooja & Yadav, S. K. CRISPR-Cas for genome editing: Classification, mechanism, designing and applications. *Int J Biol Macromol* **238**, 124054, doi:10.1016/j.ijbiomac.2023.124054 (2023).

23 Wiedenheft, B., Sternberg, S. H. & Doudna, J. A. RNA-guided genetic silencing systems in bacteria and archaea. *Nature* **482**, 331-338, doi:10.1038/nature10886 (2012).

24 Nishimasu, H. *et al.* Crystal Structure of Staphylococcus aureus Cas9. *Cell* **162**, 1113-1126, doi:10.1016/j.cell.2015.08.007 (2015).

25 Wang, H., La Russa, M. & Qi, L. S. CRISPR/Cas9 in Genome Editing and Beyond. *Annu Rev Biochem* **85**, 227-264, doi:10.1146/annurev-biochem-060815-014607 (2016).

26 Abudayyeh, O. O. *et al.* C2c2 is a single-component programmable RNA-guided RNA-targeting CRISPR effector. *Science* **353**, aaf5573, doi:10.1126/science.aaf5573 (2016).

27 Casini, A. *et al.* A highly specific SpCas9 variant is identified by *in vivo* screening in yeast. *Nature biotechnology* **36**, 265-271, doi:10.1038/nbt.4066 (2018).

28 Nakade, S., Yamamoto, T. & Sakuma, T. Cas9, Cpf1 and C2c1/2/3-What's next? *Bioengineered* **8**, 265-273, doi:10.1080/21655979.2017.1282018 (2017).

29 Xie, H. *et al.* SaCas9 Requires 5'-NNGRRT-3' PAM for Sufficient Cleavage and Possesses Higher Cleavage Activity than SpCas9 or FnCpf1 in Human Cells. *Biotechnology journal* **13**, e1700561, doi:10.1002/biot.201700561 (2018).

30 Amrani, N. *et al.* NmeCas9 is an intrinsically high-fidelity genome-editing platform. *Genome Biol* **19**, 214, doi:10.1186/s13059-018-1591-1 (2018).

31 Kim, E. *et al. In vivo* genome editing with a small Cas9 orthologue derived from Campylobacter jejuni. *Nature communications* **8**, 14500, doi:10.1038/ncomms14500 (2017).

32 Muller, M. *et al.* Streptococcus thermophilus CRISPR-Cas9 Systems Enable Specific Editing of the Human Genome. *Molecular therapy : the journal of the American Society of Gene Therapy* **24**, 636-644, doi:10.1038/mt.2015.218 (2016).

33 Bin Moon, S. *et al.* Highly efficient genome editing by CRISPR-Cpf1 using CRISPR RNA with a uridinylate-rich 3'-overhang. *Nature communications* **9**, 3651, doi:10.1038/s41467-018-06129-w (2018).

34 Zhong, Z. *et al.* Plant Genome Editing Using FnCpf1 and LbCpf1 Nucleases at Redefined and Altered PAM Sites. *Mol Plant* **11**, 999-1002, doi:10.1016/j.molp.2018.03.008 (2018).

35 Lander, E. S. The Heroes of CRISPR. *Cell* **164**, 18-28, doi:10.1016/j.cell.2015.12.041 (2016).

36 Han, W. & She, Q. CRISPR History: Discovery, Characterization, and Prosperity. *Prog Mol Biol Transl Sci* **152**, 1-21, doi:10.1016/bs.pmbts.2017.10.001 (2017).

37 Feng, S. *et al.* Strategies for High-Efficiency Mutation Using the CRISPR/Cas System. *Front Cell Dev Biol* **9**, 803252, doi:10.3389/fcell.2021.803252 (2021).

38 Jiang, F. & Doudna, J. A. CRISPR-Cas9 Structures and Mechanisms. *Annu Rev Biophys* **46**, 505-529, doi:10.1146/annurev-biophys-062215-010822 (2017).

39 Chen, S., Lee, B., Lee, A. Y., Modzelewski, A. J. & He, L. Highly Efficient Mouse Genome Editing by CRISPR Ribonucleoprotein Electroporation of Zygotes. *The Journal of biological chemistry* **291**, 14457-14467, doi:10.1074/jbc.M116.733154 (2016).

40 Luther, D. C., Lee, Y. W., Nagaraj, H., Scaletti, F. & Rotello, V. M. Delivery approaches for CRISPR/Cas9 therapeutics *in vivo*: advances and challenges. *Expert Opin Drug Deliv* **15**, 905-913, doi:10.1080/17425247.2018.1517746 (2018).

41 Platt, R. J. *et al.* CRISPR-Cas9 knockin mice for genome editing and cancer modeling. *Cell* **159**, 440-455, doi:10.1016/j.cell.2014.09.014 (2014).

42 Kurata, M. *et al.* Highly multiplexed genome engineering using CRISPR/Cas9 gRNA arrays. *PloS one* **13**, e0198714, doi:10.1371/journal.pone.0198714 (2018).

43 Vakulskas, C. A. & Behlke, M. A. Evaluation and Reduction of CRISPR Off-Target Cleavage Events. *Nucleic acid therapeutics* **29**, 167-174, doi:10.1089/nat.2019.0790 (2019).

44 Fu, Y. *et al.* High-frequency off-target mutagenesis induced by CRISPR-Cas nucleases in human cells. *Nature biotechnology* **31**, 822-826, doi:10.1038/nbt.2623 (2013).

45 Zhang, Y., Iaffaldano, B. & Qi, Y. CRISPR ribonucleoprotein-mediated genetic engineering in plants. *Plant Commun* **2**, 100168, doi:10.1016/j.xplc.2021.100168 (2021).

46 Kim, S., Kim, D., Cho, S. W., Kim, J. & Kim, J. S. Highly efficient RNA-guided genome editing in human cells via delivery of purified Cas9 ribonucleoproteins. *Genome research* **24**, 1012-1019, doi:10.1101/gr.171322.113 (2014).

47 Ramakrishna, S. *et al.* Gene disruption by cell-penetrating peptide-mediated delivery of Cas9 protein and guide RNA. *Genome Res* **24**, 1020-1027, doi:10.1101/gr.171264.113 (2014).

48 Hong, S. *et al.* Protein-Based Nanoparticles as Drug Delivery Systems. *Pharmaceutics* **12**, doi:10.3390/pharmaceutics12070604 (2020).

49 Lin, Y., Wagner, E. & Lachelt, U. Non-viral delivery of the CRISPR/Cas system: DNA versus RNA versus RNP. *Biomater Sci* **10**, 1166-1192, doi:10.1039/d1bm01658j (2022).

50 Shen, B. *et al.* Generation of gene-modified mice via Cas9/RNA-mediated gene targeting. *Cell Res* **23**, 720-723, doi:10.1038/cr.2013.46 (2013).

51 Shen, B. *et al.* Efficient genome modification by CRISPR-Cas9 nickase with minimal off-target effects. *Nature methods* **11**, 399-402, doi:10.1038/nmeth.2857 (2014).

52 Auer, T. O., Duroure, K., De Cian, A., Concordet, J. P. & Del Bene, F. Highly efficient CRISPR/Cas9-mediated knock-in in zebrafish by homology-independent DNA repair. *Genome research* **24**, 142-153, doi:10.1101/gr.161638.113 (2014).

53 Yin, H. *et al.* Therapeutic genome editing by combined viral and non-viral delivery of CRISPR system components *in vivo*. *Nat Biotechnol* **34**, 328-333, doi:10.1038/nbt.3471 (2016).

54 Yin, H. *et al.* Structure-guided chemical modification of guide RNA enables potent non-viral *in vivo* genome editing. *Nature biotechnology* **35**, 1179-1187, doi:10.1038/nbt.4005

(2017).

55 Finn, J. D. *et al.* A Single Administration of CRISPR/Cas9 Lipid Nanoparticles Achieves Robust and Persistent *In vivo* Genome Editing. *Cell reports* **22**, 2227-2235, doi:10.1016/j.celrep.2018.02.014 (2018).

56 Li, D. F. *et al.* Nanomaterials for mRNA-based therapeutics: Challenges and opportunities. *Bioeng Transl Med* **8**, e10492, doi:10.1002/btm2.10492 (2023).

57 Cheng, F. *et al.* Research Advances on the Stability of mRNA Vaccines. *Viruses* **15**, doi:10.3390/v15030668 (2023).

58 Brenner, S., Jacob, F. & Meselson, M. An unstable intermediate carrying information from genes to ribosomes for protein synthesis. *Nature* **190**, 576-581, doi:10.1038/190576a0 (1961).

59 Sonneveld, S., Verhagen, B. M. P. & Tanenbaum, M. E. Heterogeneity in mRNA Translation. *Trends Cell Biol* **30**, 606-618, doi:10.1016/j.tcb.2020.04.008 (2020).

60 Gualerzi, C. O. & Pon, C. L. Initiation of mRNA translation in prokaryotes. *Biochemistry* **29**, 5881-5889, doi:10.1021/bi00477a001 (1990).

61 Faure, G., Ogurtsov, A. Y., Shabalina, S. A. & Koonin, E. V. Role of mRNA structure in the control of protein folding. *Nucleic Acids Res* **44**, 10898-10911, doi:10.1093/nar/gkw671 (2016).

62 Darnell, F. E. mRNA structure and function. *Prog Nucleic Acid Res Mol Biol* **19**, 493-511, doi:10.1016/s0079-6603(08)60941-1 (1976).

63 Dolgin, E. The tangled history of mRNA vaccines. *Nature* **597**, 318-324, doi:10.1038/d41586-021-02483-w (2021).

64 Malone, R. W., Felgner, P. L. & Verma, I. M. Cationic liposome-mediated RNA transfection. *Proc Natl Acad Sci U S A* **86**, 6077-6081, doi:10.1073/pnas.86.16.6077 (1989).

65 Wolff, J. A. *et al.* Direct gene transfer into mouse muscle *in vivo*. *Science* **247**, 1465-1468, doi:10.1126/science.1690918 (1990).

66 Huang, C. L. *et al.* Synthetic chemically modified mrna-based delivery of cytoprotective factor promotes early cardiomyocyte survival post-acute myocardial infarction. *Mol Pharm* **12**, 991-996, doi:10.1021/mp5006239 (2015).

67 Wadhwa, A., Aljabbari, A., Lokras, A., Foged, C. & Thakur, A. Opportunities and Challenges in the Delivery of mRNA-Based Vaccines. *Pharmaceutics* **12**, doi:10.3390/pharmaceutics12020102 (2020).

68 Parayath, N. N., Stephan, S. B., Koehne, A. L., Nelson, P. S. & Stephan, M. T. *In vitro*-transcribed antigen receptor mRNA nanocarriers for transient expression in circulating T cells *in vivo*. *Nat Commun* **11**, 6080, doi:10.1038/s41467-020-19486-2 (2020).

69 Zhang, X. *et al.* Biodegradable Amino-Ester Nanomaterials for Cas9 mRNA Delivery *in vitro* and *in vivo*. *ACS Appl Mater Interfaces* **9**, 25481-25487, doi:10.1021/acsami.7b08163 (2017).

70 Omstead, D. T. *et al. In vivo* evaluation of CD38 and CD138 as targets for nanoparticle-based drug delivery in multiple myeloma. *J Hematol Oncol* **13**, 145, doi:10.1186/s13045-020-00965-4 (2020).

71 Lokras, A. G., Bobak, T. R., Baghel, S. S., Sebastiani, F. & Foged, C. Advances in the design and delivery of RNA vaccines for infectious diseases. *Adv Drug Deliv Rev*, 115419, doi:10.1016/j.addr.2024.115419 (2024).

72 Qin, S. *et al.* mRNA-based therapeutics: powerful and versatile tools to combat diseases. *Signal Transduct Target Ther* **7**, 166, doi:10.1038/s41392-022-01007-w (2022).

73 Kwon, H. *et al.* Emergence of synthetic mRNA: *In vitro* synthesis of mRNA and its applications in regenerative medicine. *Biomaterials* **156**, 172-193, doi:10.1016/j.biomaterials.2017.11.034 (2018).

74 Kang, D. D., Li, H. & Dong, Y. Advancements of *in vitro* transcribed mRNA (IVT mRNA) to enable translation into the clinics. *Adv Drug Deliv Rev* **199**, 114961, doi:10.1016/j.addr.2023.114961 (2023).

75 Hinnebusch, A. G. Structural Insights into the Mechanism of Scanning and Start Codon Recognition in Eukaryotic Translation Initiation. *Trends Biochem Sci* **42**, 589-611, doi:10.1016/j.tibs.2017.03.004 (2017).

76 Bhat, M. *et al.* Targeting the translation machinery in cancer. *Nat Rev Drug Discov* **14**, 261-278, doi:10.1038/nrd4505 (2015).

77 Li, B., Luo, X. & Dong, Y. Effects of Chemically Modified Messenger RNA on Protein Expression. *Bioconjug Chem* **27**, 849-853, doi:10.1021/acs.bioconjchem.6b00090 (2016).

78 Melamed, J. R. *et al.* Lipid nanoparticle chemistry determines how nucleoside base modifications alter mRNA delivery. *J Control Release* **341**, 206-214, doi:10.1016/j.jconrel.2021.11.022 (2022).

79 Peng, Z. H., Sharma, V., Singleton, S. F. & Gershon, P. D. Synthesis and application of a chain-terminating dinucleotide mRNA cap analog. *Org Lett* **4**, 161-164, doi:10.1021/ol0167715 (2002).

80 Legnini, I., Alles, J., Karaiskos, N., Ayoub, S. & Rajewsky, N. FLAM-seq: full-length mRNA sequencing reveals principles of poly(A) tail length control. *Nat Methods* **16**, 879-886, doi:10.1038/s41592-019-0503-y (2019).

81 Jiang, Y., Xu, X. S. & Russell, J. E. A nucleolin-binding 3' untranslated region element stabilizes beta-globin mRNA *in vivo*. *Mol Cell Biol* **26**, 2419-2429, doi:10.1128/MCB.26.6.2419-2429.2006 (2006).

82 Zhang, Y. *et al.* Efficient signal sequence of mRNA vaccines enhances the antigen expression to expand the immune protection against viral infection. *J Nanobiotechnology* **22**, 295, doi:10.1186/s12951-024-02488-3 (2024).

83 Ramanathan, A., Robb, G. B. & Chan, S. H. mRNA capping: biological functions and applications. *Nucleic Acids Res* **44**, 7511-7526, doi:10.1093/nar/gkw551 (2016).

84 Kasprzyk, R. & Jemielity, J. Enzymatic Assays to Explore Viral mRNA Capping Machinery. *Chembiochem* **22**, 3236-3253, doi:10.1002/cbic.202100291 (2021).

85 Kuhn, A. N. *et al.* Phosphorothioate cap analogs increase stability and translational efficiency of RNA vaccines in immature dendritic cells and induce superior immune responses *in vivo*. *Gene Ther* **17**, 961-971, doi:10.1038/gt.2010.52 (2010).

86 Zhang, R., Qin, X., Kong, F., Chen, P. & Pan, G. Improving cellular uptake of therapeutic entities through interaction with components of cell membrane. *Drug Deliv* **26**, 328-342, doi:10.1080/10717544.2019.1582730 (2019).

87 Schott, J. W., Morgan, M., Galla, M. & Schambach, A. Viral and Synthetic RNA Vector Technologies and Applications. *Mol Ther* **24**, 1513-1527, doi:10.1038/mt.2016.143 (2016).

88 McLenachan, S., Zhang, D., Palomo, A. B., Edel, M. J. & Chen, F. K. mRNA transfection of mouse and human neural stem cell cultures. *PLoS One* **8**, e83596,

doi:10.1371/journal.pone.0083596 (2013).

89 Yang, W., Mixich, L., Boonstra, E. & Cabral, H. Polymer-Based mRNA Delivery Strategies for Advanced Therapies. *Adv Healthc Mater* **12**, e2202688, doi:10.1002/adhm.202202688 (2023).

90 Galla, M., Will, E., Kraunus, J., Chen, L. & Baum, C. Retroviral pseudotransduction for targeted cell manipulation. *Mol Cell* **16**, 309-315, doi:10.1016/j.molcel.2004.09.023 (2004).

91 Thomas, C. E., Ehrhardt, A. & Kay, M. A. Progress and problems with the use of viral vectors for gene therapy. *Nat Rev Genet* **4**, 346-358, doi:10.1038/nrg1066 (2003).

92 Dowdy, S. F. Endosomal escape of RNA therapeutics: How do we solve this rate-limiting problem? *RNA* **29**, 396-401, doi:10.1261/rna.079507.122 (2023).

93 Butt, A. M., Abdullah, N., Rani, N., Ahmad, N. & Amin, M. Endosomal Escape of Bioactives Deployed via Nanocarriers: Insights Into the Design of Polymeric Micelles. *Pharm Res* **39**, 1047-1064, doi:10.1007/s11095-022-03296-w (2022).

94 Varkouhi, A. K., Scholte, M., Storm, G. & Haisma, H. J. Endosomal escape pathways for delivery of biologicals. *J Control Release* **151**, 220-228, doi:10.1016/j.jconrel.2010.11.004 (2011).

95 Lin, C. & Engbersen, J. F. Effect of chemical functionalities in poly(amido amine)s for non-viral gene transfection. *J Control Release* **132**, 267-272, doi:10.1016/j.jconrel.2008.06.022 (2008).

96 Huang, H. W., Chen, F. Y. & Lee, M. T. Molecular mechanism of Peptide-induced pores in membranes. *Phys Rev Lett* **92**, 198304, doi:10.1103/PhysRevLett.92.198304 (2004).

97 White, J. M. & Whittaker, G. R. Fusion of Enveloped Viruses in Endosomes. *Traffic* **17**, 593-614, doi:10.1111/tra.12389 (2016).

98 Butt, M. H. *et al.* Appraisal for the Potential of Viral and Nonviral Vectors in Gene Therapy: A Review. *Genes (Basel)* **13**, doi:10.3390/genes13081370 (2022).

99 Wang, C. *et al.* Emerging non-viral vectors for gene delivery. *J Nanobiotechnology* **21**, 272, doi:10.1186/s12951-023-02044-5 (2023).

100 Abbasi, S. *et al.* Co-encapsulation of Cas9 mRNA and guide RNA in polyplex micelles enables genome editing in mouse brain. *J Control Release* **332**, 260-268, doi:10.1016/j.jconrel.2021.02.026 (2021).

101 Kenjo, E. *et al.* Low immunogenicity of LNP allows repeated administrations of CRISPR-Cas9 mRNA into skeletal muscle in mice. *Nat Commun* **12**, 7101, doi:10.1038/s41467-021-26714-w (2021).

102 Usman, W. M. *et al.* Efficient RNA drug delivery using red blood cell extracellular vesicles. *Nat Commun* **9**, 2359, doi:10.1038/s41467-018-04791-8 (2018).

103 Hasanzadeh, A. *et al.* Highly Photoluminescent Nitrogen- and Zinc-Doped Carbon Dots for Efficient Delivery of CRISPR/Cas9 and mRNA. *Bioconjug Chem* **32**, 1875-1887, doi:10.1021/acs.bioconjchem.1c00309 (2021).

104 Timin, A. S. *et al.* Efficient gene editing via non-viral delivery of CRISPR-Cas9 system using polymeric and hybrid microcarriers. *Nanomedicine* **14**, 97-108, doi:10.1016/j.nano.2017.09.001 (2018).

105 Feng, Y. *et al.* Cationic polymer synergizing with a disulfide-containing enhancer achieved efficient nucleic acid and protein delivery. *Biomater Sci* **10**, 6230-6243,

doi:10.1039/d2bm01211a (2022).

106 Crane, R. *et al.* Effective intravitreal gene delivery to retinal pigment epithelium with hyaluronic acid nanospheres. *Mol Ther Nucleic Acids* **35**, 102222, doi:10.1016/j.omtn.2024.102222 (2024).

107 Adams, F. *et al.* Pulmonary siRNA Delivery with Sophisticated Amphiphilic Poly(Spermine Acrylamides) for the Treatment of Lung Fibrosis. *Small* **20**, e2308775, doi:10.1002/smll.202308775 (2024).

108 Jin, Y. *et al.* Synthesis and application of spermine-based amphiphilic poly(beta-amino ester)s for siRNA delivery. *Nanoscale Adv* **5**, 5256-5262, doi:10.1039/d3na00272a (2023).

109 Greco, A. *et al.* Microfluidic mixing as platform technology for production of chitosan nanoparticles loaded with different macromolecules. *Eur J Pharm Biopharm* **188**, 170-181, doi:10.1016/j.ejpb.2023.05.010 (2023).

110 Roberts, T. C., Langer, R. & Wood, M. J. A. Advances in oligonucleotide drug delivery. *Nat Rev Drug Discov* **19**, 673-694, doi:10.1038/s41573-020-0075-7 (2020).

111 Mueller, M., Reichardt, W., Koerner, J. & Groettrup, M. Coencapsulation of tumor lysate and CpG-ODN in PLGA-microspheres enables successful immunotherapy of prostate carcinoma in TRAMP mice. *J Control Release* **162**, 159-166, doi:10.1016/j.jconrel.2012.06.015 (2012).

112 Zhang, S., Shen, J., Li, D. & Cheng, Y. Strategies in the delivery of Cas9 ribonucleoprotein for CRISPR/Cas9 genome editing. *Theranostics* **11**, 614-648, doi:10.7150/thno.47007 (2021).

113 Lu, X. Y., Wu, D. C., Li, Z. J. & Chen, G. Q. Polymer nanoparticles. *Prog Mol Biol Transl Sci* **104**, 299-323, doi:10.1016/B978-0-12-416020-0.00007-3 (2011).

114 Kretzmann, J. A. *et al.* Synthetically controlling dendrimer flexibility improves delivery of large plasmid DNA. *Chem Sci* **8**, 2923-2930, doi:10.1039/c7sc00097a (2017).

115 Liu, Y. *et al.* Systemic delivery of CRISPR/Cas9 with PEG-PLGA nanoparticles for chronic myeloid leukemia targeted therapy. *Biomater Sci* **6**, 1592-1603, doi:10.1039/c8bm00263k (2018).

116 Kang, Y. K. *et al.* Nonviral Genome Editing Based on a Polymer-Derivatized CRISPR Nanocomplex for Targeting Bacterial Pathogens and Antibiotic Resistance. *Bioconjug Chem* **28**, 957-967, doi:10.1021/acs.bioconjchem.6b00676 (2017).

117 Qiao, J. *et al.* Cytosolic delivery of CRISPR/Cas9 ribonucleoproteins for genome editing using chitosan-coated red fluorescent protein. *Chem Commun (Camb)* **55**, 4707-4710, doi:10.1039/c9cc00010k (2019).

118 Blanchard, E. L. *et al.* Treatment of influenza and SARS-CoV-2 infections via mRNA-encoded Cas13a in rodents. *Nat Biotechnol* **39**, 717-726, doi:10.1038/s41587-021-00822-w (2021).

119 Yip, B. H. Recent Advances in CRISPR/Cas9 Delivery Strategies. *Biomolecules* **10**, doi:10.3390/biom10060839 (2020).

120 Zong, Y., Lin, Y., Wei, T. & Cheng, Q. Lipid Nanoparticle (LNP) Enables mRNA Delivery for Cancer Therapy. *Adv Mater* **35**, e2303261, doi:10.1002/adma.202303261 (2023).

121 Rosenblum, D. *et al.* CRISPR-Cas9 genome editing using targeted lipid nanoparticles for cancer therapy. *Sci Adv* **6**, doi:10.1126/sciadv.abc9450 (2020).

122 Xue, L. *et al.* High-throughput barcoding of nanoparticles identifies cationic, degradable

lipid-like materials for mRNA delivery to the lungs in female preclinical models. *Nat Commun* **15**, 1884, doi:10.1038/s41467-024-45422-9 (2024).

123 Mitchell, M. J. *et al.* Engineering precision nanoparticles for drug delivery. *Nat Rev Drug Discov* **20**, 101-124, doi:10.1038/s41573-020-0090-8 (2021).

124 Jose, C., Amra, K., Bhavsar, C., Momin, M. & Omri, A. Polymeric Lipid Hybrid Nanoparticles: Properties and Therapeutic Applications. *Crit Rev Ther Drug Carrier Syst* **35**, 555-588, doi:10.1615/CritRevTherDrugCarrierSyst.2018024751 (2018).

125 Dilliard, S. A. & Siegwart, D. J. Passive, active and endogenous organ-targeted lipid and polymer nanoparticles for delivery of genetic drugs. *Nat Rev Mater* **8**, 282-300, doi:10.1038/s41578-022-00529-7 (2023).

126 Jeppesen, D. K., Zhang, Q., Franklin, J. L. & Coffey, R. J. Extracellular vesicles and nanoparticles: emerging complexities. *Trends Cell Biol* **33**, 667-681, doi:10.1016/j.tcb.2023.01.002 (2023).

127 Meng, W. *et al.* Prospects and challenges of extracellular vesicle-based drug delivery system: considering cell source. *Drug Deliv* **27**, 585-598, doi:10.1080/10717544.2020.1748758 (2020).

128 Dow, L. E. Modeling Disease *In vivo* With CRISPR/Cas9. *Trends in molecular medicine* **21**, 609-621, doi:10.1016/j.molmed.2015.07.006 (2015).

129 Zuckermann, M. *et al.* Somatic CRISPR/Cas9-mediated tumour suppressor disruption enables versatile brain tumour modelling. *Nature communications* **6**, 7391, doi:10.1038/ncomms8391 (2015).

130 Hai, T., Teng, F., Guo, R., Li, W. & Zhou, Q. One-step generation of knockout pigs by zygote injection of CRISPR/Cas system. *Cell research* **24**, 372-375, doi:10.1038/cr.2014.11 (2014).

131 Zou, Q. *et al.* Generation of gene-target dogs using CRISPR/Cas9 system. *Journal of molecular cell biology* **7**, 580-583, doi:10.1093/jmcb/mjv061 (2015).

132 Niu, Y. *et al.* Generation of gene-modified cynomolgus monkey via Cas9/RNA-mediated gene targeting in one-cell embryos. *Cell* **156**, 836-843, doi:10.1016/j.cell.2014.01.027 (2014).

133 Konishi, C. T. & Long, C. Progress and challenges in CRISPR-mediated therapeutic genome editing for monogenic diseases. *Journal of biomedical research* **35**, 148-162, doi:10.7555/JBR.34.20200105 (2020).

134 Alapati, D. & Morrisey, E. E. Gene Editing and Genetic Lung Disease. Basic Research Meets Therapeutic Application. *American journal of respiratory cell and molecular biology* **56**, 283-290, doi:10.1165/rcmb.2016-0301PS (2017).

135 Alapati, D. *et al.* In utero gene editing for monogenic lung disease. *Science translational medicine* **11**, doi:10.1126/scitranslmed.aav8375 (2019).

136 Jo, D. H. *et al.* CRISPR-Cas9-mediated therapeutic editing of Rpe65 ameliorates the disease phenotypes in a mouse model of Leber congenital amaurosis. *Science advances* **5**, eaax1210, doi:10.1126/sciadv.aax1210 (2019).

137 Yang, Y. *et al.* A dual AAV system enables the Cas9-mediated correction of a metabolic liver disease in newborn mice. *Nature biotechnology* **34**, 334-338, doi:10.1038/nbt.3469 (2016).

138 Roman-Rodriguez, F. J. *et al.* NHEJ-Mediated Repair of CRISPR-Cas9-Induced DNA

Breaks Efficiently Corrects Mutations in HSPCs from Patients with Fanconi Anemia. *Cell stem cell* **25**, 607-621 e607, doi:10.1016/j.stem.2019.08.016 (2019).

139 Perez-Arancibia, R., Cisternas-Olmedo, M., Sepulveda, D., Troncoso-Escudero, P. & Vidal, R. L. Small molecules to perform big roles: The search for Parkinson's and Huntington's disease therapeutics. *Front Neurosci* **16**, 1084493, doi:10.3389/fnins.2022.1084493 (2022).

140 Masoudi Asil, S., Ahlawat, J., Guillama Barroso, G. & Narayan, M. Nanomaterial based drug delivery systems for the treatment of neurodegenerative diseases. *Biomater Sci* **8**, 4109-4128, doi:10.1039/d0bm00809e (2020).

141 Kuruvilla, J., Sasmita, A. O. & Ling, A. P. K. Therapeutic potential of combined viral transduction and CRISPR/Cas9 gene editing in treating neurodegenerative diseases. *Neurological sciences : official journal of the Italian Neurological Society and of the Italian Society of Clinical Neurophysiology* **39**, 1827-1835, doi:10.1007/s10072-018-3521-0 (2018).

142 Rohn, T. T., Kim, N., Isho, N. F. & Mack, J. M. The Potential of CRISPR/Cas9 Gene Editing as a Treatment Strategy for Alzheimer's Disease. *Journal of Alzheimer's disease & Parkinsonism* **8**, doi:10.4172/2161-0460.1000439 (2018).

143 Gyorgy, B. *et al.* CRISPR/Cas9 Mediated Disruption of the Swedish APP Allele as a Therapeutic Approach for Early-Onset Alzheimer's Disease. *Molecular therapy. Nucleic acids* **11**, 429-440, doi:10.1016/j.omtn.2018.03.007 (2018).

144 Pahan, K. A Broad Application of CRISPR Cas9 in Infectious, Inflammatory and Neurodegenerative Diseases. *Journal of neuroimmune pharmacology : the official journal of the Society on NeuroImmune Pharmacology* **14**, 534-536, doi:10.1007/s11481-019-09889-4 (2019).

145 Safari, F. *et al.* CRISPR System: A High-throughput Toolbox for Research and Treatment of Parkinson's Disease. *Cellular and molecular neurobiology* **40**, 477-493, doi:10.1007/s10571-019-00761-w (2020).

146 Inoue, N. *et al.* Knockdown of the mitochondria-localized protein p13 protects against experimental parkinsonism. *EMBO reports* **19**, doi:10.15252/embr.201744860 (2018).

147 Chen, M. *et al.* CRISPR-Cas9 for cancer therapy: Opportunities and challenges. *Cancer letters* **447**, 48-55, doi:10.1016/j.canlet.2019.01.017 (2019).

148 Bannister, A. J. & Kouzarides, T. Regulation of chromatin by histone modifications. *Cell Res* **21**, 381-395, doi:10.1038/cr.2011.22 (2011).

149 Khan, F. A. *et al.* CRISPR/Cas9 therapeutics: a cure for cancer and other genetic diseases. *Oncotarget* **7**, 52541-52552, doi:10.18632/oncotarget.9646 (2016).

150 Anastas, J. N. *et al.* Re-programing Chromatin with a Bifunctional LSD1/HDAC Inhibitor Induces Therapeutic Differentiation in DIPG. *Cancer cell* **36**, 528-544 e510, doi:10.1016/j.ccell.2019.09.005 (2019).

151 Yang, J. *et al.* CRISPR/Cas9-mediated noncoding RNA editing in human cancers. *RNA biology* **15**, 35-43, doi:10.1080/15476286.2017.1391443 (2018).

152 Zhou, S. J., Deng, Y. L., Liang, H. F., Jaoude, J. C. & Liu, F. Y. Hepatitis B virus X protein promotes CREB-mediated activation of miR-3188 and Notch signaling in hepatocellular carcinoma. *Cell death and differentiation* **24**, 1577-1587, doi:10.1038/cdd.2017.87 (2017).

153 Yu, Y., Nangia-Makker, P., Farhana, L. & Majumdar, A. P. N. A novel mechanism of lncRNA and miRNA interaction: CCAT2 regulates miR-145 expression by suppressing its

maturation process in colon cancer cells. *Molecular cancer* **16**, 155, doi:10.1186/s12943-017-0725-5 (2017).

154 Lee, E. Y. & Muller, W. J. Oncogenes and tumor suppressor genes. *Cold Spring Harb Perspect Biol* **2**, a003236, doi:10.1101/cshperspect.a003236 (2010).

155 Ferro, A. *et al.* The study of primary and acquired resistance to first-line osimertinib to improve the outcome of EGFR-mutated advanced Non-small cell lung cancer patients: the challenge is open for new therapeutic strategies. *Crit Rev Oncol Hematol* **196**, 104295, doi:10.1016/j.critrevonc.2024.104295 (2024).

156 Koo, T. *et al.* Selective disruption of an oncogenic mutant allele by CRISPR/Cas9 induces efficient tumor regression. *Nucleic acids research* **45**, 7897-7908, doi:10.1093/nar/gkx490 (2017).

157 Huang, L., Guo, Z., Wang, F. & Fu, L. KRAS mutation: from undruggable to druggable in cancer. *Signal Transduct Target Ther* **6**, 386, doi:10.1038/s41392-021-00780-4 (2021).

158 Kim, W. *et al.* Targeting mutant KRAS with CRISPR-Cas9 controls tumor growth. *Genome research*, doi:10.1101/gr.223891.117 (2018).

159 Jiang, C., Lin, X. & Zhao, Z. Applications of CRISPR/Cas9 Technology in the Treatment of Lung Cancer. *Trends in molecular medicine* **25**, 1039-1049, doi:10.1016/j.molmed.2019.07.007 (2019).

160 Chen, X. *et al.* Rsf-1 Influences the Sensitivity of Non-Small Cell Lung Cancer to Paclitaxel by Regulating NF-kappaB Pathway and Its Downstream Proteins. *Cellular physiology and biochemistry : international journal of experimental cellular physiology, biochemistry, and pharmacology* **44**, 2322-2336, doi:10.1159/000486116 (2017).

161 Khoshandam, M., Soltaninejad, H., Mousazadeh, M., Hamidieh, A. A. & Hosseinkhani, S. Clinical applications of the CRISPR/Cas9 genome-editing system: Delivery options and challenges in precision medicine. *Genes Dis* **11**, 268-282, doi:10.1016/j.gendis.2023.02.027 (2024).

162 Yi, M. *et al.* Exploiting innate immunity for cancer immunotherapy. *Mol Cancer* **22**, 187, doi:10.1186/s12943-023-01885-w (2023).

163 Dimitri, A., Herbst, F. & Fraietta, J. A. Engineering the next-generation of CAR T-cells with CRISPR-Cas9 gene editing. *Mol Cancer* **21**, 78, doi:10.1186/s12943-022-01559-z (2022).

164 Ren, J. *et al.* Multiplex Genome Editing to Generate Universal CAR T Cells Resistant to PD1 Inhibition. *Clinical cancer research : an official journal of the American Association for Cancer Research* **23**, 2255-2266, doi:10.1158/1078-0432.CCR-16-1300 (2017).

165 Valenti, M. T., Serena, M., Carbonare, L. D. & Zipeto, D. CRISPR/Cas system: An emerging technology in stem cell research. *World J Stem Cells* **11**, 937-956, doi:10.4252/wjsc.v11.i11.937 (2019).

166 Kerwash, E. & Johnston, J. D. Casgevy: Innovative Medicinal Products Require Innovative Approaches to Regulatory Assessment. *Pharmaceutics* **16**, doi:10.3390/pharmaceutics16070906 (2024).

167 Singh, A. *et al.* Revolutionary breakthrough: FDA approves CASGEVY, the first CRISPR/Cas9 gene therapy for sickle cell disease. *Ann Med Surg (Lond)* **86**, 4555-4559, doi:10.1097/MS9.0000000000002146 (2024).

168 Lovell-Badge, R. CRISPR babies: a view from the centre of the storm. *Development* **146**, doi:10.1242/dev.175778 (2019).

169 Zhang, W. W. *et al.* A second generation leishmanization vaccine with a markerless attenuated Leishmania major strain using CRISPR gene editing. *Nat Commun* **11**, 3461, doi:10.1038/s41467-020-17154-z (2020).

170 Terrett, J. A. *et al.* Abstract ND02: CTX112 and CTX131: Next-generation CRISPR/Cas9-engineered allogeneic (allo) CAR T cells incorporating novel edits that increase potency and efficacy in the treatment of lymphoid and solid tumors. *Cancer Research* **83**, ND02-ND02, doi:10.1158/1538-7445.AM2023-ND02 (2023).

171 Wei, A. *et al. In vivo* CRISPR gene editing in patients with herpetic stromal keratitis. *Mol Ther* **31**, 3163-3175, doi:10.1016/j.ymthe.2023.08.021 (2023).

172 Gillmore, J. D. *et al.* CRISPR-Cas9 *In vivo* Gene Editing for Transthyretin Amyloidosis. *N Engl J Med* **385**, 493-502, doi:10.1056/NEJMoa2107454 (2021).

173 Salgia, R., Pharaon, R., Mambetsariev, I., Nam, A. & Sattler, M. The improbable targeted therapy: KRAS as an emerging target in non-small cell lung cancer (NSCLC). *Cell Rep Med* **2**, 100186, doi:10.1016/j.xcrm.2020.100186 (2021).

174 Singhal, A., Li, B. T. & O'Reilly, E. M. Targeting KRAS in cancer. *Nat Med* **30**, 969-983, doi:10.1038/s41591-024-02903-0 (2024).

175 Chen, Y., Liu, Q. P., Xie, H. & Ding, J. From bench to bedside: current development and emerging trend of KRAS-targeted therapy. *Acta Pharmacol Sin* **45**, 686-703, doi:10.1038/s41401-023-01194-4 (2024).

176 Saw, P. E. & Song, E. Advancements in clinical RNA therapeutics: Present developments and prospective outlooks. *Cell Rep Med* **5**, 101555, doi:10.1016/j.xcrm.2024.101555 (2024).

177 Walther, J. *et al.* Comparative analysis of lipid Nanoparticle-Mediated delivery of CRISPR-Cas9 RNP versus mRNA/sgRNA for gene editing *in vitro* and *in vivo*. *Eur J Pharm Biopharm* **196**, 114207, doi:10.1016/j.ejpb.2024.114207 (2024).

178 Parhiz, H., Atochina-Vasserman, E. N. & Weissman, D. mRNA-based therapeutics: looking beyond COVID-19 vaccines. *Lancet* **403**, 1192-1204, doi:10.1016/S0140-6736(23)02444-3 (2024).

179 Yue, H., Zhou, X., Cheng, M. & Xing, D. Graphene oxide-mediated Cas9/sgRNA delivery for efficient genome editing. *Nanoscale* **10**, 1063-1071, doi:10.1039/c7nr07999k (2018).

180 Dahlman, J. E. *et al. In vivo* endothelial siRNA delivery using polymeric nanoparticles with low molecular weight. *Nat Nanotechnol* **9**, 648-655, doi:10.1038/nnano.2014.84 (2014).

181 Lin, Y.-X. *et al.* Reactivation of the tumor suppressor PTEN by mRNA nanoparticles enhances antitumor immunity in preclinical models. *Sci Transl Med.* **13**, doi:10.1126/scitranslmed.aba9772 (2021).

182 Basu Ray, G., Chakraborty, I. & Moulik, S. P. Pyrene absorption can be a convenient method for probing critical micellar concentration (cmc) and indexing micellar polarity. *Journal of Colloid and Interface Science* **294**, 248-254, doi:10.1016/j.jcis.2005.07.006 (2006).

183 Jin, Y. *et al.* Role of Hydrophobic Modification in Spermine-Based Poly(β-amino ester)s for siRNA Delivery and Their Spray-Dried Powders for Inhalation and Improved Storage. *Biomacromolecules*, doi:10.1021/acs.biomac.4c00283 (2024).

184 Jin, Y. *et al.* Synthesis and Application of Low Molecular Weight PEI-Based Copolymers for siRNA Delivery with Smart Polymer Blends. *Macromolecular Bioscience* **23**,

doi:10.1002/mabi.202200409 (2022).

185 Miyaoka, Y. *et al.* Systematic quantification of HDR and NHEJ reveals effects of locus, nuclease, and cell type on genome-editing. *Sci Rep* **6**, 23549, doi:10.1038/srep23549 (2016).

186 Conant, D. *et al.* Inference of CRISPR Edits from Sanger Trace Data. *Crispr j* **5**, 123-130, doi:10.1089/crispr.2021.0113 (2022).

187 Misale, S. *et al.* KRAS G12C NSCLC Models Are Sensitive to Direct Targeting of KRAS in Combination with PI3K Inhibition. *Clin Cancer Res* **25**, 796-807, doi:10.1158/1078-0432.CCR-18-0368 (2019).

188 Czyrnik, E. D., Wiesehofer, M., Dankert, J. T. & Wennemuth, G. The regulation of HAS3 by miR-10b and miR-29a in neuroendocrine transdifferentiated LNCaP prostate cancer cells. *Biochem Biophys Res Commun* **523**, 713-718, doi:10.1016/j.bbrc.2020.01.026 (2020).

189 Mehta, A., Dalle Vedove, E., Isert, L. & Merkel, O. M. Targeting KRAS Mutant Lung Cancer Cells with siRNA-Loaded Bovine Serum Albumin Nanoparticles. *Pharm Res* **36**, 133, doi:10.1007/s11095-019-2665-9 (2019).

190 Han, X. *et al.* An ionizable lipid toolbox for RNA delivery. *Nat Commun* **12**, 7233, doi:10.1038/s41467-021-27493-0 (2021).

191 Nemeth, Z. *et al.* Quality by Design-Driven Zeta Potential Optimisation Study of Liposomes with Charge Imparting Membrane Additives. *Pharmaceutics* **14**, doi:10.3390/pharmaceutics14091798 (2022).

192 Verma, A. & Stellacci, F. Effect of surface properties on nanoparticle-cell interactions. *Small* **6**, 12-21, doi:10.1002/smll.200901158 (2010).

193 Cheng, M. H. Y. *et al.* Induction of Bleb Structures in Lipid Nanoparticle Formulations of mRNA Leads to Improved Transfection Potency. *Adv Mater* **35**, e2303370, doi:10.1002/adma.202303370 (2023).

194 Hartl, N. *et al.* The Impact of Nylon-3 Copolymer Composition on the Efficiency of siRNA Delivery to Glioblastoma Cells. *Nanomaterials (Basel)* **9**, doi:10.3390/nano9070986 (2019).

195 Liu, L. *et al.* Efficient and Tumor Targeted siRNA Delivery by Polyethylenimine-graft-polycaprolactone-block-poly(ethylene glycol)-folate (PEI-PCL-PEG-Fol). *Mol Pharm* **13**, 134-143, doi:10.1021/acs.molpharmaceut.5b00575 (2016).

196 Gwak, S.-J., Macks, C., Bae, S., Cecil, N. & Lee, J. S. Physicochemical stability and transfection efficiency of cationic amphiphilic copolymer/pDNA polyplexes for spinal cord injury repair. *Scientific Reports* **7**, 11247, doi:10.1038/s41598-017-10982-y (2017).

197 Berger, S., Lächelt, U. & Wagner, E. Dynamic carriers for therapeutic RNA delivery. *Proceedings of the National Academy of Sciences* **121**, e2307799120, doi:doi:10.1073/pnas.2307799120 (2024).

198 Chen, J. *et al.* Cationic nanoparticles induce nanoscale disruption in living cell plasma membranes. *J Phys Chem B* **113**, 11179-11185, doi:10.1021/jp9033936 (2009).

199 Salatin, S. & Yari Khosroushahi, A. Overviews on the cellular uptake mechanism of polysaccharide colloidal nanoparticles. *J Cell Mol Med* **21**, 1668-1686, doi:10.1111/jcmm.13110 (2017).

200 Lee, P. Y., Costumbrado, J., Hsu, C. Y. & Kim, Y. H. Agarose gel electrophoresis for the separation of DNA fragments. *J Vis Exp*, doi:10.3791/3923 (2012).

201 Centelles, M. N., Qian, C., Campanero, M. A. & Irache, J. M. New methodologies to

characterize the effectiveness of the gene transfer mediated by DNA-chitosan nanoparticles. *Int J Nanomedicine* **3**, 451-460, doi:10.2147/ijn.s3445 (2008).

202 Gao, Q. *et al.* Selective targeting of the oncogenic KRAS G12S mutant allele by CRISPR/Cas9 induces efficient tumor regression. *Theranostics* **10**, 5137-5153, doi:10.7150/thno.42325 (2020).

203 Lin, Y. *et al.* Folate Receptor-Mediated Delivery of Cas9 RNP for Enhanced Immune Checkpoint Disruption in Cancer Cells. *Small* **19**, e2205318, doi:10.1002/smll.202205318 (2023).

204 Zhang, J. P. *et al.* Curing hemophilia A by NHEJ-mediated ectopic F8 insertion in the mouse. *Genome Biol* **20**, 276, doi:10.1186/s13059-019-1907-9 (2019).

205 Sentmanat, M. F., Peters, S. T., Florian, C. P., Connelly, J. P. & Pruett-Miller, S. M. A Survey of Validation Strategies for CRISPR-Cas9 Editing. *Scientific Reports* **8**, 888, doi:10.1038/s41598-018-19441-8 (2018).

206 Sansbury, B. M., Hewes, A. M. & Kmiec, E. B. Understanding the diversity of genetic outcomes from CRISPR-Cas generated homology-directed repair. *Communications Biology* **2**, 458, doi:10.1038/s42003-019-0705-y (2019).

207 Hunter, J. C. *et al.* Biochemical and Structural Analysis of Common Cancer-Associated KRAS Mutations. *Mol Cancer Res* **13**, 1325-1335, doi:10.1158/1541-7786.MCR-15-0203 (2015).

208 Simanshu, D. K., Nissley, D. V. & McCormick, F. RAS Proteins and Their Regulators in Human Disease. *Cell* **170**, 17-33, doi:10.1016/j.cell.2017.06.009 (2017).

209 Hunter, T. Signaling--2000 and beyond. *Cell* **100**, 113-127, doi:10.1016/s0092-8674(00)81688-8 (2000).

210 Wang, T., Larcher, L. M., Ma, L. & Veedu, R. N. Systematic Screening of Commonly Used Commercial Transfection Reagents towards Efficient Transfection of Single-Stranded Oligonucleotides. *Molecules* **23**, doi:10.3390/molecules23102564 (2018).

211 Li, Y. R. *et al.* Advancements in CRISPR screens for the development of cancer immunotherapy strategies. *Mol Ther Oncolytics* **31**, 100733, doi:10.1016/j.omto.2023.100733 (2023).

212 Peng, J. Gene redundancy and gene compensation: An updated view. *J Genet Genomics* **46**, 329-333, doi:10.1016/j.jgg.2019.07.001 (2019).

213 Zhao, X. *et al.* A CRISPR-Cas13a system for efficient and specific therapeutic targeting of mutant KRAS for pancreatic cancer treatment. *Cancer Lett* **431**, 171-181, doi:10.1016/j.canlet.2018.05.042 (2018).

214 Kim, W. *et al.* Targeting mutant KRAS with CRISPR-Cas9 controls tumor growth. *Genome Research* **28**, 374-382, doi:10.1101/gr.223891.117 (2018).

215 Feng, Q. *et al.* CRISPR technology in human diseases. *MedComm (2020)* **5**, e672, doi:10.1002/mco2.672 (2024).

216 Shalem, O. *et al.* Genome-scale CRISPR-Cas9 knockout screening in human cells. *Science* **343**, 84-87, doi:10.1126/science.1247005 (2014).

217 Lee, K. *et al.* Nanoparticle delivery of Cas9 ribonucleoprotein and donor DNA *in vivo* induces homology-directed DNA repair. *Nat Biomed Eng* **1**, 889-901, doi:10.1038/s41551-017-0137-2 (2017).

218 Yousefi Adlsadabad, S., Hanrahan, J. W. & Kakkar, A. mRNA Delivery: Challenges and

Advances through Polymeric Soft Nanoparticles. *Int J Mol Sci* **25**, doi:10.3390/ijms25031739 (2024).

219 Lv, H., Zhang, S., Wang, B., Cui, S. & Yan, J. Toxicity of cationic lipids and cationic polymers in gene delivery. *J Control Release* **114**, 100-109, doi:10.1016/j.jconrel.2006.04.014 (2006).

220 Bettinger, T., Carlisle, R. C., Read, M. L., Ogris, M. & Seymour, L. W. Peptide-mediated RNA delivery: a novel approach for enhanced transfection of primary and post-mitotic cells. *Nucleic Acids Res* **29**, 3882-3891, doi:10.1093/nar/29.18.3882 (2001).

221 Jiang, Z. & Thayumanavan, S. Non-cationic Material Design for Nucleic Acid Delivery. *Adv Ther (Weinh)* **3**, doi:10.1002/adtp.201900206 (2020).

222 D'Souza A, A. & Shegokar, R. Polyethylene glycol (PEG): a versatile polymer for pharmaceutical applications. *Expert Opin Drug Deliv* **13**, 1257-1275, doi:10.1080/17425247.2016.1182485 (2016).

223 Johnston, B. M., Grodzinsky, A. J. & Hammond, P. T. Charge shielding effects of PEG bound to NH(2)-terminated PAMAM dendrimers - an experimental approach. *Soft Matter* **19**, 3033-3046, doi:10.1039/d2sm01698b (2023).

224 Ke, X. *et al.* Surface-Functionalized PEGylated Nanoparticles Deliver Messenger RNA to Pulmonary Immune Cells. *ACS Appl Mater Interfaces* **12**, 35835-35844, doi:10.1021/acsami.0c08268 (2020).

225 Yin, J. *et al.* Negatively charged polymer-shielded supramolecular nano-micelles with stimuli-responsive property for anticancer drug delivery. *Int J Pharm* **627**, 122211, doi:10.1016/j.ijpharm.2022.122211 (2022).

226 Pan, D. *et al.* PEGylated dendritic diaminocyclohexyl-platinum (II) conjugates as pH-responsive drug delivery vehicles with enhanced tumor accumulation and antitumor efficacy. *Biomaterials* **35**, 10080-10092, doi:10.1016/j.biomaterials.2014.09.006 (2014).

227 Pontes, A. P. *et al.* A poly(amidoamine)-based polymeric nanoparticle platform for efficient *in vivo* delivery of mRNA. *Biomater Adv* **156**, 213713, doi:10.1016/j.bioadv.2023.213713 (2024).

228 Vestad, B. *et al.* Size and concentration analyses of extracellular vesicles by nanoparticle tracking analysis: a variation study. *J Extracell Vesicles* **6**, 1344087, doi:10.1080/20013078.2017.1344087 (2017).

229 Clogston, J. D. & Patri, A. K. Zeta potential measurement. *Methods Mol Biol* **697**, 63-70, doi:10.1007/978-1-60327-198-1_6 (2011).

230 Nobbmann, U. & Morfesis, A. Characterization of Nanoparticles by Light Scattering. *MRS Proceedings* **1074**, 1074-I1010-1045, doi:10.1557/PROC-1074-I10-45 (2008).

231 Chan, M. Y., Dowling, Q. M., Sivananthan, S. J. & Kramer, R. M. Particle Sizing of Nanoparticle Adjuvant Formulations by Dynamic Light Scattering (DLS) and Nanoparticle Tracking Analysis (NTA). *Methods Mol Biol* **1494**, 239-252, doi:10.1007/978-1-4939-6445-1_17 (2017).

232 Wang, C. *et al.* Quantitative measurement of aggregation kinetics process of nanoparticles using nanoparticle tracking analysis and dynamic light scattering. *Journal of Nanoparticle Research* **21**, 87, doi:10.1007/s11051-019-4527-0 (2019).

233 Fischer, D., Li, Y., Ahlemeyer, B., Krieglstein, J. & Kissel, T. *In vitro* cytotoxicity testing of polycations: influence of polymer structure on cell viability and hemolysis. *Biomaterials* **24**, 1121-1131, doi:10.1016/s0142-9612(02)00445-3 (2003).

234 Rejman, J., Bragonzi, A. & Conese, M. Role of clathrin- and caveolae-mediated endocytosis in gene transfer mediated by lipo- and polyplexes. *Mol Ther* **12**, 468-474, doi:10.1016/j.ymthe.2005.03.038 (2005).

235 Ostróżka-Cieślik, A. & Sarecka-Hujar, B. in *Multifunctional Systems for Combined Delivery, Biosensing and Diagnostics* (ed Alexandru Mihai Grumezescu) 139-158 (Elsevier, 2017).

236 Yang, W. *et al.* Controlling Nanoparticle Uptake in Innate Immune Cells with Heparosan Polysaccharides. *Nano Lett* **22**, 7119-7128, doi:10.1021/acs.nanolett.2c02226 (2022).

237 Dalal, C., Saha, A. & Jana, N. R. Nanoparticle Multivalency Directed Shifting of Cellular Uptake Mechanism. *The Journal of Physical Chemistry C* **120**, 6778-6786, doi:10.1021/acs.jpcc.5b11059 (2016).

238 Ivanov, A. I. Pharmacological inhibition of endocytic pathways: is it specific enough to be useful? *Methods Mol Biol* **440**, 15-33, doi:10.1007/978-1-59745-178-9_2 (2008).

239 Wang, L. H., Rothberg, K. G. & Anderson, R. G. Mis-assembly of clathrin lattices on endosomes reveals a regulatory switch for coated pit formation. *J Cell Biol* **123**, 1107-1117, doi:10.1083/jcb.123.5.1107 (1993).

240 Rodal, S. K. *et al.* Extraction of cholesterol with methyl-beta-cyclodextrin perturbs formation of clathrin-coated endocytic vesicles. *Mol Biol Cell* **10**, 961-974, doi:10.1091/mbc.10.4.961 (1999).

241 Kularatne, R. N., Crist, R. M. & Stern, S. T. The Future of Tissue-Targeted Lipid Nanoparticle-Mediated Nucleic Acid Delivery. *Pharmaceuticals (Basel)* **15**, doi:10.3390/ph15070897 (2022).

242 Liu, K. *et al.* Multiomics analysis of naturally efficacious lipid nanoparticle coronas reveals high-density lipoprotein is necessary for their function. *Nat Commun* **14**, 4007, doi:10.1038/s41467-023-39768-9 (2023).

243 Degors, I. M. S., Wang, C., Rehman, Z. U. & Zuhorn, I. S. Carriers Break Barriers in Drug Delivery: Endocytosis and Endosomal Escape of Gene Delivery Vectors. *Acc Chem Res* **52**, 1750-1760, doi:10.1021/acs.accounts.9b00177 (2019).

244 Qiu, C. *et al.* Advanced Strategies for Overcoming Endosomal/Lysosomal Barrier in Nanodrug Delivery. *Research (Wash D C)* **6**, 0148, doi:10.34133/research.0148 (2023).

245 Galliani, M., Tremolanti, C. & Signore, G. Nanocarriers for Protein Delivery to the Cytosol: Assessing the Endosomal Escape of Poly(Lactide-co-Glycolide)-Poly(Ethylene Imine) Nanoparticles. *Nanomaterials (Basel)* **9**, doi:10.3390/nano9040652 (2019).

246 Rozners, E. Chemical Modifications of CRISPR RNAs to Improve Gene-Editing Activity and Specificity. *J Am Chem Soc* **144**, 12584-12594, doi:10.1021/jacs.2c02633 (2022).

247 Leiter, A., Veluswamy, R. R. & Wisnivesky, J. P. The global burden of lung cancer: current status and future trends. *Nat Rev Clin Oncol* **20**, 624-639, doi:10.1038/s41571-023-00798-3 (2023).

248 de Sousa, V. M. L. & Carvalho, L. Heterogeneity in Lung Cancer. *Pathobiology* **85**, 96-107, doi:10.1159/000487440 (2018).

249 Barr, T., Ma, S., Li, Z. & Yu, J. Recent advances and remaining challenges in lung cancer therapy. *Chin Med J (Engl)* **137**, 533-546, doi:10.1097/CM9.0000000000002991 (2024).

250 Li, W. *et al.* mRNA-Lipid Nanoparticle-Mediated Restoration of PTPN14 Exhibits Antitumor Effects by Overcoming Anoikis Resistance in Triple-Negative Breast Cancer.

Adv Sci (Weinh) **11**, e2309988, doi:10.1002/advs.202309988 (2024).

251 Helmschrodt, C. *et al.* Polyethylenimine Nanoparticle-Mediated siRNA Delivery to Reduce alpha-Synuclein Expression in a Model of Parkinson's Disease. *Mol Ther Nucleic Acids* **9**, 57-68, doi:10.1016/j.omtn.2017.08.013 (2017).

252 Ryan, A. *et al.* Pharmaceutical design of a delivery system for the bacteriocin lacticin 3147. *Drug Deliv Transl Res* **11**, 1735-1751, doi:10.1007/s13346-021-00984-9 (2021).

253 Woodman, C., Vundu, G., George, A. & Wilson, C. M. Applications and strategies in nanodiagnosis and nanotherapy in lung cancer. *Semin Cancer Biol* **69**, 349-364, doi:10.1016/j.semcancer.2020.02.009 (2021).

254 Liu, Y. *et al.* Nanoparticles advanced from preclinical studies to clinical trials for lung cancer therapy. *Cancer Nanotechnol* **14**, 28, doi:10.1186/s12645-023-00174-x (2023).

255 Jurgens, D. C., Muller, J. T., Nguyen, A. & Merkel, O. M. Tailoring lipid nanoparticles for T-cell targeting in allergic asthma: Insights into efficacy and specificity. *Eur J Pharm Biopharm* **198**, 114242, doi:10.1016/j.ejpb.2024.114242 (2024).

256 Jang, S. C. *et al.* Bioinspired exosome-mimetic nanovesicles for targeted delivery of chemotherapeutics to malignant tumors. *ACS Nano* **7**, 7698-7710, doi:10.1021/nn402232g (2013).

257 Valcourt, D. M. *et al.* Advances in targeted nanotherapeutics: From bioconjugation to biomimicry. *Nano Res* **11**, 4999-5016, doi:10.1007/s12274-018-2083-z (2018).

258 He, Y. *et al.* Liposomes and liposome-like nanoparticles: From anti-fungal infection to the COVID-19 pandemic treatment. *Asian J Pharm Sci* **17**, 817-837, doi:10.1016/j.ajps.2022.11.002 (2022).

259 Wu, J. The Enhanced Permeability and Retention (EPR) Effect: The Significance of the Concept and Methods to Enhance Its Application. *J Pers Med* **11**, doi:10.3390/jpm11080771 (2021).

260 Wang, Z. *et al.* Active targeting theranostic iron oxide nanoparticles for MRI and magnetic resonance-guided focused ultrasound ablation of lung cancer. *Biomaterials* **127**, 25-35, doi:10.1016/j.biomaterials.2017.02.037 (2017).

261 Gabold, B. *et al.* Transferrin-modified chitosan nanoparticles for targeted nose-to-brain delivery of proteins. *Drug Deliv Transl Res* **13**, 822-838, doi:10.1007/s13346-022-01245-z (2023).

262 Mishra, R., Patel, H., Alanazi, S., Yuan, L. & Garrett, J. T. HER3 signaling and targeted therapy in cancer. *Oncol Rev* **12**, 355, doi:10.4081/oncol.2018.355 (2018).

263 Cho, H. S. & Leahy, D. J. Structure of the extracellular region of HER3 reveals an interdomain tether. *Science* **297**, 1330-1333, doi:10.1126/science.1074611 (2002).

264 Sithanandam, G. & Anderson, L. M. The ERBB3 receptor in cancer and cancer gene therapy. *Cancer Gene Ther* **15**, 413-448, doi:10.1038/cgt.2008.15 (2008).

265 Tanner, B. *et al.* ErbB-3 predicts survival in ovarian cancer. *J Clin Oncol* **24**, 4317-4323, doi:10.1200/JCO.2005.04.8397 (2006).

266 Lipton, A. *et al.* HER3, p95HER2, and HER2 protein expression levels define multiple subtypes of HER2-positive metastatic breast cancer. *Breast Cancer Res Treat* **141**, 43-53, doi:10.1007/s10549-013-2665-0 (2013).

267 Kumagai, T. *et al.* HER3 expression is enhanced during progression of lung adenocarcinoma without EGFR mutation from stage 0 to IA1. *Thorac Cancer* **9**, 466-471,

doi:10.1111/1759-7714.12609 (2018).

268 Beji, A., Horst, D., Engel, J., Kirchner, T. & Ullrich, A. Toward the prognostic significance and therapeutic potential of HER3 receptor tyrosine kinase in human colon cancer. *Clin Cancer Res* **18**, 956-968, doi:10.1158/1078-0432.CCR-11-1186 (2012).

269 Qian, G. *et al.* Heregulin and HER3 are prognostic biomarkers in oropharyngeal squamous cell carcinoma. *Cancer* **121**, 3600-3611, doi:10.1002/cncr.29549 (2015).

270 Schardt, J. S. *et al.* Engineered Multivalency Enhances Affibody-Based HER3 Inhibition and Downregulation in Cancer Cells. *Mol Pharm* **14**, 1047-1056, doi:10.1021/acs.molpharmaceut.6b00919 (2017).

271 Goldman, M. J. *et al.* Visualizing and interpreting cancer genomics data via the Xena platform. *Nat Biotechnol* **38**, 675-678, doi:10.1038/s41587-020-0546-8 (2020).

272 Kandil, R., Xie, Y., Mehta, A. & Merkel, O. A Method for Targeted Nonviral siRNA Delivery in Cancer and Inflammatory Diseases. *Methods Mol Biol* **2059**, 155-166, doi:10.1007/978-1-4939-9798-5_7 (2020).

273 Witta, S. E. *et al.* ErbB-3 expression is associated with E-cadherin and their coexpression restores response to gefitinib in non-small-cell lung cancer (NSCLC). *Ann Oncol* **20**, 689-695, doi:10.1093/annonc/mdn703 (2009).

274 Wadajkar, A. S. *et al.* Tumor-targeted nanotherapeutics: overcoming treatment barriers for glioblastoma. *Wiley Interdiscip Rev Nanomed Nanobiotechnol* **9**, doi:10.1002/wnan.1439 (2017).

275 Coldren, C. D. *et al.* Baseline gene expression predicts sensitivity to gefitinib in non-small cell lung cancer cell lines. *Mol Cancer Res* **4**, 521-528, doi:10.1158/1541-7786.MCR-06-0095 (2006).

276 Kronqvist, N. *et al.* Combining phage and staphylococcal surface display for generation of ErbB3-specific Affibody molecules. *Protein Eng Des Sel* **24**, 385-396, doi:10.1093/protein/gzq118 (2011).

277 Jay, S. M. *et al.* Engineered bivalent ligands to bias ErbB receptor-mediated signaling and phenotypes. *J Biol Chem* **286**, 27729-27740, doi:10.1074/jbc.M111.221093 (2011).

278 Abramson, J. *et al.* Accurate structure prediction of biomolecular interactions with AlphaFold 3. *Nature* **630**, 493-500, doi:10.1038/s41586-024-07487-w (2024).

279 Kandil, R. *et al.* Coming in and Finding Out: Blending Receptor-Targeted Delivery and Efficient Endosomal Escape in a Novel Bio-Responsive siRNA Delivery System for Gene Knockdown in Pulmonary T Cells. *Adv Ther (Weinh)* **2**, doi:10.1002/adtp.201900047 (2019).

280 Hao, F. *et al.* Polyethylenimine-based Formulations for Delivery of Oligonucleotides. *Curr Med Chem* **26**, 2264-2284, doi:10.2174/0929867325666181031094759 (2019).

281 Yong, K. W., Yuen, D., Chen, M. Z. & Johnston, A. P. R. Engineering the Orientation, Density, and Flexibility of Single-Domain Antibodies on Nanoparticles To Improve Cell Targeting. *ACS Appl Mater Interfaces* **12**, 5593-5600, doi:10.1021/acsami.9b20993 (2020).

282 Lee, J. H., Chapman, D. V. & Saltzman, W. M. Nanoparticle Targeting with Antibodies in the Central Nervous System. *BME Front* **4**, 0012, doi:10.34133/bmef.0012 (2023).

283 Kou, X., Zhang, W. & Zhang, W. Quantifying the Interactions between PEI and Double-Stranded DNA: Toward the Understanding of the Role of PEI in Gene Delivery. *ACS Appl Mater Interfaces* **8**, 21055-21062, doi:10.1021/acsami.6b06399 (2016).

284 Lee, S. Y. *et al.* Stability and cellular uptake of polymerized siRNA (poly-siRNA)/polyethylenimine (PEI) complexes for efficient gene silencing. *J Control Release* **141**, 339-346, doi:10.1016/j.jconrel.2009.10.007 (2010).

285 Guerrini, L., Alvarez-Puebla, R. A. & Pazos-Perez, N. Surface Modifications of Nanoparticles for Stability in Biological Fluids. *Materials (Basel)* **11**, doi:10.3390/ma11071154 (2018).

286 Polo, E. *et al.* Tips for the functionalization of nanoparticles with antibodies. *Methods Mol Biol* **1051**, 149-163, doi:10.1007/978-1-62703-550-7_11 (2013).

287 Lallana, E., Sousa-Herves, A., Fernandez-Trillo, F., Riguera, R. & Fernandez-Megia, E. Click chemistry for drug delivery nanosystems. *Pharm Res* **29**, 1-34, doi:10.1007/s11095-011-0568-5 (2012).

288 Jones, S. K., Sarkar, A., Feldmann, D. P., Hoffmann, P. & Merkel, O. M. Revisiting the value of competition assays in folate receptor-mediated drug delivery. *Biomaterials* **138**, 35-45, doi:10.1016/j.biomaterials.2017.05.034 (2017).

289 Papademetriou, J. *et al.* Comparative binding, endocytosis, and biodistribution of antibodies and antibody-coated carriers for targeted delivery of lysosomal enzymes to ICAM-1 versus transferrin receptor. *J Inherit Metab Dis* **36**, 467-477, doi:10.1007/s10545-012-9534-6 (2013).

290 Hirst, J. & Robinson, M. S. Clathrin and adaptors. *Biochim Biophys Acta* **1404**, 173-193, doi:10.1016/s0167-4889(98)00056-1 (1998).

291 Langer, A. *et al.* A New Spectral Shift-Based Method to Characterize Molecular Interactions. *Assay Drug Dev Technol* **20**, 83-94, doi:10.1089/adt.2021.133 (2022).

292 Luks, V. L. *et al.* Surface conjugation of antibodies improves nanoparticle uptake in bronchial epithelial cells. *PLoS One* **17**, e0266218, doi:10.1371/journal.pone.0266218 (2022).

10. List of Publications and Conference Contributions

Publications:

- Siyu Chen, Mariem Triki, Simone P. Carneiro, Olivia M. Merkel*. A Novel Micelleplex for Tumour-Targeted Delivery of CRISPR-Cas9 against KRAS-Mutated Lung Cancer. Nanoscale. (Under review)

- Siyu Chen, Simone P. Carneiro, Olivia M. Merkel*. Anionic polymer coating for enhanced delivery of Cas9 mRNA and sgRNA nanoplexes. Biomaterials science. (Under review)

- Siyu Chen, Sahana Sheshachala, Aditi Mehta, Simone P. Carneiro, Olivia M. Merkel*. Engineered-affibody conjugates contribute to the specific receptor-mediated cellular internalization of polyplexes in Erbb3 overexpressed lung cancer cells. (Manuscript in preparation)

- Siyu Chen, Simone P. Carneiro, Olivia M. Merkel*. The method to assess the cellular duration and degradation of mRNA and sgRNA after transfection with confocal co-localization. (Book chapter, Manuscript in preparation)

Conference Contributions:

- Gold Research Council (GRC) Drug Carriers in Medicine and Biology (Portland, USA, 2024)
  Poster presentation " The delivery of CRISPR to target *KRAS* mutations in lung cancer cells"

- Drug Delivery to The Lungs (Edinburgh, UK, 2023)
  Poster presentation " The delivery of CRISPR-Cas9 targeting *KRAS* mutant in lung cancer"

- Controlled Release Society (CRS) EU chapter meeting (Achen, Germany, 2022)
  Poster presentation "The delivery of CRISPR to target *KRAS* mutations for lung cancer therapy "

11. Acknowledgments

In November 2020, amidst the challenges of the COVID-19 pandemic, I embarked on my four-year doctoral journey, flying from Shanghai, China, to Munich, Germany, with both anticipation and trepidation. Life and study during this time presented numerous challenges, from adjusting to a new environment and culture to facing the inconveniences of a global shutdown. In the laboratory, I encountered many difficulties, learning from mistakes as I transitioned into a new scientific research field and initiated a project from scratch. However, these four years of experience have helped me grow significantly, both personally and professionally, allowing me to approach the unknown and face challenges with greater resilience.

For this, I am sincerely grateful to my supervisor, Prof. Dr. Olivia Merkel. Thank you for granting me the opportunity to pursue my Ph.D. in your group and work on such interesting projects. You have been more than just a mentor in research; you have been a guide in my personal growth. Your kindness and encouragement helped me navigate the initial confusion when I first joined the lab. Your vast knowledge and passion for science lit the path for me to follow in my research journey. I deeply appreciate all the opportunities and support you have provided over these four years.

I would also like to extend special thanks to my examiners. Thank you, Prof. Wolfgang Frieß, for evaluating my work as the second reviewer. My gratitude also goes to Prof. Stefan Zahler, Prof. Franz Bracher, Prof. Susanne Koch, and Prof. Ernst Wagner for taking the time to serve on my defense committee and assessing my work.

Next, I would like to express my appreciation to Dr. Aditi Mehta, our former Postdoc, for providing me with this fascinating research topic. Although we only met a few times, your foundational work and experience greatly contributed to the success of this project.

My sincere gratitude goes to Dr. Simone Carneiro, our Postdoc. Thank you for

your unwavering support throughout my work. Collaborating with you was an unforgettable experience, and your insights and guidance were invaluable when the project encountered obstacles.

I am also grateful to the senior Ph.D. students, Dr. Yao Jin, Dr. Lorenz Isert, Dr. Domizia Baldassi, Dr. Bettina Gabold, Dr. Natascha Hartl, and Dr. Christoph Zimmermann. Thank you for your patience and guidance when I first joined the lab. Your mentorship helped me develop essential experimental skills and become a more professional researcher. I truly enjoyed our time together, especially during the difficult days of the pandemic.

To Gabriele Loiudice, thank you for being such a wonderful lab mate, and always bringing laughter and positivity to the lab! I would also like to thank my colleagues over the years: Dr. Benjamin Winkeljann, Dr. Valentin Fell, Dr. Müge Molbay, Dr. Karin Bartel, Dr. David Jürgens, Joschka Müller, Leonie Deßloch, Adrian Kromer, Min Jiang, Katharina Steinegger, Anny Nguyen, Katrin Wiebe, Stina Rademacker, Felix Sieber-Schäfer, Lasse Hagedorn, Carolina Fuchs, Fabian Link, Nora Martini, Moritz Marschhofer, Jiayi Zhu, and Leon Reger. Thank you for fostering a great working environment! Additionally, thanks to Fabian Volk, Cynthia Zettl, Judith Möller, and Kate Kutsenok. Though our time together was brief, your kindness and friendliness left a lasting impression. Many thanks to my master student, Mariem Triki, and student assistant, Deepak K. Sundaramoorthy, for your dedication and hard work on the project.

I would also like to extend my sincere thanks to Prof. Gerhard Winter, the former chair, for your outstanding leadership. I am grateful to Gabriele Brandstäter, Sabine Kohler, Dr. Gerhard Simon, Dr. Alexandra Mößlang, Dr. Katharina Prüßmann, Susanne Petzel, Alice Hirschmann, and Regine Bahr for your support in keeping the lab running smoothly. A big thank you to all the members of AK Winter and AK Frieß for the wonderful atmosphere and unforgettable memories we shared.

I also want to acknowledge the China Scholarship Council for providing financial support during my Ph.D. studies and personal life.

Heartfelt thanks to my friends in Munich, you have been like a second family to me during these four years. Thank you for all the laughter, meals, and trips we shared. I have cherished every moment.

Last but not least, I would like to thank my parents and family. Your constant support has been the foundation of my journey, and I would not be who I am today without you.